UPC **CTTC**

Numerical methods for radiative heat transfer

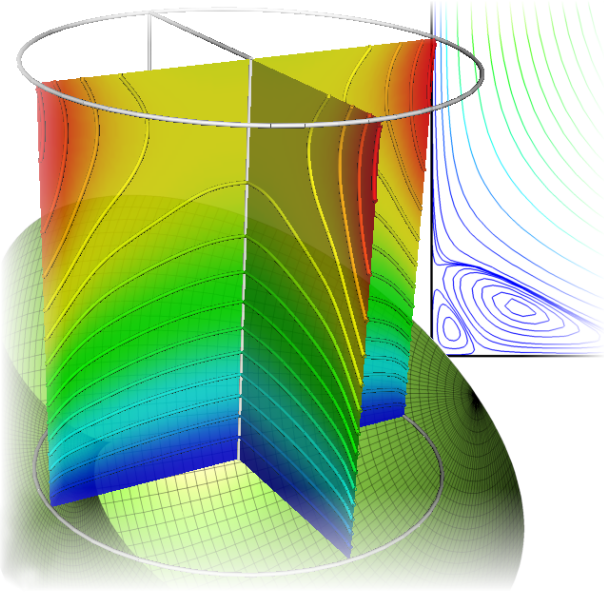

Centre Tecnològic de Transferència de Calor
Departament de Màquines i Motors Tèrmics
Universitat Politècnica de Catalunya

Guillem Colomer Rey
Doctoral Thesis

Guillem Colomer Rey

DOCTORAL THESIS

UPC – Juny 2006

Numerical methods for radiative heat transfer

Guillem Colomer Rey

TESI DOCTORAL

presentada al

Departament de Màquines i Motors Tèrmics
E.T.S.E.I.T.
Universitat Politècnica de Catalunya

per a l'obtenció del grau de

Doctor en Ciències Físiques

Terrassa, Juny 2006

Numerical methods for radiative heat transfer

Guillem Colomer Rey

Directors de la Tesi

Dr. Miquel Costa Pérez
Dr. Assensi Oliva Llena
Dr. Ricard Cònsul Serracanta

Tribunal Qualificador

Dr. José Pinazo Ojer
Universitat Politècnica de València
Dr. Carlos David Pérez Segarra
Universitat Politècnica de Catalunya
Dr. Antonio Pascau Benito
Universidad de Zaragoza
Dr. Eduard Egusquiza Estevez
Universitat Politècnica de Catalunya
Dr. Agustín Macías Machín
Universidad de Las Palmas de Gran Canaria

Agraïments

Vull aprofitar aquestes ratlles per donar les gràcies a tothom qui ha contribuït, d'una o altra manera, a que aquest treball s'hagi pogut completar. D'entrada, a l'Assensi Oliva, que em va animar a començar aquest projecte, a més de proporcionar totes les eines, bàsicament informàtiques, que he emprat tots aquests anys. De manera molt especial, agrair-li la seva comprensió en moments difícils, permetent-me agafar-me el treball al meu ritme.

Molt important ha estat també la calidesa que han aportat tots els membres del grup, els que hi son i els qui han marxat, i que han fet d'aquest un lloc on hi he treballat realment de gust. I, no podia faltar, el meu agraïment també al sector informàtic que manté els equipaments en funcionament, aixi com el "cluster", del que n'he tret profit puntualment.

M'agradaria tenir un record per en Miquel Costa, que desafortunadament va emmalaltir al poc de començar la meva feina. Vam tenir el temps just de col·laborar en un parell de treballs, però malauradament, no ha pogut veure aquesta tesi finalitzada.

Aquesta tesi tampoc hauria estat possible sense el suport i el recolzament dels meus pares, i que amb l'Eva i l'Aina han tingut la paciència d'aguantar-me durant tot aquest temps. I a la Noe, que, en l'elaboració de la tesi, m'ha hagut de suportar més que ningú. A vosaltres,doncs , que m'heu donat tantes i tantes mostres d'estimació i afecte, us la dedico.

Contents

C Characterization of flows 153

Outline

The main objective of the present thesis is to study the energy transfer by means of radiation. Therefore, the basic phenomenology of radiative heat transfer has been studied. However, considering the nature of the equation that describes such energy transfer, this work is focussed on the numerical methods which will allow us to take radiation into account, for both transparent and participating media. Being this the first effort within the CTTC ("Centre Tecnològic de Transferència de Calor") research group on this subject, it is limited to simple cartesian and cylindrical geometries.

For this purpose, chapter 1 contains an introduction to radiative energy transfer, and the basic equations that govern radiative transfer are discussed. These are the radiative transfer equation, formulated in terms of the absorption and scattering coefficients, and the energy equation. It is also given a discussion on when this mode of energy transfer should be considered. In this chapter are also defined all of the magnitudes and concepts used throughout this work. It ends with a brief description of some approximate methods to take radiation into account.

The Radiosity Irradiosity Method, RIM, which is suitable only for transparent media, is introduced in chapter 2. In this chapter it is also described a numerical method to calculate the view factors for axial symmetric geometries. The main results obtained in such geometries are also presented. Although a little disconnected from the rest of the present thesis, the algorithm used to handle "de facto" three dimensional geometries with computation time just a little longer than two dimensional cases, with no additional memory consumption, is considered worthy enough to be included in this work.

In chapter 3, it is detailed one of the most widely used numerical methods to effectively compute radiation energy transfer within either transparent or participating media. This method is called the Discrete Ordinates Method (DOM). The fundamental aspect of this method is the choice of an ordinate set to integrate the radiative transfer equation. The characterization of such valuable ordinate sets is laid out properly. The discretization of the radiative transfer equation, presented in chapter 1, is explained in detail, for both cartesian and cylindrical geometries. The direct solution procedure is also outlined. Finally, illustrative results obtained with the DOM under several conditions are presented.

In the moment we wish to solve real problems, we face the fact that the properties on which the radiative transfer equation is based, i. e., the absorption and scattering coefficients, depend strongly on radiation wavelength. Therefore, there are situations where the usually assumed gray behavior of the media involved is far from being true. In the present thesis, special emphasis has been placed on studying the radiative properties of real gases in chapter 4. This interest resulted on a bibliographical research on how the wavenumber dependence of the absorption coefficient, a fundamental issue regarding radiation heat transfer, is modeled and estimated. Furthermore, this bibliographical research was focussed also on numerical models capable of handle such wavenumber dependence. Remarks about the different methods considered can be found in section 4.3. Several methods are discussed, and two of them, namely the Weighted Sum of Gray Gases (WSGG) and the Spectral Line Weighted sum of gray gases (SLW), have been implemented to perform non gray calculations. Some significant results are shown.

Plenty of tests have been performed to the numerical code that resulted from the elaboration of this thesis. Its results have been compared to other numerical methods, published in several specialized journals, or directly to available analytical solutions. Cartesian and cylindrical geometries are the only ones taken into account. According to the results obtained, the objectives proposed in this thesis have been satisfied. As a demonstration of the usefulness of the implemented code, it has been succesfully integrated to a wider, general purpose, computational fluid dynamics code (DPC), fruit of the effort of many researchers during many years.

Results of the above integration lead to the resolution of combined heat transfer problems, that are analyzed in chapters 5 and 6, where radiative heat transfer is coupled to convection heat transfer. The effect of radiation on the total heat transfer is studied in chapter 5, which has been published as *International Journal of Heat and Mass Transfer*, volume 47 (issue 2), pages 257–269, year 2004. In chapter 6, the influence of some parameters of the SLW model on a combined heat transfer problem is analyzed. This chapter has been submitted for publication at the *Journal of Quantitative Spectroscopy and Radiative Transfer*.

Chapter 7 contains some final general remarks as well as ideas on how the present work could be continued.

Finally the appendices include some material which would disturb the normal reading flow of the thesis, such as appendices A and B, and also material that does not fit too well within the title of the thesis in appendix C. All this material follows from the six-year period on which this thesis has been developed.

1

Radiative heat transfer

1.1 State of the art

Radiation heat transfer has been, probably, the last mode of energy transfer to be widely taken into account by the community of numerical scientists. The reason is mainly the nature of the radiative transfer equation, which will be discussed later. This equation determines the intensity radiation field, a magnitude used to perform radiative energy balances over volumes and surfaces. In its general form, the radiative transfer equation involves both differentiation and integration, and therefore a complete solution is available only for a few limited situations.

The natural approach to account for radiation is, therefore, to simplify the radiative transfer equation. The most dramatic simplification is to consider transparent media, meaning that radiative exchange takes place only between surfaces. In these cases, the radiative transfer equation needs not to be solved and alternative techniques exist. This is the simplest way to take radiation into account, and it comes, in general, at a low computational cost. The most popular of such methods is the Radiosity-Irradiosity Method (RIM), which is detailed in chapter 2.

The years passed, and the computers got faster and better. Different numerical methods to solve the radiative transfer equation were formulated. These include the Discrete Transfer Method [1], the Discrete Ordinates Method [2] (DOM), described in chapter 3, and some of its variants [3,4,5], Finite Volume Methods [6], the REM^2 method [7]... These methods are all capable of handle radiation in transparent and participating, gray media. Other methods are also discussed in section 1.6. Further improvements on radiation modelling include the development of non gray methods, as a set of models which, accordingly, are independent of the radiative transfer equation solver. Different levels of accuracy can be achieved by such non gray models, whose discussion is left to chapter 4.

With respect to numerical techniques to integrate differential equations, the conventional radiative transfer equation solvers use the same solutions applied in computational fluid dynamics to improve its performance. Several works on parallelization exists [8], with the additional decision on whether it is better to parallelize the spatial or the angular domain. Good performances are obtained for spatial decomposition [9]. Monte Carlo radiation solvers do not face such decision, since they are very well suited to be parallelized [10]. Interpolation schemes are also considered, beyond the typical high-order schemes employed in the convection-diffusion equation. Given the directional nature of radiation, the intensity is not interpolated from neighboring nodes but from its projection along the propagation direction [11].

The situations where radiative heat transfer plays a fundamental role are those where high temperatures are achieved. Notably, when simulating combustion chambers, radiation should be taken into account, with a complete solution of the radiative transfer equation, as in [12]. However, a survey on combustion oriented literature reveals that this is not exactly the case, since few works on this subject consider radiative heat transfer. And if they do, usually over-simplified models are assumed, models that even do not require the full solution of the radiative transfer equation [13].

Radiative transfer is considered also in turbulent flows. Due to the additional overhead that turbulence implies, earlier works [14] simply inserted a source term due to radiation in the Favre averaged Navier-Stokes equations, and no average was performed at all when solving the radiative transfer equation. Latter works do take into account the interaction between turbulence and radiation, by solving a time averaged radiative transfer equation and modeling the correlated quantities [15, 16]. A detailed review on these correlations can be found in [17].

In fire safety science, where an estimate of the energy output of a fire is desired, radiation transfer is a key aspect to be taken into account [18, 19]. Radiation is also the dominant mode of energy transfer in rocket plumes. These are analyzed in order to improve combustion efficiency and the base protection from radiation heating. The presence of scattering particles in a plume is considered in [20]. Furthermore, the study of industrial furnaces also requires the solution of the radiative transfer equation [21], not to mention any application which involves the use of solar energy.

1.2 Mathematical description of radiation

We refer as radiative energy transfer to the variation of the energy of any system due to absorption or emission of electromagnetic waves. From a physical point of view, such electromagnetic waves can be understood as a group of massless particles that propagate at the speed of light c. Each of these particles carries an ammount of energy, inversely proportional to the wavelength of its associated wave. Such particles are dubbed photons. A single photon represents a plane wave, therefore we are forced to assume that it propagates along a straight path. Because of this, we can think of a system loosing energy by emitting a number of photons, or gaining energy by absorbing them.

Each photon has a well defined polarization state, an internal degree of freedom, which is important in calculating properties such as the fraction of incident energy that is reflected by a medium. However, thermal radiation is not polarized on average, and therefore the polarization of the photons is ignored hereinafter.

Radiation heat transfer presents a number of unique characteristics. First of all, the amount of radiative heat transfer does not depend on linear differences of temperature, but on the difference of the fourth power of the temperature. This fact implies that, at high temperatures, radiative energy transfer should be taken into account, particularly if large differences in temperature exist. Furthermore, it is the only one form of energy transfer in vacuum. Therefore, in vacuum applications, radiation should be taken into account, even an low temperatures. And, of course, it should be taken into account for study of devices which use solar energy.

On the other hand, radiation can be neglected if there are no significant temperature differences in a given system, and also if highly reflective walls are present. Furthermore, this kind of walls can prevent bodies to radiate energy away, as well as to shield sensible components from damaging radiation. Such shields can be seen in any spacecraft, for instance.

In order to fully account for radiation transfer, we are obliged to solve Maxwell equations for the electromagnetic field. Since these equations are linear, any solution can be represented as a superposition of plane waves, i. e., by a certain set of photons. It turns out that, by treating radiative transfer in this way, it won't be necessary to solve the Maxwell equations. Therefore, all we need is to concentrate on the number of photons present at a single point, and its energy distribution. As the photons propagate along straight paths, we also need to know, at every spatial location, the number of photons propagating in a given solid angle. Under the assumption of straight propagation, we are neglecting the wave properties of radiation. However, these are only relevant for cavities whose size is of the order of magnitude of the radiation wavelength. This is not the case for most of the practical problems, since we can estimate the the longest significant wavelength at room temperature to be less than 20 microns. For high temperature applications, such wavelength is reduced further. Only for cavities of these dimensions wave properties of radiation become relevant.

The photon density is defined as the number of photons, with wavelength between λ and $\lambda + d\lambda$, crossing an area dA perpendicular to the photon direction $\hat{\mathbf{s}}$, within a solid angle $d\Omega$, per unit time dt and per unit wavelength $d\lambda$. It is more useful to consider the energy density I instead of the photon density. The energy density is simply the number of photons multiplied by the energy of each photon. The energy density is usually named intensity radiation field, and its physical meaning is therefore

$$I(\mathbf{r}, \hat{\mathbf{s}}, \lambda) = \frac{\text{energy of wavelength } \lambda \text{ through an area normal to } \hat{\mathbf{s}}}{dA\, d\Omega\, d\lambda\, dt}. \tag{1.1}$$

From this definition is clear that, for a fixed point and wavelength, the intensity radiation field is a function defined over the unit sphere, and therefore is not a conventional scalar field, such as the temperature. With the definition of the intensity radiation field on mind, the total energy that crosses a surface perpendicular to a given unit vector $\hat{\mathbf{n}}$, per unit time and area, is readily obtained as

$$q(\mathbf{r}, \hat{\mathbf{n}}) = \int_0^\infty d\lambda \int_{4\pi} d\Omega\, (\hat{\mathbf{n}} \cdot \hat{\mathbf{s}}) I(\mathbf{r}, \hat{\mathbf{s}}, \lambda), \tag{1.2}$$

where the $(\hat{\mathbf{n}} \cdot \hat{\mathbf{s}})$ factor appears since I is defined as energy through the propagation direction $\hat{\mathbf{s}}$.

1.3 Radiative properties of materials

1.3.1 Black body radiation

Once the mathematical tools for the description of radiation energy are settled, it would be interesting to know how much energy emits a body under different physical conditions. This one turns out to be a complicated problem, so some simplifying hypothesis are required. The simplest possible case is that of the black body. Historically, the problem that posed the black body to late 19th century scientists lead to the formulation of the first quantum hypothesis, which finally resulted in a revolution in physics and, consequently, on the other sciences.

The black body plays the same role as the ideal gas, in the sense that its behavior is the same no matter of what is made. It also serves as a basis for more complicated bodies. By definition, any body which absorbs the totality of photons that incide on it, is called a black body. For such a body in thermal equilibrium with its surroundings, it has to emit as much radiation energy as it absorbs, otherwise it will heat up or cool down. This fact is called the Kirchhoff law. The energy emitted by a black body depends only on its temperature, and the distribution over all wavelengths is

$$I_b(T, \lambda) = \frac{2hc^2}{\lambda^5} \frac{1}{\exp(hc/\lambda kT) - 1}, \tag{1.3}$$

where h is the Planck's constant, k is the Boltzmann constant, and c is the speed of light. The photon emission by a black body is isotropical, that is, it does not depend on any particular direction $\hat{\mathbf{s}}$. Therefore, by using equation 1.2, carrying out the angular integration over an hemisphere, we find that the energy emitted by a black body per unit area, time and wavelength is simply $E_b(T, \lambda) = \pi\, I_b(T, \lambda)$.

An important feature of a black body is the emissive power per unit area, which is readily found by integrating equation 1.3 over all wavelengths. The result is the well known Stefan-Boltzmann law, which relates the emissive power to the temperature of the black body:

$$I_b(T) = \frac{2\pi^4 k^4}{15 h^3 c^2} T^4 = \frac{\sigma_B T^4}{\pi}. \tag{1.4}$$

Using equation 1.3, it is possible to show that the wavelength at which the black body emission intensity is maximum times the temperature is constant. This is known as Wien law. After some calculation, we find that $\lambda_{\max} T = 2897.82\ \mu m K$.

1.3.2 Surface properties

Each surface will radiate a certain ammount of energy due to its temperature. Such emitted energy, which will depend on the properties of the surface, its temperature, the radiation wavelength, the direction of emission. . . leads to the definition of the emissivity of a surface. As stated before, we can use the black body as a reference to define the surface properties of real bodies. Therefore, if the surface is at temperature T, the emissivity is defined as

$$\varepsilon = \frac{I_{\text{emitted}}(T, \lambda, \hat{\mathbf{s}})}{I_b(T, \lambda)}. \tag{1.5}$$

where the temperature, wavelength, and incident direction dependence, have been dropped for the sake of clarity. As the black body is defined as the perfect radiation absorber, by the Kirchhoff law, there is no body capable of emitting more radiation energy than a black body for any given temperature. Therefore, the emissivity ε will be between zero and one.

On the other hand, when an electromagnetic wave incides on a surface, the interaction between this incident wave and the elements of the surface result on a fraction of the energy of the wave being reflected, while the remaining fraction will be absorbed (or transmitted) within the material. These fractions may very well depend on the incident angle and the wavelength of the original wave. Specifically, we can define

$$\rho = \frac{I_{\text{reflected}}}{I_{\text{incoming}}}; \quad \alpha = \frac{I_{\text{absorbed}}}{I_{\text{incoming}}}; \quad \tau = \frac{I_{\text{transmitted}}}{I_{\text{incoming}}}; \tag{1.6}$$

again, the temperature, wavelength, and incident direction dependence, have been dropped. The coefficients ρ, α, and τ, are the reflectivity, absorptivity, and transmissivity of the surface respectively. As the wave is either reflected, or absorbed, or transmitted, it is clear that we must have $\rho + \alpha + \tau = 1$ if the energy is to be conserved.

An important feature of reflection should be pointed out: while the reflected wave has the same angle (with respect to the normal of the surface) of the incident wave for perfectly smoot surfaces, if the surface is not polished, the angle of the reflected wave could have any value, due to multiple reflections. There is a fraction of the incoming intensity that is equally distributed for all possible outgoing directions. Due to this, the reflectivity ρ is usually divided in a diffuse component ρ_d, and a specular component ρ_s. Therefore, a fraction ρ_d of the incoming energy will be reflected equally over all the angles, and a fraction ρ_s will be reflected in a angle equal to that of the incident wave. We have of course $\rho = \rho_d + \rho_s$.

Moreover, a surface that absorbs a fraction α of the incident energy will emit the same amount of energy if it is at thermal equilibrium (the Kirchhoff law again). Therefore, we could assume that $\alpha(T, \lambda, \hat{\mathbf{s}}) = \varepsilon(T, \lambda, \hat{\mathbf{s}})$. A good approximation is to assume also that the corresponding integrated, wavelength and direction independent, absorptivity and emissivity are equal. Hence, three parameters, namely ρ_d, ρ_s, and ε, will suffice to describe the radiative properties for any surface.

1.4 Radiative transfer equation

We are assuming that photons propagate along straight lines, hence the most natural way to examine the effect exerted by the medium on the number of photons (or equivalently on the intensity radiation field) is to analyze the intensity radiation field precisely along a straight line. In the most general case, the intensity along the direction defined by the unit vector $\hat{\mathbf{s}}$ will depend both on the distance ℓ in this direction, and on time t. Therefore we could write the variation of intensity with respect to ℓ and t as

$$dI = I(\ell + d\ell, t + dt) - I(\ell, t) = \frac{\partial I}{\partial \ell} d\ell + \frac{\partial I}{\partial t} dt. \tag{1.7}$$

Recalling that photons travel at the speed of light c, we have $d\ell = c\,dt$, and the resulting variation of intensity per unit length along the direction $\hat{\mathbf{s}}$ is

$$\frac{dI}{d\ell} = \frac{\partial I}{\partial \ell} + \frac{1}{c}\frac{\partial I}{\partial t}. \tag{1.8}$$

The speed of light is very high, resulting on the fact that, for practical purposes, we can think that the intensity radiation field instantly reacts to any changes of the physical conditions that determine it. Therefore, the partial derivative of I with respect to time t in equation 1.8, will be ignored hereinafter.

As an electromagnetic wave propagates inside a medium, it looses energy as the charged particles within de medium accelerate in response to the wave. These particles, in turn, release part of its energy in form of electromagnetic waves. In the photon framework, we think of the same process as photons being absorbed and emitted by the medium. However, if the final state of the interacting particle is the same as the initial state, we understand that the corresponding photon is simply redirected (and therefore has the same energy). We say that such a photon is scattered. It turns out that scattered photons complicate the formulation of the radiative transfer equation (RTE), by turning a simple linear differential equation to an integro-differential one, combining differentiation with respect one set of variables (spatial location) and integration over another set of variables (solid angle).

The RTE accounts for the variation of the intensity radiation field, readily related to the number of photons, on a direction given by the unit vector $\hat{\mathbf{s}}$. Such variation can be attributed to different phenomena, and is usually divided in three additive terms. It is written as

$$\frac{dI(\hat{\mathbf{s}})}{d\ell} = -(\kappa + \sigma_s)I(\hat{\mathbf{s}}) + \kappa I_b + \frac{\sigma_s}{4\pi}\int_{4\pi} \phi(\hat{\mathbf{s}}';\hat{\mathbf{s}})I(\hat{\mathbf{s}}')\,d\Omega', \tag{1.9}$$

where, for simplicity, the spatial dependence on the path ℓ of the intensity I, as well as its wavelength dependence, are not explicitly written. This equation, however, does not hold if the wave characteristics of radiation are manifest. In the above equation, which is valid for a single wavelength, one should use equation 1.3 when calculating the second right hand side term. If the absorption and scattering coefficients κ and σ_s are zero, the RTE is simplified enormously. Under such conditions, we talk of a transparent medium, and for very small domains, compared to $1/\kappa$ or $1/\sigma_s$, this approximation is reliable.

The first term, which is negative, accounts for the decrease of the number of photons on the given direction, either because it is absorbed by the medium (with an absorption coefficient κ) or because it is scattered onto another direction (with a scattering coefficient σ_s). The second term has positive sign, therefore implying an increase of the number of photons. This term is due to thermal emission of photons. It is zero only if the temperature is zero, or the absorption coefficient is zero. Notice that the proportionality coefficient is the same absorption coefficient appearing in the first term. This holds under the assumption of local thermodynamic equilibrium (see, for instance, Modest [22], section 9.2). The third term contributes only if the medium scatters radiation. We should take into account that any photon, propagating along a direction given by $\hat{\mathbf{s}}'$, may be redirected to the analyzed direction $\hat{\mathbf{s}}$. We define the function $\phi(\hat{\mathbf{s}}';\hat{\mathbf{s}})$ to be 4π times the probability of such redirection occurring. Then we integrate to consider all possible directions $\hat{\mathbf{s}}'$. The function $\phi(\hat{\mathbf{s}}';\hat{\mathbf{s}})$ is known as the phase function. It has to be normalized, in a way that

$$\int_{4\pi} \phi(\hat{\mathbf{s}}';\hat{\mathbf{s}})\,d\Omega = 4\pi, \tag{1.10}$$

where this time the phase function is integrated over the second argument. This equation merely states that the incoming photon should be scattered into some other direction.

However, the interaction between radiation and matter is more complicated than that, and it is indeed possible for a scattered photon to vary its energy. This can be taken into account by allowing the phase function to depend on the incoming and outgoing photon wavelengths. The usual approximation for problems related to heat transfer is to consider elastic scattering, that is, to take a phase function of the form used in equation 1.9, thus ignoring the energy change of a scattered photon. Moreover, it is assumed that the phase function depends only on the relative orientation of the two directions $\hat{\mathbf{s}}$ and $\hat{\mathbf{s}}'$, that is, of the scalar product $\hat{\mathbf{s}} \cdot \hat{\mathbf{s}}' = \cos\theta$. This allows any phase function to be written as the series expansion

$$\phi(\cos\theta) = \sum_{n=0}^{\infty} A_n P_n(\cos\theta), \tag{1.11}$$

where the P_n are the Legendre polynomials. Most commonly used phase functions are these with $n = 0$ (isotropic phase function), which implies $\phi(\cos\theta) = 1$ and with $n = 1$ (linear anisotropic phase function), which results in $\phi(\cos\theta) = 1 + A_1 \cos\theta$.

The radiative transfer equation is sometimes written by changing the geometrical length variable ℓ by the optical depth (or thickness) τ, defined by $d\tau = \beta\, d\ell$ where $\beta = \kappa + \sigma_s$ is the extinction coefficient. The optical thickness is defined in a differential fashion, since the extinction coefficient may depend on ℓ, for instance for a non isothermal medium. The use of the non dimensional optical depth is useful, since approximations to the RTE exists for the limits of large or small optical thickness. On the other hand, a large absorption coefficient is meaningless until the size of the domain under consideration is given. In this variable, then, the RTE becomes

$$\frac{dI(\hat{\mathbf{s}})}{d\tau} = -I(\hat{\mathbf{s}}) + (1-\omega)I_b(\tau) + \frac{\omega}{4\pi}\int_{4\pi} \phi(\hat{\mathbf{s}}';\hat{\mathbf{s}})I(\hat{\mathbf{s}}')\, d\Omega', \tag{1.12}$$

where $\omega = \sigma_s/\beta$ is known as the albedo, a measure of the relative significance of absorption and scattering. Notice that the optical thickness is dimensionless, and therefore the above equation can be thought as being non-dimensional.

The radiative transfer is subject to a variety of boundary conditions. The most widely used is that of a opaque surface, described by its reflectivity ρ_d, ρ_s, and emissivity ε. If the unit vector $\hat{\mathbf{n}}$ denote the normal to the surface, the monochromatic wall boundary condition verified by the intensity is

$$I_0(\hat{\mathbf{s}}) = \varepsilon I_b(T_0, \lambda) + \rho_s(\hat{\mathbf{s}}^*)I(\hat{\mathbf{s}}^*) + \frac{1}{\pi}\int_{\hat{\mathbf{n}}\cdot\hat{\mathbf{s}}<0} \rho_d(\hat{\mathbf{s}})|\hat{\mathbf{n}}\cdot\hat{\mathbf{s}}|I_0(\hat{\mathbf{s}})\, d\Omega, \tag{1.13}$$

where $\hat{\mathbf{s}}^*$ is the reflected outgoing direction $\hat{\mathbf{s}}$ through the plane defined by the boundary. Here we have labeled with a subindex 0 the values at the boundary. The first term represents the thermal contribution of the surface. This term may depend on the outgoing direction through the emissivity coefficient, and is directly taken from equation 1.5. The second term is simply the specular contribution to the direction $\hat{\mathbf{s}}$ given by the specular reflectivity. The third term takes into account the diffuse contribution of the reflected intensity, and hence all incoming directions should be considered. This is why the integral is carried out over the incoming directions to the surface. This boundary equation works only for directions such that $\hat{\mathbf{n}} \cdot \hat{\mathbf{s}} > 0$.

Of course, the above boundary condition is not the only suitable for radiation heat transfer. For instance, for solar colector applications, more information should be provided, such as the amount of direct intensity, incidence angle, and so on. These boundary conditions have been used in [23]. See section 3.3.3 for a deeper explanation of these particular boundary conditions.

Given the integro-differential nature of the radiative transfer equation, it is not surprising that few analytical solutions exist. However, a formal solution can be obtained, even for a scattering medium, although the solution for I depends, in general, on the angular integral of I. This formal solution is obtained in section A.1. Analytical solutions are important since they will assist on the verification of the RTE solvers.

1.5 Energy equation

Under certain conditions, energy transfer by radiation may be the dominant mode of heat transfer. In such cases, the denomination radiative equilibrium is used. In a steady state condition, the radiative heat flux per unit volume, i. e., the divergence of the radiative heat, must equal the source term S everywhere in the domain. Then, the energy conservation equation has only one term, and takes the simple form

$$\boldsymbol{\nabla} \cdot \mathbf{q}_r = \mathcal{S}. \tag{1.14}$$

Energy transfer by conduction, convection, as well as other terms that could contribute are ignored. As stated before, once the intensity radiation field is known, the divergence of radiative heat flux is readily obtained by the balance between absorbed and emitted energy. Using equation 1.2 we could find the energy gain or loss on an infinitessimal volume $dV = dx\,dy\,dz$. For that matter, we choose cartesian coordinates and consider the difference in the heat flux per unit area through two x planes separated by a distance dx, which gives the amount of radiative energy accumulated in this infinitesimal length dx. This is $q(\mathbf{r} + \hat{\mathbf{\imath}} dx, \hat{\mathbf{\imath}}) - q(\mathbf{r}, \hat{\mathbf{\imath}}) \simeq \partial q(\mathbf{r}, \hat{\mathbf{\imath}})/\partial x\, dx$. Analogous expressions are obtained for the corresponding y and z planes, replacing also $\hat{\mathbf{\imath}}$ for $\hat{\mathbf{\jmath}}$ or $\hat{\mathbf{k}}$. The total heat flux of this cubic volume is therefore

$$\left(\frac{\partial q(\mathbf{r}, \hat{\mathbf{\imath}})}{\partial x} + \frac{\partial q(\mathbf{r}, \hat{\mathbf{\jmath}})}{\partial y} + \frac{\partial q(\mathbf{r}, \hat{\mathbf{k}})}{\partial z} \right) dV = \boldsymbol{\nabla} \cdot \mathbf{q}_r\, dV \tag{1.15}$$

if we let $\mathbf{q}_r(\mathbf{r}) = q(\mathbf{r}, \hat{\mathbf{\imath}})\hat{\mathbf{\imath}} + q(\mathbf{r}, \hat{\mathbf{\jmath}})\hat{\mathbf{\jmath}} + q(\mathbf{r}, \hat{\mathbf{k}})\hat{\mathbf{k}}$. Next, we substitute equation 1.2 in equation 1.15, and since the integration is over the solid angle and the derivation is with respect to the spatial coordinates, we may put the differential operator inside the integral. Furthermore, neither $\hat{\mathbf{n}}$ nor the dummy variable $\hat{\mathbf{s}}$ depend on the location. Hence, we have (on a monochromatic basis)

$$\nabla \cdot \mathbf{q}_r = \int_{4\pi} \left\{ (\hat{\mathbf{\imath}} \cdot \hat{\mathbf{s}}) \frac{\partial I}{\partial x} + (\hat{\mathbf{\jmath}} \cdot \hat{\mathbf{s}}) \frac{\partial I}{\partial y} + (\hat{\mathbf{k}} \cdot \hat{\mathbf{s}}) \frac{\partial I}{\partial z} \right\} d\Omega. \tag{1.16}$$

The integrand is precisely the left hand side of the radiative transfer equation (written in cartesian coordinates), so we can substitute it by the right hand side of equation 1.9. This results in

$$\nabla \cdot \mathbf{q}_r = \int_{4\pi} \left\{ -(\kappa + \sigma_s) I(\hat{\mathbf{s}}) + \kappa I_b + \frac{\sigma_s}{4\pi} \int_{4\pi} \phi(\hat{\mathbf{s}}'; \hat{\mathbf{s}}) I(\hat{\mathbf{s}}')\, d\Omega' \right\} d\Omega. \tag{1.17}$$

The first two terms are readily obtained as $-(\kappa + \sigma_s)G + 4\pi\kappa I_b(\ell)$, defining $G = \int_{4\pi} I\, d\Omega$. This integral G is the incident energy and depends on the position $\mathbf{r}$ only. The third term is easily obtained by inverting the integration order. By doing so we get

$$\frac{\sigma_s}{4\pi} \int_{4\pi} \left\{ I(\hat{\mathbf{s}}') \int_{4\pi} \phi(\hat{\mathbf{s}}'; \hat{\mathbf{s}})\, d\Omega \right\} d\Omega'. \tag{1.18}$$

Using equation 1.10, we see that the inner integral is just 4π. The resulting term is then $\sigma_s G$. When adding up with the other terms, we see that the scattering involving terms cancel out, consistent with the previous assumption that scattering only redirects photons without changing its energy.

The preceding discussion is valid for a single wavelength, to avoid excessive notational complications. To account for the total heat transfer due to radiation, we must integrate the above expression over all wavelengths:

$$\nabla \cdot \mathbf{q}_r = \int_0^\infty \kappa \left(4\pi I_b - G \right) d\lambda, \tag{1.19}$$

where everithing inside the integral is presumabily wavelength dependant. After integration of the above equation over the whole spectrum, and equating the source term to the divergence of heat flux, we have

$$\mathcal{S} = 4\kappa_P \sigma_B T^4 - \int_0^\infty \kappa G\, d\lambda \Rightarrow T^4 = \frac{1}{4\sigma_B \kappa_P} \left(\mathcal{S} + \int_0^\infty \kappa G\, d\lambda \right) \tag{1.20}$$

where κ_P is the Planck mean absorption coefficient, defined as

$$\kappa_P = \frac{\pi}{\sigma_B T^4} \int_0^\infty \kappa(\lambda) I_b(T, \lambda)\, d\lambda. \tag{1.21}$$

It is clear that there exists only one temperature for which equation 1.20 can hold, so the temperature is well determined.

1.6 Solution methods for the radiative heat transfer

Once the radiation heat transfer phenomenology has been well posed, a brief overview of some analytical and numerical techniques to take into account radiative heat transfer, either solving the RTE or not, is hereinafter presented, in order of increasing complexity. The Radiosity-Irradiosity Method, RIM, suitable for transparent medium only, is explained in detail in chapter 2, and the Discrete Ordinates Method, DOM, in chapter 3.

1.6.1 Diffusion approximation

Diffusion approximation applies when the optical depth of a medium is high. Under these circumstances, radiation becomes a local phenomenon, meaning that the mean free path of a photon, related to $1/\beta$, is much smaller than the size L of the domain considered. Using the analytical solution obtained in A.1, expressed in terms of the optical depth τ, can be written as (see [22], page 485)

$$\begin{aligned} q(\tau) &= 2\sigma_B \left(T_1^4 E_3(\tau) - T_2^4 E_3(\tau_L - \tau)\right) + \\ &\quad +2\pi \int_0^{\tau} S(\tau') E_2(\tau - \tau')\, d\tau' + 2\pi \int_{\tau}^{\tau_L} S(\tau') E_2(\tau' - \tau)\, d\tau', \end{aligned} \tag{1.22}$$

where the bounding walls are considered black ($\varepsilon = 1$), at temperatures T_1 and T_2, and the medium isotropically scattering. Thus we can perform the angular integration, which leads to the exponential integral functions E_2 and E_3 (see Modest [22], p. 799). In the above equation, we will neglect the wall contribution, i. e., the non integral terms, which is consistent with our assumption of high optical thickness. Also a integration variable change is performed: the integrals are carried out over the argument of the E_2 functions. Furthermore, the upper integration limit is substituted by infinity since we are interested on that limit. Therefore, the heat flux is approximated by

$$q(\tau) \simeq 2\pi \int_0^{\infty} E_2(\zeta) \left[S(\tau - \zeta) + S(\tau + \zeta)\right] d\zeta \simeq -4\pi \frac{dS}{d\tau} \int_0^{\infty} \zeta E_2(\zeta)\, d\zeta. \tag{1.23}$$

The last integral equals $1/3$. Furthermore, in this limit and under the assumption of isotropical scattering, the source function S is simply the black body intensity I_b (see [22], p. 487). Restoring the geometrical length, using that $d\tau = \beta\, d\ell$, the radiative heat flux in this approximation is

$$q(\ell) \simeq -\frac{4\pi}{3\beta_R} \frac{dI_b}{dT} \frac{dT}{d\ell} = -k_R \frac{dT}{d\ell}, \tag{1.24}$$

which is the same equation of the conductive heat transfer (the last equation has also been integrated over the wavelength). The k_R may be understood as a temperature dependent thermal conductivity, and is simply $k_R = 16\sigma_B T^3/3\beta_R$, where β_R is known as the Rosseland mean extinction coefficient, and is defined as

$$\frac{1}{\beta_R} = \frac{\pi}{4\sigma_B T^3} \int_0^\infty \frac{1}{\beta} \frac{\partial I_b}{\partial T} \, d\lambda. \tag{1.25}$$

Some effects of the fact that, at high optical depths, radiation transport ressembles conduction transport, are explored in chapter 5, by calculating independently radiative and convective contributions and adding up to obtain the final result.

Since we neglected the influence of the boundaries on the deduction of equation 1.24, this approximation is expected to fail near the boundaries. In a work by Lee and Viskanta [24] the diffusion approximation is compared to the DOM. According to this work, the heat fluxes are fairly well predicted (except near the boundaries), and for large optical thickness they judge that diffusion approximation predicts more realistic results.

1.6.2 Spherical harmonics decomposition

The intensity radiation field depends on the location $\mathbf{r}$ as well as on the direction $\hat{\mathbf{s}}$. Therefore it is natural to think of a separate spatial and angular dependence of the intensity radiation field. Any function defined on the unit sphere is properly described by the spherical harmonics. The phase function is also written in a spherical harmonic basis, by means of equation 1.11. Explicitly, we consider

$$I(\mathbf{r}, \hat{\mathbf{s}}) = \sum_{l=0}^{\infty} \sum_{m=-l}^{l} i_{lm}(\mathbf{r}) Y_{lm}(\hat{\mathbf{s}}), \tag{1.26}$$

where the $i_{lm}(\mathbf{r})$ are functions to be determined, and that cause the intensity radiation field to verify the radiative transfer equation. So far, no approximation has been made, hence this method is of little use. The usual approach is to limit the highest order of the spherical harmonic, i. e., by carrying the above summation from $l = 0$ to $l = N$. This truncated expansion of the intensity is plugged into equation 1.9 and a differential equation for the $i_{lm}(\mathbf{r})$ is obtained. The angular integrals are carried out by using the orthogonality properties of the spherical harmonics. This method is known as the P_N approximation.

By using the P_1 approximation, it turns out that the intensity radiation field must have the simplest direction dependence possible. This forces the intensity to be

$$I(\mathbf{r}, \hat{\mathbf{s}}) = a + \mathbf{b} \cdot \hat{\mathbf{s}} = \frac{1}{4\pi}(G + 3\mathbf{q}_r \cdot \hat{\mathbf{s}}), \tag{1.27}$$

where G is the total incident energy and $\mathbf{q}_r$ is defined by equation 1.15. Notice that, again, the radiative transfer equation does not have to be solved, since we already know the intensity radiation field. Inserting the intensity radiation field in this particular form on the RTE, equation 1.9, multiplying by the direction vector $\hat{\mathbf{s}}$, and integrating over the solid angle, we can relate G and $\mathbf{q}_r$, obtaining

$$\boldsymbol{\nabla} G = -3\beta \mathbf{q}_r, \tag{1.28}$$

where β is the extinction coefficient, and isotropical scattering has been assumed. Plugging this relation into energy equation 1.19, and after some manipulation, we can obtain an equation for the incident energy G. We can interpret this equation on a spectral basis or being wavenumber integrated already. For an homogeneous medium, it reads

$$\nabla^2 G - 3\beta^2(1-\omega)G = -12\pi\beta^2(1-\omega)I_b. \tag{1.29}$$

in the absence of additional heat sources. If other heat sources are present, equation 1.14 should be used. In the above equation ω stands for the scattering albedo.

The boundary conditions for this equation comes from substituting the explicit intensity radiation field in this approximation into the boundary conditions, equation 1.13. If the surfaces are taken to be diffuse and opaque (i. e., with the transmissivity set to zero, and emissivity $\varepsilon = 1 - \rho_d - \rho_s$), it can be seen that (Modest [22], p.515), under this approximation, the boundary condition becomes

$$-\frac{2(2-\varepsilon)}{3\varepsilon}\hat{\mathbf{n}} \cdot \boldsymbol{\nabla} G + G = 4\pi I_b. \tag{1.30}$$

Using this approximation, we avoid to solve the RTE with all its directional coupling via the in scattering integral. However, the P_1 method is only reliable for optically thick media. This method was used by Draoui et al. [25] to couple radiation in participating media with natural convection in square cavities. Mengüç and Viskanta [26] used the P_1 and P_3 approximations in three dimensional enclosures. Approximations beyond P_3 are very complex and present no significant advantage over other methods such as the DOM. This method is useful if analytical solutions are required to study limiting cases, for example.

1.6.3 Ray tracing methods

Ray tracing methods are purely computational, opposed to the diffusion approximation and the spherical harmonics decomposition, which allow a qualitative analysis of the problem under consideration. The domain is divided in a number of surfaces, and a number of photons, evenly distributed along each surface, are shot, in a random direction, and according to the emissive properties of that surface. Photons of all energies are emitted.

Each emitted photon is tracked, and depending on the medium where this photon is propagating, such photon will be absorbed or scattered with a certain probability, per unit length. If a photon is absorbed within the medium, the energy of the control volume on which the absorption occurs will increase in the ammount of the energy of the photon. Otherwise, the photon will hit a surface element, with defined surface properties, and may then be reflected (either specularly or diffusely), absorbed or transmitted. Given the random nature of this method, it is also called Monte Carlo method.

This method is well suited for problems where radiation is the dominant mode of heat transfer, but its coupling to convective heat transfer is not as immediate as for other methods based on the solution of the RTE. However, it allows complicated geometries, as wall as complex models for the optical properties, with virtually no compuational time increase. Tessé et al. [27] successfully used the Monte Carlo method to take into account turbulence-radiation interaction in a sooty flame.

1.7 Conclusions

In this chapter, an overview of radiative heat transfer is given. The fundamental magnitude used to describe radiation, the intensity radiation field, is defined, and it is explained how to obtain energy fluxes from it. Also, a brief description of black body radiation is performed. The fundamental radiative properties of surfaces, namely the absorptivity, emissivity, transmissivity, and reflectivity, are discussed. Next, the fundamental, Boltzmann type equation, that determines the intensity radiation field, is presented, and its directional nature is highlighted. This is known as the radiative transfer equation. For problems that are radiation dominated, the energy equation, which will allow to determine the temperature field, is to be considered.

Finally, several methods to solve the RTE are explained. The first two being approximative methods, which permit to perform quick analytical analysis for limiting cases. The last method is a purely computational one, but it is very well suited for parallelization and irregular geometries.

References

[1] P. J. Coelho and M. G. Carvalho. A conservative formulation of the discrete transfer method. *Journal of Heat Transfer*, 119(1):118–128, 1997.

[2] W. A. Fiveland. Discrete-ordinates solutions of the radiative transport equation for rectangular enclosures. *Journal of Heat Transfer*, 106:699–706, November 1984.

[3] Seung Wook Baek and M. Y. Kim. Modification of the Discrete Ordinates Method in an axisymmetric cylindrical geometry. *Numerical Heat Transfer, Part B*, 31:313–326, 1997.

[4] L. B. Barrichello and C. E. Siewert. A new version of the discrete ordinates method. In *Proceedings of the* 2^{nd} *International Conference on Computational Heat and Mass Transfer*, October 2001.

[5] H. Cha and T. H. Song. Discrete ordinates interpolation method applied to irregular three-dimensional geometries. *Journal of Heat Transfer*, 120(4):823–827, November 2000.

[6] G. D. Raithby and E. H. Chui. A finite volume method for predicting radiant heat transfer in enclosures with participating media. *Journal of Heat Transfer*, 112:415–423, 1990.

[7] Shigenao Maruyama and T. Aihara. Radiation heat transfer of arbitrary three-dimensional absorbing, emitting and scattering media and specular and diffuse surfaces. *Journal of Heat Transfer*, 119(1):129–136, 1997.

[8] P. J. Coelho and J. Gonçalves. Parallelization of the finite volume method for radiation heat transfer. *Int. J. Num. Meth. Heat Fluid Flow*, 9(4):388–404, 1999.

[9] Gautham Krishnamoorthy, Rajesh Rawat, and Philip J. Smith. Parallel computations of nongray radiative heat transfer. *Numerical Heat Transfer, Part B*, 48(2):191–211, 2005.

[10] J. G. Marakis, J. Chamiço, G. Brenner, and F. Durst. Parallel ray tracing for radiative heat transfer. 11(7):663–681, 2001.

[11] P. J. Coelho. Numerical simulation of radiative heat transfer from non-gray gases in three-dimensional enclosures. *J. Quant. Spectrosc. Radiat. Transfer*, 74(3):307–328, 2002.

[12] Fengshan Liu, Hongsheng Guo, and Gregory J. Smallwood. Effects of radiation model on the modeling of a laminar coflow methane/air diffusion flame. *Combustion and Flame*, 138:136–154, 2004.

[13] Hongsheng Guo, Yiguang Ju, and Takashi Niioka. Effects of radiative heat loss on the extinction of counterflow premixed H_2-air flames. *Combust. Theory Modelling*, 4(4):459–475, 2000.

[14] Claudio Mesyngier and Bakhtier Farouk. Turbulent natural convection - nongray gas radiation analysis in a square enclosure. *Numerical Heat Transfer, Part A*, 29:671–687, 1996.

[15] L. H. Liu, X. Xu, and Y. L. Chen. On the shapes of the presumed probability density function for the modeling of turbulence-radiation interactions. *J. Quant. Spectrosc. Radiat. Transfer*, 87(3–4):311–323, 2004.

[16] P. J. Coelho, O. J. Teerling, and D. Roekaerts. Spectral radiative effects and turbulence/radiation interaction in a non-luminous turbulent jet diffusion flame. *Combustion and Flame*, 133(1–2):75–91, 2003.

[17] A. Yu. Snegirev. Statistical modeling of thermal radiation transfer in buoyant turbulent diffusion flames. *Combustion and Flame*, 136:51–71, 2004.

[18] Jean François Sacadura. Radiative heat transfer in fire safety science. *J. Quant. Spectrosc. Radiat. Transfer*, 93(1–3):5–24, 2005.

[19] David Lacroix, Nacer Berour, Pascal Boulet, and Gérard Jeandel. Radiative and conductive heat transfer in a nongrey semitransparent medium. Application to fire protection curtains. *J. Quant. Spectrosc. Radiat. Transfer*, 86(1):9–30, 2004.

[20] S. T. Thynell. Effect of linear anisotropic scattering on spectral emission from cylindrical plumes. *Journal of Thermophysics and Heat Transfer*, 6(2):224–231, 1992.

[21] Fengshan Liu, H. A. Becker, and Y. Bindar. A comparative study of radiative heat transfer modelling in gas-fired furnaces using the simple grey gas and the weighted-sum-of-grey-gases models. *Int. J. Heat and Mass Transfer*, 41(22):3357–3371, 1998.

[22] Michael F. Modest. *Radiative Heat Transfer*. McGraw Hill, 1993.

[23] G. Colomer, J. Cadafalch, and M. Costa. Numerical study of a solar collector. In *Proceedings of the Forum International Sur les Energies Renouvelables*, volume I, pages 66–71, 2002.

[24] K. H. Lee and R. Viskanta. Two-dimensional combined conduction and radiation heat transfer: comparison of the discrete ordinates method and the diffusion approximation methods. *Numerical Heat Transfer, Part A*, 39:205–225, 2001.

[25] Abdeslam Draoui, Francis Allard, and Claudine Beghein. Numerical analysis of heat transfer by natural convection and radiation in absorbing, emitting and scattering fluids enclosed in square cavities. *Heat and Technology*, 10(1–2):160–177, 1992.

[26] M. P. Mengüç and R. Viskanta. Radiative transfer in three-dimensional rectangular enclosures containing inhomogeneous, anisotropically scattering media. *J. Quant. Spectrosc. Radiat. Transfer*, 33(6):533–549, 1985.

[27] Lionel Tessé, Francis Dupoirieux, and Jean Taine. Monte Carlo modelling of radiative transfer in a turbulent sooty flame. *Int. J. Heat and Mass Transfer*, 47(3):555–572, 2004.

2

The Radiosity Irradiosity Method

Numerical results using the method described in this chapter have been published in

G. Colomer, M. Costa, R. Cònsul and A. Oliva. Radiant exchange in domains with obstacles using the discrete ordinates method. In *Proceedings of the fifth European Congress on Computational Methods in Applied Sciences and Engineering* (ECCOMAS), pages 1–20, 2000.

2.1 Introduction

The simplest case of radiative heat transfer appears when the medium properties are such that the approximation of non participating media applies. It is worth noting that the capability of any media to interact with the photons depends not only on the media, but also on the volume occupied by it. For instance, a mass of air that fills a $1m^3$ box (at a pressure of $1atm$) can be considered transparent, while a much larger volume of air, like the atmosphere, is certainly not transparent.

In such cases, where we have a number of surfaces surrounding a media that can be considered transparent, the radiosity-irradiosity method, or RIM, can be used to evaluate the radiative heat exchange between the bounding surfaces. The RIM involves the implicit assumption of diffuse surfaces, i. e., the ammount of photons emitted (or absorbed) by a surface does not depend on the direction of the emerging (or incoming) photons. Non metallic surfaces, for example, show a constant emissivity for a large range of angles, and the emissivity vanishes for directions tangent to the surface. Metals present a wider variation, altouhg emissivity is in general very low. The diffuse emission is, therefore, a good assumption in general. According to section 1.3.2, the reflectivity is related to the emissivity by $\rho = 1 - \varepsilon$ for opaque surfaces, and therefore the assumption of diffuse surfaces is often a good approximation of the behavior of real surfaces.

The main advantage of the RIM is that we do not need to solve the radiative transfer equation 1.9. The problem of finding the intensity radiation field is diverted to calculate a set of purely geometrical entities (purely geometrical due to the diffuse behavior of the surfaces) that depend only on the relative location and orientation of the surfaces of the analyzed domain. Those geometrical entities are called view factors, or form factors, and represent the fraction of energy that is emitted by one surface and intercepted by another. More precisely,

$$F_{dA_1 \to dA_2} \equiv \frac{\text{energy emitted by } dA_1 \text{ intercepted by } dA_2}{\text{total energy emitted by } dA_1} \tag{2.1}$$

where dA_i is an infinitesimal surface. Since the photons are assumed to travel along straight paths, if a photon leaving dA_1 hits the surface dA_2, a photon leaving dA_2 is capable to hit dA_1. Therefore, the total energy leaving dA_1 and is intercepted by dA_2, that is, $F_{dA_1 \to dA_2} dA_1$, can be viewed as energy leaving dA_2 and intercepted by dA_1, that is, $F_{dA_2 \to dA_1} dA_2$. Therefore, the so-called reciprocity law states that

$$dA_1 F_{dA_1 \to dA_2} = dA_2 F_{dA_2 \to dA_1}. \tag{2.2}$$

For any given surface elements, i and j, the vector $\mathbf{s}_{ij}$ is defined as the vector joining the center of the two elements, and the vectors $\hat{\mathbf{n}}_i$ and $\hat{\mathbf{n}}_j$ are defined as the normals to each surface. Then, the view factor is

$$F_{dA_i \to dA_j} = \frac{(\hat{\mathbf{n}}_i \cdot \mathbf{s}_{ij})(\hat{\mathbf{n}}_j \cdot \mathbf{s}_{ij})}{\pi(\mathbf{s}_{ij} \cdot \mathbf{s}_{ij})^2} dA_j. \tag{2.3}$$

In order to find the view factor between two finite areas, we just have to integrate the above equation. Defining θ_i (resp. θ_j) as the angles between $\hat{\mathbf{n}}_i$ (resp. $\hat{\mathbf{n}}_j$) and the vector $\mathbf{s}_{ij}$ that expresses the relative location of the surfaces, the view factor between finite areas results in

$$F_{A_i \to A_j} = \frac{1}{A_i} \int_{A_j} \int_{A_i} \frac{\cos\theta_i \cos\theta_j}{\pi \mathbf{s}_{ij}^2} dA_i dA_j. \tag{2.4}$$

Care must be taken when using finite areas. In particular, the emission of the area must be homogeneous, meaning that the whole area is isothermal. It is possible to divide an isothermal area to refine the calculations, resulting, however, in an increased number of view factors to compute.

Thinking again in terms of energy emitted by surfaces, it is clear that the energy emitted by a surface dA_i will be intercepted by another surface, since the enclosed medium is transparent. This fact is highlighted in the conservation equation

$$\sum_{j=1}^{N} F_{i \to j} = 1 \;\; \forall i, \tag{2.5}$$

where N is the total number of surfaces.

2.2 The radiosity equation

Once the view factors are defined and calculated, it is possible to make an energy balance for each surface, which will relate the energy emitted by one surface to the energy emitted by the others. The radiosity of a surface, j_k, is defined as the energy that leaves the surface per unit area. Recalling the definition of the emissivity and reflectivity, the radiosity can be expressed as

$$j_k = \varepsilon_k E_{b,k} + \rho_k g_k, \tag{2.6}$$

where $E_{b,k}$ is the black body emission at T_k, the temperature of surface k.

The total incident energy on surface k, G_k, is the sum of the energy emitted by all surfaces that is intercepted by surface k. Given the definitions of view factors and radiosity, it is clear that surface l, with area A_l, contributes to G_k with the amount $F_{l \to k} j_l A_l$. By using the reciprocity law, equation 2.2, the irradiosity g_k, defined as the incident energy on surface k (G_k), per unit area, reads

$$g_k = \sum_{l=1}^{N} F_{k \to l} j_l. \tag{2.7}$$

For N surfaces, equations 2.6 and 2.7, define a linear system with N unknowns, the radiosities j_k. Once this system is solved, the total heat flux, per unit area, is simply $q_k = j_k - g_k$. Considering the total heat flux $Q_k = A_k q_k$, and the conservation equation 2.5, it is possible to show that, indeed, energy is conserved, i. e.,

$$\sum_{k=1}^{N} Q_k = 0. \tag{2.8}$$

The above definitions of radiosity and irradiosity, and also the energy conservation, are valid for each spectral range we consider. In engineering and solar equipment applications, usually two ranges are considered: the thermal band, and the solar band. Moreover, the black body emission $E_{b,k}$ in equation 2.6 is considered to be $\sigma_B T_k^4$ for the thermal band and zero for the solar band.

2.3 View factors in cylindrical coordinates

In the simplest case of two dimensional geometries, that is, a section of a three dimensional domain with one dimension much larger than the other two, the view factors can be calculated in a closed form using the method of crossed strings by Hottel (see for example [1], p. 178). For a general three dimensional geometry there is not any useful analytical expression for the view factors, except for a few cases with rectangular areas which are parallel or orthogonal. Therefore, in general, the view factors must be calculated by numerical integration.

In the present work, cylindrical geometries with an axis of symmetry are considered. Despite the fact that those geometries can be described by only two coordinates, they are in fact three dimensional domains, and have to be dealt with as such. Thus, in principle, expensive numerical computations are required to calculate the view factors. There are only two kinds of areas in this geometry: rings of infinitesimal height dz, or hollow disks of infinitesimal radius dr. Each area is divided in a number of angular elements, dA_i for the disk, and dA_j for the ring, as depicted in figure 2.1.

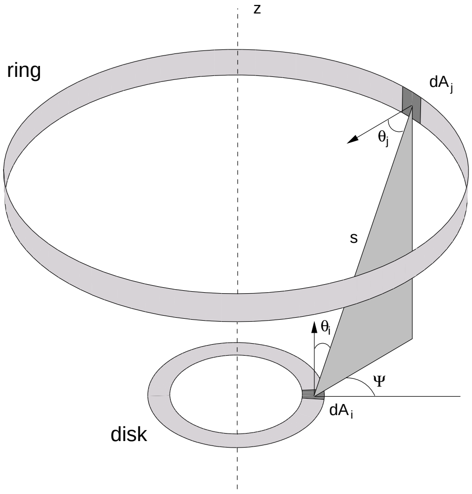

Figure 2.1: Two elementary surfaces in cylindrical geometry. The domain is invariant respect any rotation around the z axis.

Our goal is to calculate the view factor between the whole disk and the whole ring. That is,

$$F_{A_i \to A_j} = \frac{1}{A_i} \int F_{dA_i \to A_j} dA_i,$$

where the integral runs over 0 and 2π along the ring, i. e., the angle Ψ in the figure. However, if a symmetry axis exists (and in this case is the z axis), the view factor $F_{dA_i \to A_j}$ is the same for each elementary area dA_i; hence, for this particular case, it is true that $F_{A_i \to A_j} = F_{dA_i \to A_j}$. Thus, instead of numerically calculate two integrals, it suffices with only one numerical integration. The remaining integral is, taking into account equation 2.4,

$$F_{A_i \to A_j} = F_{dA_i \to A_j} = dS \int_0^{2\pi} \frac{\cos\theta_i \cos\theta_j}{\pi s^2} \, d\Psi, \tag{2.9}$$

where $s \equiv |\mathbf{s}_{ij}|$. Also dC is a shortcut for

$$dS = \begin{cases} rdr & \text{if } \hat{\mathbf{n}} \parallel \hat{\mathbf{k}} \\ rdz & \text{if } \hat{\mathbf{n}} \perp \hat{\mathbf{k}} \end{cases}$$

being $\hat{\mathbf{k}}$ the unitary vector parallel to the symmetry axis z.

The angles θ_i and θ_j, as well as the distance $\mathbf{s}_{ij}$ of the two elementary areas dA_i and dA_j, are assumed constant within each elementary area. The actual values for the angles and the distance used, are those that correspond to the middle point of each surface. The main drawback that we must face when using numerical integration is that the results for two areas that are in contact are not well calculated, since the constant angles and distance assumption does not hold.

Finally, the problem of calculating the view factor in cylindrical coordinates is reduced to the integral 2.9. By symetry, only the integral between 0 and π has to be calculated. In order to achieve a good precision, we need to divide the interval $[0, \pi]$ in a sufficently large number of steps. In this work, however, equation 2.9 has been solved by means of a more efficient, Gaussian like, quadrature method, which roughly consists on the following approximation (more details on Gaussian integration can be found in section B.1):

$$\int_a^b \omega(x) f(x) dx \sim \sum_i \omega_i f_i,$$

with the weights ω_i depending on the weighting function ω and the integration interval. For the specific case on which we are interested, the approximate value of the integral, calculated with a summation of $m + 1$ terms, is given by

$$\int_0^{\pi} f(\theta) d\theta \sim \frac{\pi}{m+1} \sum_{k=0}^{m} f\left(\frac{(2k+1)\pi}{2(m+1)}\right). \tag{2.10}$$

It turns out that, when evaluating the integral 2.9 in this way, the view factors so obtained are closer to the analytical values, and are obtained with less computational effort. When calculating the integral numerically, we should define the angular refinement $\Delta\Psi$, to give to each elementary surface dA_i a precise value for its area. We could think that the number of terms of the approximation and this $\Delta\Psi$ are related; however, numerical experiments show that the final results almost do not depend on $\Delta\Psi$. Thus, the computation time is the same whatever the angular refinement.

The values that the algorithm uses, which gives satisfactory results when compared to analytical solutions, are $m = 70$ and $\Delta\Psi = \pi/200$.

For a two dimensional, axial symmetric case, defined by a mesh of $n \times n$, the number of surfaces can be estimated to be $5n$, and the number of view factors to compute, with the aid of the reciprocity equation 2.2, approximately $25n^2/2$ (the total computation time is proportional to m times this number). If the same geometry is treated as three dimensional, with q angular partitions, the number of surfaces can be estimated to be $4nq$. Alas, if the constant θ_i and θ_j through the elementary area assumption must hold, the q should be of the same order of n, and the number of view factors to compute is roughly $8n^4$ (and the computation time proportional to this number). Thus,

$$\frac{t_{2\mathrm{D}}}{t_{3\mathrm{D}}} \sim \frac{m}{n^2}.$$

The finest mesh tested in the present work was a 64×64 control volumes mesh. In this particular case, then, the speedup is about 60.

The hardest part of the algorithm is to take into account all possible relative orientations of the elementary surfaces. It is important to determine if there exists any surface blocking the path between any given two surfaces (i. e., if one surface can see the other). And it is possible that a surface blocks the path for a given range of Ψ, and do not block the path for another range of Ψ. The possibility that one surface can not see itself because of a blocking obstacle should be considered also. The policy adopted is that, if there is a surface blocking the path that joins the centers of the two surfaces under consideration, those two surfaces cannot see each other, and the view factor is set to zero. The normal situation is that, even there is a blocking surface, one surface can partly see the other, so it is possible to improve the results (by increasing the computation time, but not the ratio $t_{2\mathrm{D}}/t_{3\mathrm{D}}$), by weighting the view factor depending on how much area of one surface is seen by the other.

The main source of error of the RIM is, precisely, the correct determination of the blocking faces. Thus, the results given by this method with complicated geometries are not so good. By increasing the number of surfaces one can partly overcome this limitation, but at a great expense in computational resources. A good error estimation of the view factors is to check the conservation equation 2.5. Kadinsky and Perić [2] presented a view factor correction, and and such correction ensures the energy conservation, but this is done by modifying some view factors. Such correction has been used in this thesis.

2.4 Sample calculations

With the aim of validate the numerical method to find the view factors explained in the precedent section, several problems, with known analytical solution, have been solved. The main interest in doing so is to guarantee the energy conservation, since the results concerning the radiative heat transfer, calculated with the RIM, will be incorporated to more general software, that solves the Navier-Stokes equations that describe the heat and mass transfer. This software is developped using the finite volume method technique, which imposes the energy and mass conservation for each control volume. To ensure that no unphysical energy source or sink is added, equation 2.8 is checked for several geometric configurations.

2.4.1 Concentrical cylinders

Consider two black, concentrical cylinders, with a radius of $0.5m$ and $1m$ respectively, and temperatures T_{in} and T_{out}. The length of the cylinders will be increased in order to pretend infinitely long cylinders. The radiative heat flux per unit area, from the inner cylinder to the outer, is given by

$$q_{\text{in}\to\text{out}} = F_{\text{in}\to\text{out}}\sigma_B(T_{\text{in}}^4 - T_{\text{out}}^4). \tag{2.11}$$

Explicitly, T_{in} was set to $310K$ and T_{out} to $300K$. The above expression holds if the caps of the cylinder are considered to belong to the exterior surface, that is, $F_{\text{int}\to\text{out}} = 1$. Thus, in this particular case, $q_{\text{in}\to\text{out}} = 64.3664W/m^2$. Results are given in table 2.1, where L is the length of the cylinders. As the length of the cavities increases, the calculated value approaches the theoretical one. This can be attributed to the fact that, for small L, the effects of the caps of the cylinder, where the view factors are not to well calculated, are more important. The teoretical value assumes that the heat flux along the inner cylinder is constant, thus the table presents the mean value (of heat flux per unit area) along the inner cylinder. The error of the solution, δQ_t, defined as the sum of the heat flux for all the surfaces normalized to the teoretical value, is also shown, in percentile basis.

L (m)	$\bar{q}(W/m^2)$	δQ_t (%)
1.0	64.2823	0.3
3.0	64.3136	0.2
5.0	64.3186	0.2
10.0	64.2978	0.3
20.0	64.3474	0.4

Table 2.1: Black concentrical cylinders case: Mean heat flux through inner cylinder. The meshes used are 32 × 32, 32 × 96, and 32 × 156. The error on the total heat flux, $\delta Q_t = \sum_k Q_k/q_{\text{in}\to\text{out}}$, is reported.

The calculation of the view factors has been carried out with a mesh adapted to the length of cylinders; that is, the number of control volumes along the symmetry axis has been increased as the length L does, in order to have the control volumes with approximately a square shape. This has been accomplished for lengths $L = 1m$, $3m$, and $5m$. For the $L = 10m$ case, the control volumes are stretched by a factor of two, while for $L = 20m$, the control volumes are stretched by a factor of 4. The use of the stretched control volumes implies worse calculated view factors, and in fact the error δQ_t is bigger for the two last cases, with longer cylinders.

2.4.2 Internal obstacle

Consider again two concentrical cylinders, the smallest of length $L/2$, completely included in the other, of length L. The centers of both cylinders coincide. The radius of the cylinders are the same of the previous case, $0.5m$ and $1m$ respectively. Again a theoretical value of the radiative heat flux per unit area, from the inner cylinder to the outer, can be calculated, assuming that the heat flux on the inner cylinder is constant. This implies that the inner cylinder can be treated as a unique surface, and $F_{\text{in}\to\text{out}} = 1$. By the reciprocity law, equation 2.2, we have $F_{\text{out}\to\text{in}} = A_{\text{in}}/A_{\text{out}}$, the ratio between the areas of both cylinders. Under these circumstances, and considering that the surfaces are described by emissivities ε_{in} and ε_{out}, the theoretical heat flux is

$$q_{\text{in}\to\text{out}} = \frac{\sigma_B(T_{\text{in}}^4 - T_{\text{out}}^4)}{\dfrac{1}{\varepsilon_{\text{in}}} + \left(\dfrac{1}{\varepsilon_{\text{out}}} - 1\right)\dfrac{A_{\text{in}}}{A_{\text{out}}}} \tag{2.12}$$

All the tested cases considered that $\varepsilon_{\text{int}} = \varepsilon_{\text{out}} = \varepsilon$. The temperatures of the cylinders are the same of the previous case, that is, $T_{\text{in}} = 310K$ and $T_{\text{out}} = 300K$. The mean values of the heat flux through the axial wall of the outer cylinder, for different values of the emissivity ε and length L are shown in table 2.2. In parentheses, the percentile error in the total heat flux is indicated.

	$L = 1m$	$L = 3m$	$L = 5m$	$L \to \infty$
$\varepsilon = 1.0$	64.2531 (0.2%)	64.3319 (0.1%)	64.3426 (0.1%)	64.3664
$\varepsilon = 0.8$	48.0916 (0.3%)	48.8852 (0.2%)	48.9380 (0.2%)	49.0411
$\varepsilon = 0.7$	40.8586 (0.4%)	41.7474 (0.2%)	41.8161 (0.2%)	41.9130
$\varepsilon = 0.5$	27.7499 (0.6%)	28.4737 (0.3%)	28.5498 (0.4%)	28.6073
$\varepsilon = 0.3$	16.0083 (1.0%)	16.3538 (0.6%)	16.4037 (0.7%)	16.4340

Table 2.2: Gray surfaces, concentrical cylinders. The grids used are 32 × 32, 32 × 96, and 32 × 156. Mean heat flux on the axial wall of the outer cylinder. In parentheses, the percentile error in the total heat flux is reported.

As expected, the biggest difference between the calculated and theoretical value (the one with $L \to \infty$) is for the shortest cylinder considered, $L = 1m$. Also the error in total heat flux decreases for increasing L, due to the same reason that in the previous section: the effects of the corners are less important for longer cylinders. Interesting enough, for a given length, the error increases as the emissivity ε decreases. This behavior is due to the fact that the irradiosity term, g_k, appears in the radiosity equation 2.6 multiplied by the constant $\rho_k = 1 - \varepsilon_k$. Thus, any errors committed in the calculation of the view factors will have greater influence on radiative heat transfer in cases where the emissivity of the surfaces is small.

2.4.3 Hollow cylinder

Suppose a hollow cylinder, whose surfaces can be considered to behave like a black body. The length and radius of the cylinder are $1m$, and the temperatures are $T_{\text{wall}} = 310K$ and $T_{\text{cap}} = 300K$. Under these conditions, the heat flux per unit area emitted by the wall, which is hotter, can be evaluated with the following expression:

$$q_{\text{wall}\to\text{cap}} = 2F_{\text{wall}\to\text{cap}}\sigma_B(T^4_{\text{wall}} - T^4_{\text{cap}}). \tag{2.13}$$

Again, this result is valid if the heat flux per unit area is constant throughout the wall, which is the assumption implicitly made when considering only three surfaces (the wall and the two caps) to solve this problem. To solve this problem analytically, we realize that all we need to know is one view factor due to the high symmetry of the situation. The analytical view factor is calculated using equation 2.4, which can be found tabulated in many text books (see Modest [1], p. 791). Particularly,

$$F_{\text{wall}\to\text{cap}} = \frac{\sqrt{5}-1}{4}. \tag{2.14}$$

Thus, the teoretical value for the heat flux per unit area is, in this case, $q_{\text{wall}\to\text{cap}} = 39.7806\ W/m^2$. Table 2.3 shows the mean heat flux per unit area along the cylinder wall, and the total error as defined in previous sections.

Mesh	$\bar{q}(W/m^2)$	$\delta Q_t(\%)$
16x16	39.5629	0.04
24x24	39.6355	0.01
32x32	39.6715	0.005
48x48	39.7044	0.003
64x64	39.7231	0.003

Table 2.3: Hollow cylinder case: Mean radiative heat flux through cylinder wall, and error in total heat flux.

The total heat flux error, as expected, decreases as the mesh resolution is increased. As the size of the control volumes diminishes, the number of view factors badly approximated decreases with respect the total number of view factors to be calculated. The result is that the error drops in more than one order of magnitude for the finest mesh. This is the simplest geometry we can conceive in cylindrical coordinates, yet numerical errors are present due to the corner problem when evaluating numerically the integral 2.4. Another fact becomes apparent after looking at the results of this case: in this geometry there are no blocking surfaces, thus avoiding also the problem of whether a surface sees another surface, and resulting in lower total heat flux errors, even for the coarsest mesh, than the concentrical cylinders geometry in the previous cases.

2.5 Conclusions

In this chapter, the Radiosity Irradiosity Method has been outlined, and all of the concepts relevant to the RIM have been defined. The main contents of this chapter are devoted to the introduction of a procedure to calculate, by numerical integration, the view factors between surfaces in cylindrical geometries with axial symmetry. The main difficulty when calculating the view factors is the presence of internal obstacles, which causes equation 2.5 not to be verified in its presence.

Three geometries have been solved using this procedure. Two with internal obstacles and one without. As expected, the error (measured as the percentile deviation from zero of the sum of the total heat flux over all surfaces) in the complex geometries is larger (by one to two) orders of magnitude than in the simplest configuration. Also the influence of the emissivity on the error is checked: the lower the emissivity, and therefore the larger the reflectivity, the larger the error.

References

[1] Michael F. Modest. *Radiative Heat Transfer*. McGraw Hill, 1993.

[2] L. Kadinski and M. Perić. Numerical study of grey-body surface radiation coupled with fluid flow for general geometries using a finite volume multigrid solver. *Int. J. Heat and Fluid Flow*, 6:3–18, November 1996.

3

The Discrete Ordinates Method

Parts of this chapter have been published in

G. Colomer, M. Costa, R. Cònsul and A. Oliva. Radiant exchange in domains with obstacles using the discrete ordinates method. In *Proceedings of the Fifth European Congress on Computational Methods in Applied Sciences and Engineering* (ECCOMAS), pages 1–20, 2000.

3.1 Introduction

The most general way to take into account radiative energy transfer, as stated in chapter 1, is to consider the intensity radiation field, I, which is defined as the energy due to radiation (carried by photons), propagating along a given direction $\hat{\mathbf{s}}$, that crosses a unit area normal to $\hat{\mathbf{s}}$, per unit area, unit solid angle arround $\hat{\mathbf{s}}$, unit wavelength and time. The intensity radiation field obeys the radiative transfer equation, RTE, described in section 1.4:

$$\frac{dI(\hat{\mathbf{s}})}{d\ell} = -(\kappa + \sigma_s) I(\hat{\mathbf{s}}) + \kappa I_b + \frac{\sigma_s}{4\pi} \int_{4\pi} \phi(\hat{\mathbf{s}}'; \hat{\mathbf{s}}) I(\hat{\mathbf{s}}')\, d\Omega'. \tag{3.1}$$

The medium behavior is modeled by the two properties, the absoprtion coefficient κ and the scattering coefficient σ_s. The phase function $\phi(\hat{\mathbf{s}}'; \hat{\mathbf{s}})$ accounts for the probability of a photon being redirected from direction $\hat{\mathbf{s}}'$ to direction $\hat{\mathbf{s}}$, multiplied by 4π. Recall that the most widely used boundary condition for the intensity radiation field, for a wall of given emissivity ε, and reflectivities ρ_s and ρ_d (see section 1.3.2), is

$$I_{\text{wall}}(\hat{\mathbf{s}}) = \varepsilon I_b + \rho_s(\hat{\mathbf{s}}^*) I(\hat{\mathbf{s}}^*) + \frac{1}{\pi} \int_{\hat{\mathbf{n}} \cdot \hat{\mathbf{s}} < 0} \rho_d(\hat{\mathbf{s}}) I(\hat{\mathbf{s}}) |\hat{\mathbf{n}} \cdot \hat{\mathbf{s}}|\, d\Omega, \tag{3.2}$$

where $\hat{\mathbf{n}}$ is the normal to the wall, and $\hat{\mathbf{s}}^*$ is the result of reflecting the direction $\hat{\mathbf{s}}$ with respect to the plane perpendicular to $\hat{\mathbf{n}}$. The integral is over all directions $\hat{\mathbf{s}}$ incident on the wall, hence the requirement $\hat{\mathbf{n}} \cdot \hat{\mathbf{s}} < 0$. Boundary conditions suitable for solar applications, using the DOM, are discussed in section 3.3.3.

The hard part of equation 3.1 is the last term of the right hand side, the so called in-scattering term. While the intensity radiation field is diferentiated respect to a spatial coordinate, it is integrated over all directions, thus making analytical solutions difficult to obtain in a closed form. An integral over all directions also appears in the boundary conditions. The Discrete Ordinates Method consists on evaluate such integral terms by means of a Gaussian quadrature over the solid angle. Therefore, the DOM correctly evaluates angular integrals of the intensity radiation field, but it is poorly suited to follow the track of a particular photon. If we are interested in how a medium reacts to radiation incident in a very particular direction, this method is not the most appropriate. However, concerning to heat transfer applications, the DOM is commonly used, for a wide variety of coupled convection-conduction-radiation problems [1,2,3,4].

The integrals over the solid angle that appear in equations 3.1 and 3.2 are replaced by a weighted summation of the integrand evaluated at discrete, conveniently selected, ordinates $\hat{\mathbf{s}}_i$ (section B.1 illustrates with a simple example why this is possible). The Gaussian quadrature provides the approximations

$$\int_{4\pi} \phi(\hat{\mathbf{s}}';\hat{\mathbf{s}}) I(\hat{\mathbf{s}}') d\Omega' \simeq \sum_{j=1}^{N} \omega_j I^j \phi(\hat{\mathbf{s}}_j;\hat{\mathbf{s}}_i) \tag{3.3}$$

and

$$\int_{\hat{\mathbf{n}}\cdot\hat{\mathbf{s}}<0} I(\hat{\mathbf{s}}) |\hat{\mathbf{n}} \cdot \hat{\mathbf{s}}| \, d\Omega \simeq \sum_{\hat{\mathbf{n}}\cdot\hat{\mathbf{s}}_j<0} \omega_j I^j |\hat{\mathbf{n}} \cdot \hat{\mathbf{s}}_j|, \tag{3.4}$$

where I^j is a shortcut for $I(\hat{\mathbf{s}}_j)$. Thus, the original integro-differential RTE equation becomes a system of N linear differential equations, an equation for each discretized ordinate. Moreover, defining

$$S^i = \kappa I_b + \frac{\sigma_s}{4\pi} \sum_{j\neq i} \omega_j I^j \phi(\hat{\mathbf{s}}_j;\hat{\mathbf{s}}_i) \tag{3.5}$$

$$B^i = \kappa + \sigma_s - \frac{\sigma_s}{4\pi} \omega_i \phi(\hat{\mathbf{s}}_i;\hat{\mathbf{s}}_i), \tag{3.6}$$

the problem is diverted to solve this system of differential equations:

$$\frac{dI^i}{d\ell} = -B^i I^i + S^i \qquad 1 \leq i \leq N, \tag{3.7}$$

where ℓ is a length parameter that runs along each direction defined by $\hat{\mathbf{s}}_i$.

We are interested on the energy transfer due to radiation in a variety of situations. Therefore, we must be able to calculate the radiant energy flux through a surface, and the radiant energy generation per unit volume. For this purpose, equations 1.2 and 1.19 are used. Once the Gaussian quadrature approximation is applied, these become

$$q(\hat{\mathbf{n}}) \simeq \sum_j \omega_j I^j (\hat{\mathbf{n}} \cdot \hat{\mathbf{s}}_j) \tag{3.8}$$

for the heat flux through a surface perpendicular to $\hat{\mathbf{n}}$ and

$$\boldsymbol{\nabla} \cdot \mathbf{q}_r \simeq \kappa \left(4\pi I_b - \sum_j \omega_j I^j \right) \tag{3.9}$$

for the energy source (or sink) per unit volume. The following development of the numerical methods to integrate the RTE is valid on a those ranges of the spectrum where optical properties may be assumed constant. Usually, the gray properties assumption is used, meaning that the optical properties are independant of the wavenumber, and the I_b term in equation 3.1, the black body emissivity is given by the Stefan-Boltzmann law, that is, $I_b = \sigma_B T^4 / \pi$.

3.2 Discrete ordinates selection

One of the constraints of the Gaussian quadrature with n points, is that the integral should be exact, whenever the integrand is a polynomial of a given degree, usually a degree less or equal than n. Therefore, the bigger is n, the better any non-polynomial integral is approximated, for the difference between the actual intensity and a polynomial of degree n decreases as n increases. A way to introduce this constraint is to demand that a number of integral half-moments are to be verified, that is,

$$\sum_{2\pi} \omega_j (\hat{\mathbf{\imath}} \cdot \hat{\mathbf{s}}_j)^a (\hat{\mathbf{\jmath}} \cdot \hat{\mathbf{s}}_j)^b (\hat{\mathbf{k}} \cdot \hat{\mathbf{s}}_j)^c = \int_{2\pi} \sin^b \theta \cos^{a+c} \theta \cos^a \varphi \sin^c \varphi \, d\Omega, \tag{3.10}$$

for positive values of a, b, and c, where the integral and the summation are extended to the hemisphere with positive y (see Koch et al. [5] for instance). For some values a, b, and c the above integral is zero, by symmetry. The integrand corresponds to the projections of any direction whithin the hemisphere over the three axis, raised to the powers a, b, and c for the x, y, and z axis projection. For radiation problems, our main concern is that any ordinate sets verifies the zeroth moment, that is, $a = b = c = 0$, and the first moment, $a + b + c = 1$, which correspond, respectively, to the energy source term, equation 3.9, and to the heat flux through a surface, equation 3.8. Although integral moments should be satisfied respect to every direction, this restriction is not assumible with a finite number of ordinates. Thus, we demand that the moments are to be verified only with respect to the three coordinate axis.

These constraints limit the values of the weights ω_j and ordinates $\hat{\mathbf{s}}_j$, and in practice yield to valuable ordinate sets. The higher the number of half moments verified, the better will be the integral approxmiation for any non-polynomial integrand. The reason is that we could think of the intensity radiation field, or even the phase function, expressed in terms of an infinite series using the spherical harmonics as a basis functions, as in section 1.6.2. Therefore, if the verified number of half moments is large, so is the number of spherical harmonics exactly approximated by the Gaussian quadrature, since these are linear combinations of powers of sine and cosine functions. Koch and Becker [6], after analyzing different quadrature sets, propose as the best scheme such quadrature sets that exactly integrate the spherical harmonics up to a given order.

The set of directions $\hat{\mathbf{s}}_i$ is highly symmetrical, in the sense that it is defined only for the octant with positive values of x, y, and z. For the other octants, the corresponding ordinates are obtained by reflection. Figure 3.1 shows the characterization of any direction with the polar and azimuthal angles θ_i and φ_i. For one dimensional problems, the ordinates $\hat{\mathbf{s}}_i$ are defined on one quadrant, with $\varphi_i = 0$. There are also sets available for two dimensional geometries that are also defined in a quadrant: all ordinates lie on the same plane.

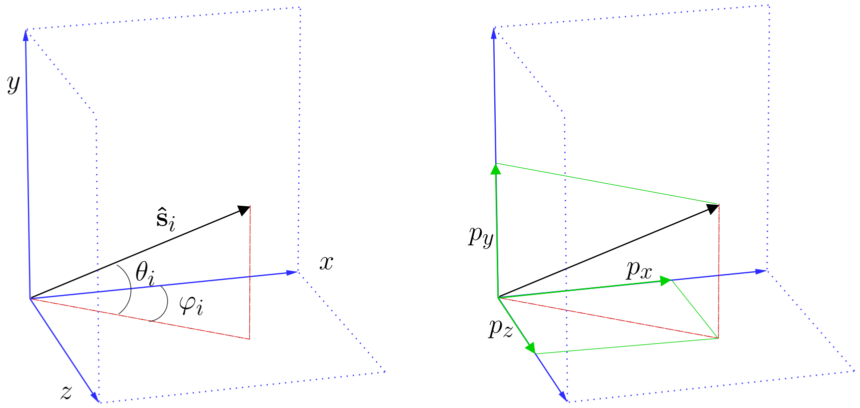

Figure 3.1: Angular definition convention used in this work, and definition of the ordinate $\hat{\mathbf{s}}_i$ (left). The projections over the three axis are highlighted in green (right)

The choice of a suitable set of ordinates is a key aspect of the DOM. Such a set is acceptable if it guarantees, at least, the energy conservation condition; i. e., it gives an exact value for the first moment of the intensity field integrated over half of the solid angle. Sànchez and Smith [7] proposed a simple, constant weight, scheme, defined on a single plane, suitable for one or two dimensional problems:

$$\theta_i = \frac{\pi}{4N}(2i-1) \quad 1 \leq i \leq N \tag{3.11}$$

$$\omega = \frac{\pi}{2\sum_{i=1}^{N}\cos\theta_i} = \pi \sin\frac{\pi}{4N}. \tag{3.12}$$

Here, N is the number of directions per quadrant, and θ_i is the angle between the x axis and the direction $\hat{\mathbf{s}}_i$. It is worth noting that this set does not verify the zeroth moment, and thus must not be used for scattering media or radiative equilibrium calculations, where the exact value of the integral of the intensity over the solid angle, that is, the zeroth moment, is required.

More general sets, usable for both two and three dimensional geometries, are not so simply described. In general, in order to find the most general set that is maximally symmetric, i. e., invariant under rotations of 90 degrees, we pick one direction, $\hat{\mathbf{s}}_1$ in the first octant, that will act as a generator of a group of ordinates. We consider the projections along the three axis, p_x, p_y, and p_z, for this particular direction. Our aim is to find other directions, two or five more, such the projections along the three axis of these newly found directions are the permutations of p_x, p_y and p_z: for instance, the projection of $\hat{\mathbf{s}}_2$ along x axis could be p_y, and the projection along the y axis, p_x, the projection of $\hat{\mathbf{s}}_2$ along the z axis remaining the same of $\hat{\mathbf{s}}_1$. We will be able to find a group of three directions (if two of the original projections are equal) or a group of six directions (if all the three projections are different). Such groups must always be considered together. There is a group which contains only one direction, $\hat{\mathbf{s}}_0$, the one with $\varphi = \pi/4$ and $\theta = \arctan(1/\sqrt{2})$. In this particular case, all the projections are equal to $1/\sqrt{3}$. These sets are called DCT on the literature, and are also described in [5].

Given the generator φ_1, θ_1, it is possible to find out what the remaining elements of the group are. In the general case where the group has six elements, these are $\theta_2 = \theta_1$, $\varphi_2 = \pi/2 - \varphi_1$, $\theta_3 = \arcsin(\cos\theta_1\cos\varphi_1)$, $\varphi_3 = \arctan(\tan\theta_1/\sin\varphi_1)$, $\theta_4 = \arcsin(\cos\theta_1\sin\varphi_1)$, $\varphi_4 = \arctan(\tan\theta_1/\cos\varphi_1)$, $\theta_5 = \theta_4$, $\varphi_5 = \pi/2 - \varphi_4$ and $\theta_6 = \theta_3$, $\varphi_6 = \pi/2 - \varphi_3$. All the directions of a given group lie in the same plane, and in fact all the ordinates are at the same distance from $\hat{\mathbf{s}}_0$. If the symmetry condition has to be verified, the weight must be the same for each member of the group. If only one group is considered, the weight is chosen in a way that the first integral moment is verified, that is,

$$4\omega\sum_{i=1}^{N} p_x^i = \pi \tag{3.13}$$

where p_x^i is the projection of the ith ordinate along the x axis, and N is the number of directions of the group. Clearly, the same ω will be obtained considering p_y^i (or

p_z^i). In order to verify also the zeroth moment, another group should be added. As the number of groups is increased, the number of half moments verified rises. There is one degree of freedom when choosing the ordinates in this way, that is, the generator direction. There are no hints of which generators are worthy, being this the major drawback of this method. The group generated by $\varphi_1 = \theta_1 = \pi/3$, which has six ordinates, gives good results, compared to analytical solutions. The ordinate set obtained as described above was seldom used, due mainly to the degree of freedom it has (namely the $\hat{\mathbf{s}}_1$ direction), and to the availability of other ordinate sets.

The most widely used ordinate sets are the so called S_n sets, which are obtained imposing constraints on the moments that these sets should verify (see section B.3). There are several kinds of S_n sets; sets that verify only even moments, sets verifying sequential moments, sets verifying unordered moments (although zeroth and first moment are always verified)…

Götz [8] gives an extensive review of such different ordinate sets, and the set constraints are explained by Fiveland [9]. However, the number of ordinates of the S_n type is low, implying a sensible ray effect. Moreover, the S_n sets are hard to obtain for large n. For this reason, the T_n set, developped by Thurgood et al. [10], is also used, and it is easily generated for any given order. However, the number of T_n ordinates that should be used in order to achieve the same precision of the S_n ordinates is larger, resulting in a more expensive computational cost. This is due to the fact that the first moment is not exactly accomplished by the T_n, altgough the error decreases as the order increases. In fact, the T_n quadrature set verifies only the zeroth and second moment. Both the S_n and the T_n verify the symmetry conditions discussed before.

So as to give an idea of how such ordinate sets look like, the ordinate set corresponding to the S_{10} is shown in table 3.1, valid for two dimensional problems. In three dimensional problems, the ordinates are the same, but the weights are divided by 2. For this particular set, the moments verified are those with $a = \{0, 1, 2, 5, 8, 10\}$, $b = c = 0$ in equation 3.10, while all the nonzero moments, with $a + b + c \leq 7$, are well approximated, with a maximum error of 3.6% for the case $a = b = c = 2$.

3.3 Solving the differential equations

The integral in the equation 3.1 has been substituted, with the aid of the Gaussian quadrature, by a summation that links simple linear differential equations, one for each ordinate $\hat{\mathbf{s}}_i$. These differential equations may be solved by using a variety of techniques.

In this work, the finite volume technique is employed. Such technique is chosen because, on the long term, it is intended to solve the coupling of radiative and other heat transfer phenomena, namely conductive and convective energy transfer,

Ord.	p_x	p_y	p_z	ω
$\hat{\mathbf{s}}_1$	0.1372719331279688	0.9809754496166665	0.1372719331279688	$1.8888232000589797e-1$
$\hat{\mathbf{s}}_2$	0.1372719331279688	0.1372719331279688	0.9809754496166665	$1.8888232000589797e-1$
$\hat{\mathbf{s}}_3$	0.9809754496166665	0.1372719331279688	0.1372719331279688	$1.8888232000589797e-1$
$\hat{\mathbf{s}}_4$	0.7004128840817093	0.1372719331279490	0.7004128840817092	$3.4740434059426763e-2$
$\hat{\mathbf{s}}_5$	0.7004128840817092	0.7004128840817092	0.1372719331279493	$3.4740434059426763e-2$
$\hat{\mathbf{s}}_6$	0.1372719331279494	0.7004128840817092	0.7004128840817092	$3.4740434059426763e-2$
$\hat{\mathbf{s}}_7$	0.5046889100289156	0.7004128840817038	0.5046889100289156	$2.2999433124904400e-1$
$\hat{\mathbf{s}}_8$	0.5046889100289156	0.5046889100289156	0.7004128840817038	$2.2999433124904400e-1$
$\hat{\mathbf{s}}_9$	0.7004128840817038	0.5046889100289156	0.5046889100289155	$2.2999433124904400e-1$
$\hat{\mathbf{s}}_{10}$	0.1372719331279505	0.8523177344565439	0.5046889100289205	$2.9679023294111218e-1$
$\hat{\mathbf{s}}_{11}$	0.5046889100289206	0.1372719331279504	0.8523177344565438	$2.9679023294111218e-1$
$\hat{\mathbf{s}}_{12}$	0.8523177344565439	0.1372719331279504	0.5046889100289206	$2.9679023294111218e-1$
$\hat{\mathbf{s}}_{13}$	0.5046889100289205	0.8523177344565439	0.1372719331279504	$2.9679023294111218e-1$
$\hat{\mathbf{s}}_{14}$	0.1372719331279504	0.5046889100289205	0.8523177344565440	$2.9679023294111218e-1$
$\hat{\mathbf{s}}_{15}$	0.8523177344565440	0.5046889100289205	0.1372719331279503	$2.9679023294111218e-1$

Table 3.1: Two dimensional S_{10} ordinates set. Four groups, with constant weight each, are present. The projections along the axis are indeed permuted within each group. There are little differences, but only in the last digits of the projections.

for which a finite volume formulated computational code is available. Thus, we proceed to divide the domain in a number of non overlapping control volumes, and to integrate equation 3.7 over such control volume, assuming that the intensity is constant inside the control volume. Repeating the integration for all the control volumes, we end up with a system of algebraic equations, whose solution gives the intensity at each point, and for a particular ordinate $\hat{\mathbf{s}}_i$. So, in fact, we will have to solve N such algebraic systems, coupled by the in-scattering term and, in general, also by the boundary conditions. We can work out the right hand side of equation 3.7, which is independant of the coordinates choosen to describe the problem. This yields

$$V(-B^i I^i + S^i), \tag{3.14}$$

where V is the volume of the control volume, since all magnitudes inside are assumed constant. The difficult part, in non cartesian coordinates, is the left hand side of RTE, in which derivatives with respect to the angles defining the direction $\hat{\mathbf{s}}_i$ will appear. In the present work, it is explained in detail how to handle the cases of cartesian and cylindrical coordinates. The complication arises by the fact that we are assuming that radiation propagates along straight lines, and the cartesian coordinates are the only ones well suited for such cases.

3.3.1 Discretization in cartesian coordinates

The left hand side of the RTE is to be understood as the variation of the intensity in direction $\hat{\mathbf{s}}_i$ along the propagation path. In rectangular geometries, well described by cartesian coordinates, this derivative along the path is simply

$$\frac{dI^i}{d\ell} = \mu_i \nu_i \frac{\partial I^i}{\partial x} + \mu_i^* \frac{\partial I^i}{\partial y} + \mu_i \nu_i^* \frac{\partial I^i}{\partial z} \tag{3.15}$$

where $\mu_i = \cos\theta_i$, $\nu_i = \cos\varphi_i$, $\mu_i^* = \sin\theta_i$, and $\nu_i^* = \sin\varphi_i$. As stated previously, this is the simplest form for the spatial variation of the intensity radiation field. There appear only derivatives with respect to the spatial coordinates x, y, and z, because the angles between the radiation path and the coordinate axis are constant. In cartesian coordinates, the control volumes are rectangular boxes, such as that on figure 3.2. Thus, integrating equation 3.15 over such a box, the left hand side of equation 3.7 results in

$$V\left(\mu_i\nu_i \frac{I_e^i - I_w^i}{\Delta x} + \mu_i^* \frac{I_n^i - I_s^i}{\Delta y} + \mu_i \nu_i^* \frac{I_t^i - I_b^i}{\Delta z}\right). \tag{3.16}$$

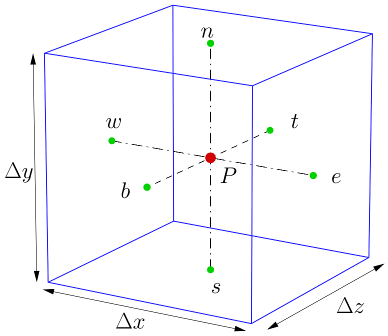

Figure 3.2: Control volume in cartesian coordinates. The RTE is solved only on the nodes (red dot), although the value of the intensity at the faces (green dots) is needed as an intermediate step in the resolution of the RTE.

The derivative of the intensity is approximated in the simplest fashion possible. The intensity at the faces (e, w, n, s, t, and b) of the control volume is not calculated, and will be related to the intensity at the node P. A linear interpolation is used, and the relation between the intensity at the nodes and faces is

$$I_P^i = f I_e^i + (1-f) I_w^i, \tag{3.17}$$

and the same is true for the remaining pairs of faces of the control volume (I_n and I_s, and I_t and I_b). The factor f selects the numerical scheme; the common choice is $f = 1$ for an upwind (or step) scheme. Other values than $f = 1$ may result in negative, unphysical intensities. Now, the intensity at node P may be isolated, by manipulating equations 3.14 and 3.16, and written as a function of the intensity at faces e, s, and b:

$$I_P^i = \frac{\mu_i \nu_i \Delta y \Delta z I_w^i + \mu_i^* \Delta x \Delta z I_s^i + \mu_i \nu_i^* \Delta x \Delta y I_b^i + f V S^i}{\mu_i \nu_i \Delta y \Delta z + \mu_i^* \Delta x \Delta z + \mu_i \nu_i^* \Delta x \Delta y + f V B^i}. \tag{3.18}$$

The above equation is valid for directions with positive projections along the three axis. For directions with negative x axis projection, that is, photons propagating from east to west, I_w is to be substituted by I_e. A similar substitution is done for directions with negative y axis projection, i. e., I_s substituted by I_n, and for directions with negative z axis projection, by substituting I_b by I_t. We must know the value of the intensity at the faces of the control, in order to calculate the intensity at the node P. This kind of discretization implies that the solution of the RTE will be explicit; for a non scattering medium surrounded by black walls, the solution will not require an iterative procedure, since the equations 3.7 will be uncoupled.

Solution procedure. Now let's examine in detail the explicit solution procedure for a two dimensional cavity. For one and three dimensional geometries the procedure is analogous.

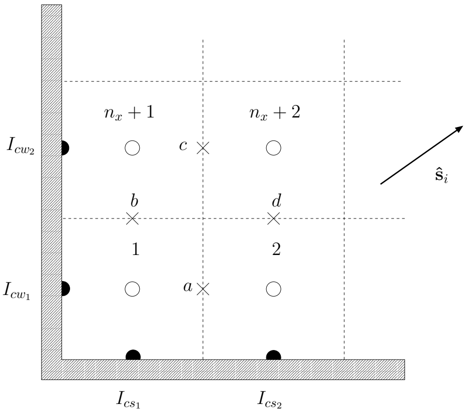

Figure 3.3: Scheme for the explicit resolution of the RTE. Boundary nodes are marked with solid semi-circles, nodes with hollow circles and faces with crosses.

The following procedure is valid for a direction defined in the octant with positive projections over the three axis. When solving any of the ordinates of this octant, the first node we will solve is the labeled with an "1" in figure 3.3. The intensity is calculated using the intensities at the faces $I^i_{cw_1}$ and $I^i_{cs_1}$, that are known from the boundary conditions. It is worth noting that, for instance, $I^i_{cw_1}$ is a boundary condition only for the ordinates with positive projection over the x axis. In order to find I^i_1, equation 3.18 is used; for a two dimensional case, consider $\Delta z = 1$ and $\Delta x \Delta y = 0$. Given the intensity at node 1, the intensity at the face labelled a in figure 3.3 is calculated using equation 3.17.

For the second node, labelled "2", the same procedure is applied, now using the recently calculated intensity at face a and the intensity imposed by the boundary condition $I^i_{cs_2}$. With the value at a and the recently calculated intensity at node "2", the intensity at the east face of node 2 is computed using equation 3.17. The procedure is repeated until the node "n_x". The intensity at the east face of node "n_x" (not shown) is also calculated, for the intensity at this particular face is not a boundary condition for ordinates with positive projection over the x axis.

The solution procedure continues calculating the intensity at the node "$n_x + 1$", using the values $I^i_{cw_2}$ and the intensity at the face labelled b, which is available from the intensity at node "1" and the boundary condition $I^i_{cs_1}$. Once $I^i_{n_x+1}$ is known, the intensity at face c is calculated, and the procedure follows for the node "$n_x + 2$". The second row is completed, and then the remaining lines are calculated, until the whole domain is solved. For a three dimensional case, the procedure is the same up to this point. Once a plane is solved, the intensities at the faces that are needed in equation 3.18 are obtained from the previous ones and the recently calculated nodes. The first plane is determined by the boundary conditions.

The procedure is the same for the remaining directions, with negative projections over the x axis, the y axis, or both. For instance, for a negative x projection and positive y projection of $\hat{\mathbf{s}}_i$, the solution procedure starts from node "n_x", taking into account that now the boundary conditions are I^i_{cs} and I^i_{ce}, that are not shown in figure 3.3.

3.3.2 Discretization in cylindrical coordinates

In cylindrical coordinates, as well as in every non cartesian coordinate system, the left hand side of the RTE will present a more complicated form than in cartesian coordinates. In particular, derivatives of I respect to $\hat{\mathbf{s}}$ will appear. This is because of the requirement for the direction $\hat{\mathbf{s}}$ to be constant when calculating the spatial derivative (that is, we are assuming that photons propagate in straight paths). If the coordinate system changes point to point, extra derivatives with respect to the angles that define $\hat{\mathbf{s}}$ will appear to balance the change of $\hat{\mathbf{s}}$ due to the coordinate system.

Thus, the cylindrical coordinates form of the RTE will add extra difficulties, because of the extra derivatives of I, and because the DOM relies on discretizing the directions for whith the RTE is solved. The left hand side of equation 3.1, then, can be approximated by the difference $I(\mathbf{r}') - I(\mathbf{r})$, see figure 3.4. It is also clear that

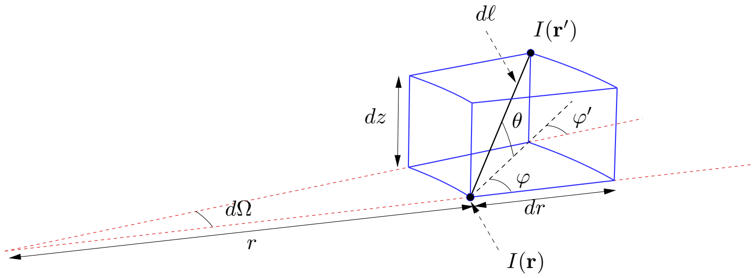

Figure 3.4: Derivation of the RTE in cylindrical coordinates. φ' lies in the same plane of φ and $d\Omega$

$r' = r + dr$, $\varphi' = \varphi - d\Omega$, $z' = z + dz$ and $\theta' = \theta$, since the vector that defines the z axis is constant. Expanding the difference between the intensity radiation field at points $\mathbf{r}'$ and $\mathbf{r}$ the left hand side can be approximated as

$$dI(\hat{\mathbf{s}}) = \frac{\partial I(\hat{\mathbf{s}})}{\partial r} dr + \frac{\partial I(\hat{\mathbf{s}})}{\partial z} dz - \frac{\partial I(\hat{\mathbf{s}})}{\partial \varphi} d\Omega. \tag{3.19}$$

No derivative with respect to the angular coordinate Θ appears, since we are considering only cylindrical geometries with axial symmetry. It is clear from figure 3.4 that $dr = d\ell\, \cos\theta \cos\varphi$ and $dz = d\ell\, \sin\theta$. The relation between $d\ell$ and $d\Omega$ is a little harder to find. Looking at the figure again, we have $(r + dr)\sin d\Omega = d\ell \cos\theta \sin\varphi$. Since dr and $d\Omega$ are infinitesimal, it is possible to state that $r\, d\Omega = d\ell \cos\theta \sin\varphi$. So the radiative transfer equation in cylindrical coordinates is

$$\mu \frac{\partial I(\hat{\mathbf{s}})}{\partial r} + \xi \frac{\partial I(\hat{\mathbf{s}})}{\partial z} - \frac{\eta}{r} \frac{\partial I(\hat{\mathbf{s}})}{\partial \varphi} = -(\kappa + \sigma_s) I(\hat{\mathbf{s}}) + \kappa I_B + \frac{\sigma_s}{4\pi} \int_{4\pi} I(\hat{\mathbf{s}}') \Phi(\hat{\mathbf{s}}'; \hat{\mathbf{s}})\, d\Omega' \tag{3.20}$$

where $\mu = \cos\theta \cos\varphi$, $\xi = \sin\theta$ and $\eta = \cos\theta \sin\varphi$. Droping the $\hat{\mathbf{s}}$ dependence for clarity, it can be written in a more convenient form:

$$\frac{\mu}{r} \frac{\partial (rI)}{\partial r} + \xi \frac{\partial I}{\partial z} - \frac{1}{r} \frac{\partial (\eta I)}{\partial \varphi} = -(\kappa + \sigma_s) I + \kappa I_B + \frac{\sigma_s}{4\pi} \int_{4\pi} I \Phi(\hat{\mathbf{s}}'; \hat{\mathbf{s}})\, d\Omega' \tag{3.21}$$

The main difficulty is the appearance of the derivative with respect the direction $\hat{\mathbf{s}}$ in the left hand side of the RTE. In order to approximate such derivative, the more ordinates the better, but in most ordinate sets, and particularly the S_n, the ordinates aren't even close to each other, making the usual evaluation of a numerical derivative uncertain. Thus, the approximation of the angular derivative has to be accurately chosen. The angular derivative used in this work is the one proposed by Truelove [11], which is

$$\frac{\partial(\eta I)}{\partial\varphi} \simeq \frac{\gamma_{i+}I^{i+} - \gamma_{i-}I^{i-}}{\omega_i}, \tag{3.22}$$

where the γ coefficients are determined by a recurrence relation. If the intensity radiation field is assumed to be constant, then $\gamma_{i+} = \gamma_{i-} + \omega_i \partial\eta/\partial\varphi$. The intensities at ordinates $i+$ and $i-$ are related to the discrete intensity I^i by the linear relation $I^i = fI^{i+} + (1-f)I^{i-}$. The factor f is the same as in equation 3.17. The initial values for γ_{i-} and I^{i-} depend on the polar angle, and are $\gamma_{i-} = 0$ and the solution of the simplified equation (in this equation $\varphi = 0$)

$$\mu\frac{\partial I^{i-}}{\partial r} + \xi\frac{\partial I^{i-}}{\partial z} = -B^{i-}I^{i-} + S^{i-} \tag{3.23}$$

with the same definition of the source terms as in equation 3.5. Finally, the set of diferential equations to solve is

$$\frac{\mu_i}{r}\frac{\partial(rI^i)}{\partial r} + \xi_i\frac{\partial I^i}{\partial z} - \frac{1}{r}\left(\frac{\gamma_{i+}I^{i+} - \gamma_{i-}I^{i-}}{\omega_i}\right) = -B^iI^i + S^i, \tag{3.24}$$

For this equation, the finite volume technique is also employed, so, the next step is to multiply both sides by $2\pi r\,dr\,dz$, which is the element of volume in the case of axial simetry, and integrate over the volume. When the integral is performed, the resulting equations use the unknown values of the intensity at the faces of the control volume. By using a linear relation like equation 3.17 to relate the value of the intensity at the faces and in the center of the control volume, I^i_e and I^i_n can be eliminated and the explicit value for I^i_P is obtained:

$$I^i_P = \frac{\mathcal{N}_r I^i_w - \mathcal{N}_P I^{i-}_P + \mathcal{N}_z I^i_z + fVS^i}{\mathcal{D}_r - \mathcal{D}_P + \mathcal{D}_z + fVB^i}. \tag{3.25}$$

The coeficients are

$$\mathcal{N}_r = 2\pi\mu^i\Delta z(r_w(1-f) + r_e f) \qquad \mathcal{D}_r = 2\pi\mu^i\Delta z r_w \tag{3.26}$$

$$\mathcal{N}_P = \frac{2\pi\Delta_z(r_e - r_w)(\gamma_{i+}(1-f) + \gamma_{i-}f)}{\omega_i} \qquad \mathcal{D}_P = \frac{2\pi\Delta_z(r_e - r_w)\gamma_{i+}}{\omega_i} \tag{3.27}$$

$$\mathcal{N}_z = \mathcal{D}_z = \pi\xi_i(r_e^2 - r_w^2) \qquad V = \pi(r_e^2 - r_w^2)\Delta z \tag{3.28}$$

The above coeficients are valid when integrating the equation inwards (from higher to lower radius). When integrating the equation outwards, from lower to higher radius, r_e has to be changed to r_w and viceversa in $\mathcal{N}_r$ and $\mathcal{D}_r$ only. As stated before the γ coeficients are obtained by a recursion formula:

$$\gamma_{i+} = \gamma_{i-} \pm \mu_i \omega_i \tag{3.29}$$

where the plus sign is used for outwards integration and the minus sign is used for inwards integration. The reason for that sign change is that the ordinates are only defined on the first octant and therefore μ_i, η_i and ξ_i are all positive.

Solution procedure. The N discrete ordinates $\hat{\mathbf{s}}_i$ are classified in m groups. Each group has l_m ordinates, and all of the ordinates belonging to the same group have equal polar angle θ. Thus there are only m different polar angles covered by the discrete ordinates set. For each of these m groups, the ordinates are ordered from higher to lower μ. The domain is discretized in $N_r \times N_z$ control volumes.

The solution procedure for each group is as follows: set $\gamma_{i-} = 0$, and for each ordinate l, $l = 1 \mapsto l_m$, equation 3.25 is repeatedly solved in the direction of decreasing radius. The values of I_r and I_z for the first node are determined by the boundary conditions, while the value of I_P^{i-} is obtained by solving equation 3.23. The linear relation $I_P^i = fI_e^i + (1-f)I_w^i$ is used once I_P is known, in order to calculate I_e^i for the radial node k, which is equal to I_w^i for the radial node $k-1$. Once each ordinate has been calculated, equation 3.25 is integrated outwards, for each ordinate l, this time $l = l_m \mapsto 1$. The boundary condition at the symmetry axis is that the intensity outwards should be equal to the intensity inwards. The linear relation $I_P^i = fI_e^i + (1-f)I_w^i$ is again used to calculate I_e^i for radial node k, which is equal to I_w^i for the radial node $k+1$. This procedure is repeated for each z.

Notice that the order in which each of the m groups is solved is irrelevant in this case. This is because no derivatives respect to the polar direction θ appear in the radiative transfer equation.

3.3.3 Boundary conditions

The discretization of the wall boundary conditions, where $\hat{\mathbf{n}}$ is the vector perpendicular to the wall (equation 3.2) is readily obtained by replacing the integral term by a weighted summation,

$$\int_{\hat{\mathbf{n}}\cdot\hat{\mathbf{s}}<0} \rho_d(\hat{\mathbf{s}}) I(\hat{\mathbf{s}}) |\hat{\mathbf{n}}\cdot\hat{\mathbf{s}}|\, d\Omega \simeq \sum_{\hat{\mathbf{n}}\cdot\hat{\mathbf{s}}_j<0} \omega_j \rho_d(\hat{\mathbf{s}}_j) I^j |\hat{\mathbf{n}}\cdot\hat{\mathbf{s}}_j|, \tag{3.30}$$

where I^j is a shortcut for $I(\hat{\mathbf{s}}_j)$. The angular discretized form of such boundary condition is therefore

$$I^j_{\text{wall}} = \varepsilon I_b + \rho_s^j I^{j*} + \sum_{\hat{\mathbf{n}}\cdot\hat{\mathbf{s}}_j<0} \omega_j \rho_d(\hat{\mathbf{s}}_j) I^j |\hat{\mathbf{n}}\cdot\hat{\mathbf{s}}_j|. \tag{3.31}$$

Again I^{j*} is the intensity in a direction $\hat{\mathbf{s}}_j^*$ which is the reflection of $\hat{\mathbf{s}}_j$ with a plane perpendicular to $\hat{\mathbf{n}}$. It is clear from the above equation that, for black boundaries (i. e., $\varepsilon = 1$, and $\rho_d = \rho_s = 0$), there is no coupling among the different discretized directions due to the boundaries. Thus, if the medium is also non scattering, the solution procedures described above solve the RTE in just one step.

The wall boundary conditions, however, are not appropriate for solar applications. For instance, in the work [12], a solar collector is studied, and boundary conditions capable of handle incoming intensity at a very particular angle are required. The following holds only for ordinates that lie exactly on a plane, such as these defined by equations 3.11 and 3.12.

The incidence angle of incoming radiation may be any between 0 and $\pi/2$, while the ordinates that we are solving belong to a discrete set. This means that, in general, the incident direction, $\hat{\mathbf{s}}$, will not coincide with any of the discrete ordinates. The idea is to split the incoming intensity into two consecutive discrete ordinates, with appropriate weights. If the incident angle is Θ_{ext}, the angle within the medium will change according to Snell law:

$$n_{\text{ext}}\Theta_{in} = n_{\text{int}}\Psi, \tag{3.32}$$

where Ψ is the angle to be incorporated to the boundary conditions, and n stands for the refraction index. The incoming intensity, I_0, will be reduced also by a factor τ_s, the transmissivity of the surface. The incoming intensity direction is written in terms of $\hat{\mathbf{s}}_1$ and $\hat{\mathbf{s}}_2$, two consecutive discrete ordinates (see figure 3.5). Therefore, we seek two values, m and n, such that

$$\hat{\mathbf{s}} = m\hat{\mathbf{s}}_1 + n\hat{\mathbf{s}}_2. \tag{3.33}$$

We multiply equation 3.33 by $\hat{\mathbf{s}}_1$ and $\hat{\mathbf{s}}_2$, and solve for m and n:

$$\begin{aligned} m &= \frac{a - cb}{1 - c^2} \\ n &= \frac{b - ca}{1 - c^2}, \end{aligned}$$

where $a = \hat{\mathbf{s}}_1 \cdot \hat{\mathbf{s}}$, $b = \hat{\mathbf{s}}_2 \cdot \hat{\mathbf{s}}$, and $c = \hat{\mathbf{s}}_1 \cdot \hat{\mathbf{s}}_2$, all these quantities are known.

This is the decomposition of the $\hat{\mathbf{s}}$ vector into two consecutive ordinate sets. Finally, the values m and n are multiplied by $I_0\tau_s$, and divided by the corresponding weights ω_1 and ω_2, respectively. Therefore we have, for this particular boundary condition, the intensity equal to zero except for the two ordinates $\hat{\mathbf{s}}_1$ and $\hat{\mathbf{s}}_2$. The energy flux through a surface perpendicular to the x axis is, in this approximation,

$$q_r \simeq \sum_j I^j \omega_j (\hat{\mathbf{i}} \cdot \hat{\mathbf{s}}_j) = I_0 \tau_s (m \cos\theta_1 + n \cos\theta_2). \tag{3.34}$$

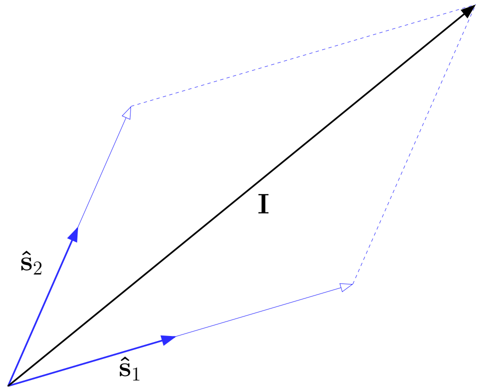

Figure 3.5: Incoming intensity as a sum of two discrete ordinates

It is possible to show that, as the number of directions increases, both m and n tend to $1/2$, and since in this limit, $\theta_1 \simeq \theta_2 \simeq \Psi$, we obtain the expected result for the radiative heat flux, namely

$$q_r \simeq I_0 \tau_s \cos \Psi. \tag{3.35}$$

3.4 Numerical issues

3.4.1 Error sources

There are two types of numerical errors when solving the RTE with the discrete ordinates method. First, there is the ray effect. This effect manifests itself as oscillations in the profile along any direction of integrated quantities, such as heat flux (equation 3.8) and divergence of heat flux (equation 3.9). These undulations appear because the RTE is solved only for a few directions. The only way to minimize this effect is to consider sets with more ordinates. Last, but not least, there is the false scattering effect. This effect is due to the finite size of the control volumes, and to the fact that the mesh is not (in general) aligned with the ordinates that we are solving. Therefore, solutions that should present a sharp step, exhibit a perceptible slope instead. This is the same effect described by Patankar [13] as false diffusion. The means to overcome this effect is to increase the number of control volumes of the mesh.

It is interesting to note that both effects are linked. For instance, if we try to minimize the false scattering by increasing the mesh size, then the ray effect will become more obvious, provided that the ordinate set remains the same. Thus, in order to have correct numerical simulations, an increase of the mesh size should be accompanied of an increase of the number of ordinates, to avoid the ray effect. In section B.2 there is an explaination of this linkage.

It is worth noting that the ray effect is reduced when the optical thickness is increased. The reason is that, as the optical thickness increases, radiation becomes more and more a local phenomenon, its directional behavior tending to disappear. The mean free path of the photons is then reduced, meaning that the photon which impacts to a surface bears little or no information on from which surface was emitted. The impact of false scattering is also diminished if the albedo is large.

3.4.2 Radiative equilibrium

For situations where radiation is the dominant mode of heat transfer, the energy equation takes the form of equation 1.14. Thus, taking into account equation 1.20, the temperature at each point may be evaluated. However, once the temperature field is updated, the intensity radiation field should be recalculated, resulting on a new, different temperature inferred using equation 1.20. Therefore, an iterative procedure is required.

It is also possible to include other modes of energy transfer in the source term $\mathcal{S}$ in equation 1.14. For example, conduction heat transfer could be included by setting the source function to $\boldsymbol{\nabla} \cdot (k \boldsymbol{\nabla} T)$, being k the thermal conductivity. In practice, however, combined problems are solved the other way around: the radiative heat flux divergence is included as a varying source term in the energy equation, and the temperature is not calculated using equation 1.20.

3.4.3 Two media interface modelling

When two or more different materials are considered, the intensity in the interface of these two materials cannot be calculated using equation 3.17. Instead, a more detailed balance is performed. In figure 3.6 the relevant quantities are indicated. The intensity is known on the nodes (red dots), and its represented by an arrow pointing in the direction of $\hat{\mathbf{s}}_i$. The different length of the arrows accounts for the different value of I^i at each node. The swinging line represents the black body intensity I_b at the temperature of the node "1", which is isotropical. There is also a contribution due to the diffuse reflectivity, which takes into account the intensity in all directions in the same quadrant of I^i_* (not shown for the sake of clarity). Our aim is to compute the value at the interface (green dot), I^i_c.

There are different contributions to I^i_c; a term due to the black body emission, which takes into account the temperature of node "1", a transmitted term through the node "1", and a reflection term that takes into account the incoming intensity from node "2". The surface is assumed to be described by the specular reflectivity ρ_s, and the diffuse reflectivity ρ_d. More precisely, the intensity between the two nodes

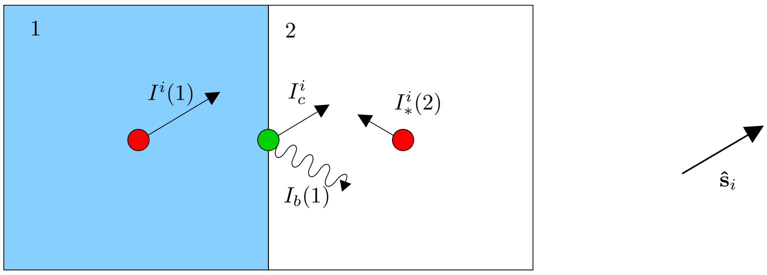

Figure 3.6: Calculation of the intensity I^i_c at the face between two control volumes of different material, and for direction $\hat{\mathbf{s}}_i$. $I^i_*(2)$ represents the intensity in a direction which is the reflected counterpart of $\hat{\mathbf{s}}_i$ with respect to the normal to the interface.

is calculated using the relation

$$I^i_c = \varepsilon^i I_b(1) + \tau^i I^i(1) + \rho^i_s I^i_*(2) + \frac{1}{\pi} \sum_{\hat{\mathbf{n}}\cdot\hat{\mathbf{s}}_j<0} \omega_j \rho^j_d I^j(2) |\hat{\mathbf{n}} \cdot \hat{\mathbf{s}}_j|, \tag{3.36}$$

where the parentheses indicates in which node the intensity is evaluated. The term $I^i_*(2)$ represents the intensity in a direction which is the reflected counterpart of $\hat{\mathbf{s}}_i$ with respect to the normal to the interface. The superindex i means magnitudes evaluated in the direction i.

The following simplifications are used: if the node “1” is opaque, then we assume that $\tau^i = 0$ and $\varepsilon^i = 1 - \rho^i_d - \rho^i_s$. On the other hand, if node “1” is not opaque, then $\varepsilon^i = 0$ and $\tau^i = 1 - \rho^i_d - \rho^i_s$. Finally, if the node “2” is opaque, the intensity I^i_c is set to zero.

3.5 Sample calculations

A wide variety of cases have been solved by using the DOM, with the goal of testing the reliability of the implemented code. Whenever possible, results obtained with other methods are also presented, including comparisons to analytical solutions. The work presented in the 5th ECCOMAS conference [14], held in Barcelona, includes the solution of cases with and without intermediate obstacles, both transparent and participating media, problems considering the radiative equilibrium assumption, simple cavities with cylindrical symmetry…Some illustrative results, not included in any published work, are presented as well.

3.5.1 Analytical solution in purely absorbing media

In order to test the capabilities of the DOM in participating media we first focus our attention to a case which has an analytical solution: a square enclosure with length $1m$, containing a purely absorpting medium with $T = 0K$, surrounded by black walls at temperature T, such that $\sigma_B T^4 = 1 \; Wm^{-2}$. The analytical solution for this particular case is explained in section A.2.

Numerical results are presented for several absorptions, in a 128×128 control volumes mesh, with $f = 0.6$ (see equation 3.17). The ordinate set is obtained from equations 3.11 and 3.12, for $N = 3$. Since we are comparing the intensity radiation field, and we are not interested in integral quantities, the number of directions is completely irrelevant, because the medium is non scattering and the walls are black. Therefore, the results presented for this problem are not affected by the ray effect.

Intensity radiation field along the direction given by $\theta = \pi/12$ is shown in the plots of figures 3.7 and 3.8. The intensity is evaluated along the straight line $y = 1 - x$. The agreement between analytical and numerical solution is really good, except in te vicinity of $x = 0.8$. This is the manifestation of the false scattering, since it is not possible, numerically, to reproduce the step present in the analytical solution. The false scattering effect is apparent, because the mesh is not properly aligned with the directions that we are solving. To reduce this false scattering, and to obtain a numerical solution even closer to the analytical one, higher order schemes should be employed.

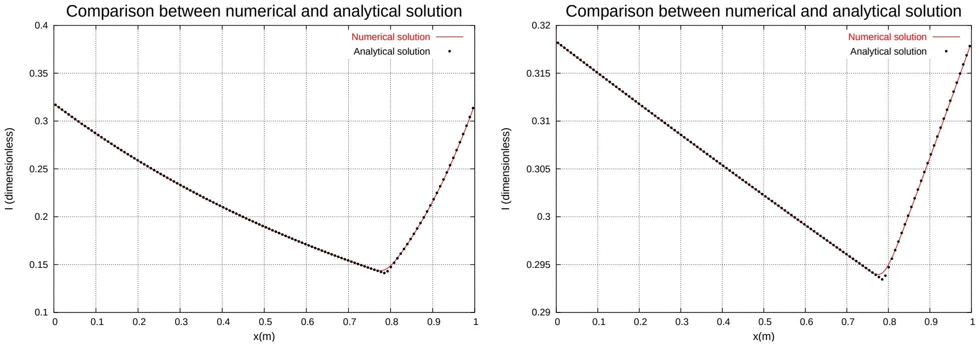

Figure 3.7: Comparison between numerical and analytical solutions of the RTE. Left: absorption coefficient $\kappa = 1m^{-1}$. Right: Absorption coefficient $\kappa = 0.1m^{-1}$.

3.5.2 Geometry with internal obstacles

This case attempts to simulate a printed board, with two heated elements exchanging energy by radiation with its cooler environment. The case has been solved

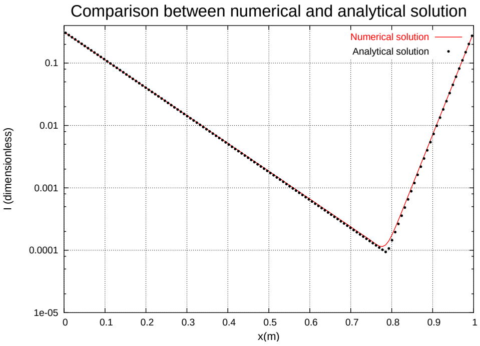

Figure 3.8: Comparison between numerical and analytical solutions of the RTE, absorption coefficient $\kappa = 10m^{-1}$.

to demonstrate the ability of the DOM to handle complicated cartesian geometries and also to compare the results obtained with the DOM and the RIM. Consider a two dimensional cavity, with $L_x = 12mm$ and $L_y = 50mm$. The board is maintained at $T_{\text{board}} = 310K$, and is characterized by an emissivity of $\varepsilon_{\text{board}} = 0.9$. The remaining surrounding walls are kept at $T = 300K$, and have emissivities of $\varepsilon = 0.5$. The protrusions, pretending to be chips, are hotter at $T_{\text{chip}} = 320K$ and have an emissivity of $\varepsilon_{\text{chip}} = 0.8$. Their dimensions are $6mm$ wide and $15mm$ high. The whole set is symmetrical with respect the line $y = 25mm$. The whole scheme is depicted in figure 3.9 (left).

The results obtained with the DOM, with the directions given by equations 3.11 and 3.12, and $N = 20$, are compared to the results obtained with the RIM, with a coarse mesh of 12×50 control volumes.

Figure 3.10 shows the heat flux following the profile of the printed board. The variable k is used to describe the path along which the heat flux is calculated. We start in the middle of the west wall, with $k = 0$, and continue clockwise running along all the surfaces (including the upper protrusion), until we reach the middle of the east wall ($k = 1$), as illustrated in figure 3.9 (right). The precise value of k is obtained by dividing the number of surface by the total number of surfaces in this path, which, for a 32×80 control volume mesh, is 144.

The heat flux shows big jumps, corresponding to the transition between zones at diferent temperatures (from west wall to the protrusion, to the west wall again, to the north wall…). The oscillations apparent in the RIM result are due to the fact that in this geometry there are blocking surfaces, an important source of error when calculating the view factors.

There is an overall good agreement between both methods, except for two clearly

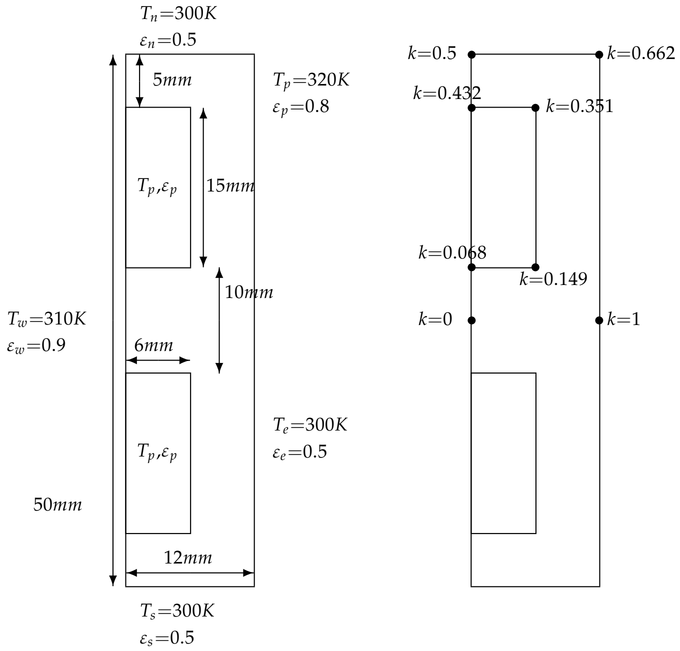

Figure 3.9: Geometry of the printed board, and definition of the variable k.

defined ranges of k, which correspond to the west wall. The results obtained with the DOM are closer to those reported by Sànchez and Smith [7] in these zones.

3.5.3 Purely scattering medium

Next, a two dimensional, square cavity, with length $1m$, containing a purely scattering medium is considered, with $\sigma_s = 1m^{-1}$ and $T = 0K$. The same case was solved by Fiveland [15]. The east, north and south walls are black and maintained at $0K$, while the west wall, also black, has a fixed temperature T_w. The non dimensional total incident energy G^* is calculated, where

$$G^* = \int_{4\pi} I d\Omega / \sigma_B T_w^4. \tag{3.37}$$

In figure 3.11, G^* is plotted versus the x coordinate. Solution is obtained on a 61×61 mesh, with the T_5 and the S_4 sets for the angular quadrature, and $f = 1$ (see equation 3.17). There is a good agreement between numerical results presented in [16] and the DOM, for the T_5 quadrature, with a total of 100 ordinates, while the S_4 ordinate set, with 12 ordinates, shows the forementioned ray effect, as an oscilation

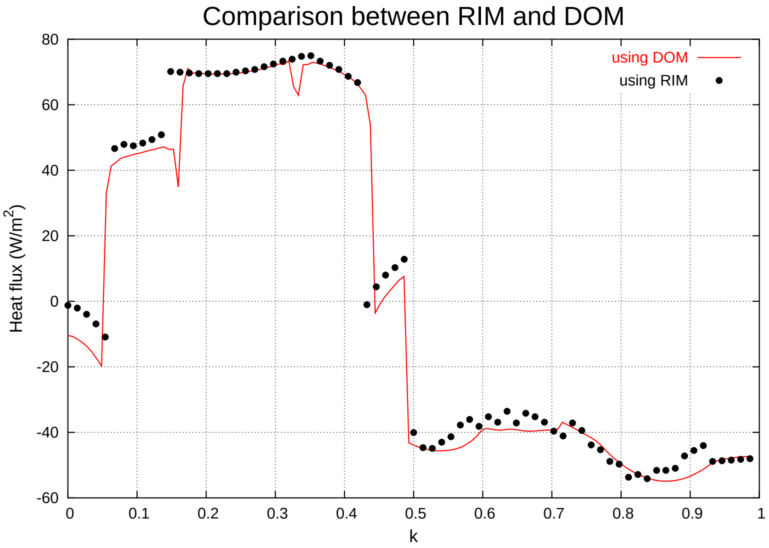

Figure 3.10: Comparison between RIM and DOM methods, for a simplified model of a printed board.

around the direction independant result using T_5, with 100 ordinates. The quadrature set to be used is implicitly determined by the mesh size: the finer the mesh, more ordinates must have the ordinate set chosen to integrate the RTE.

3.5.4 Inhomogeneous three dimensional cavity

The software tools developped allow the resolution of the RTE with locally varying optical properties, i. e., the absorption and scattering coefficients may be a function of the position. This ability will be very useful, and will have an inmediate application to comubstion problems, since the absorption coefficient will depend both on the temperature and species concentration, fields which vary considerably on the domain.

Hsu and Farmer [17] solved a three dimensional domain, with inhomogeneous optical properties, using the YIX and Monte Carlo methods, and with an anisotropic phase function. The radiative transfer equation is solved using the DOM, with six directions per octant, namely the S_6 ordinate set. An inhomogeneous optical thickness $\tau = L(\kappa + \sigma_s)$ is used, specifically of the form

$$\tau(x, y, z) = a\left(1 - 2\left|x - \frac{1}{2}\right|\right)\left(1 - 2\left|y - \frac{1}{2}\right|\right)\left(1 - 2\left|z - \frac{1}{2}\right|\right) + b, \tag{3.38}$$

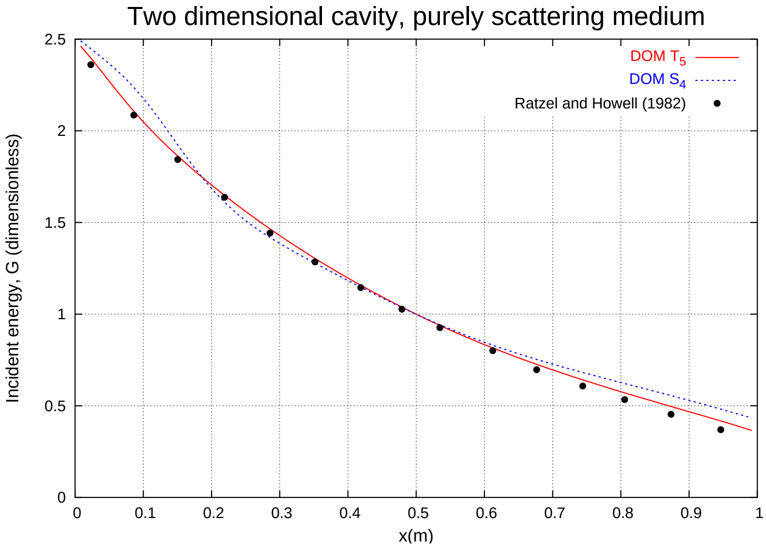

Figure 3.11: Two dimensional cavity containing cold, purely scattering media. The west wall has an emission power of 1 W/m^2. The total incident energy G^* is plotted for $y = 0.5$. Results obtained with the DOM are calculated with the T_5 and S_4 (which shows ray effect) ordinate sets, and 61×61 mesh.

for several values of a and b. The phase function is assumed to be of the form $\phi(\hat{\mathbf{s}}'; \hat{\mathbf{s}}) = 1 + \gamma(\hat{\mathbf{s}}' \cdot \hat{\mathbf{s}})$. This phase function is known as linear anisotropic scattering phase function. The phase function is said to be forward scattering if $\gamma = 1$, backward scattering if $\gamma = -1$ and isotropically scattering if $\gamma = 0$. Different values of γ are used. Various problems are solved, all of them concerning a cubical cavity with length $L = 1m$. The albedo, $\omega = \sigma_s/(\kappa + \sigma_s)$, a measure of the importance of the absorption versus the scattering, is set to $\omega = 0.9$. Thus, the effect of the anisotropic scattering will be more apparent.

For the first case presented, the coefficients for the optical thickness are $a = 0.9$ and $b = 0.1$. The boundary conditions are five cold walls ($T = 0\,K$) and one with an emissive power of unity, at $x = 0$. The medium is assumed to be at radiative equilibrium. The mesh used was an uniform, 64^3 control volume mesh. This problem is solved for a forward scattering phase function ($\gamma = 1$) and for a backward scattering phase function ($\gamma = -1$). The total heat flux through the hot surface is shown in figure 3.12. The total heat flux is lower in the backward scattering case, since the photons, that are only emitted from the hot wall, are most probably scattered back; these back scattered photons count as a negative contribution to the total heat flux.

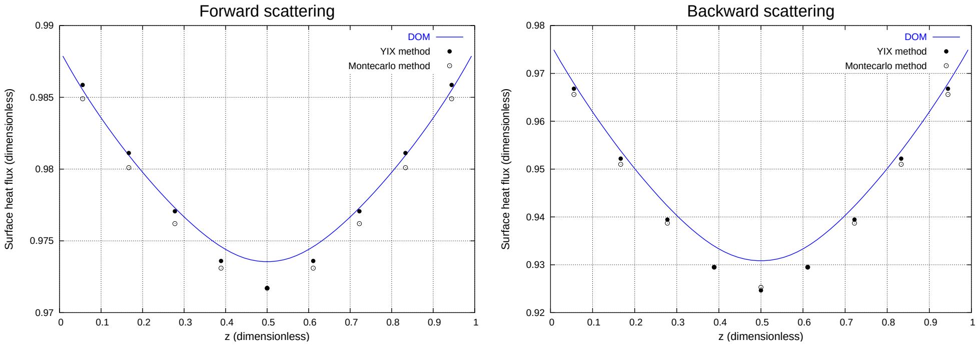

Figure 3.12: Dimensionless heat flux at hot surface, $x = 0$ and $y = 1/2$. Left: forward scattering, $\gamma = 1$. Right: Backward scattering, $\gamma = -1$.

The emissive power given by the DOM for this low optical thickness differs from the YIX and Monte Carlo result. Taking into account that the same problem solved with the DOM and a uniform 12^3 control volume mesh gives a result which is closer to that of the YIX and Monte Carlo methods, the difference observed may be due mainly to the fact that different meshes were used (the YIX and Monte Carlo used a 9^3 control volume mesh). The heat flux through the hot surface predicted by the DOM is slightly larger than the obtained with the Monte Carlo and YIX methods. However the maximum difference, which is for backward scattering, is less than 1%.

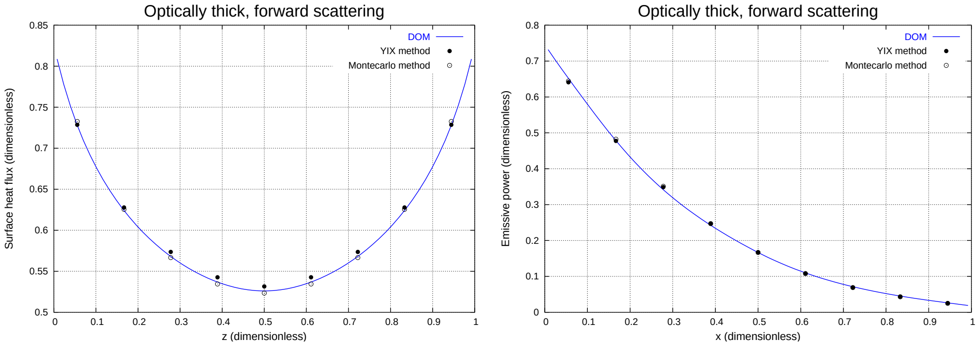

Figure 3.13: Optically thick case, forward scattering ($\gamma = 1$). Left: Dimensionless heat flux at hot surface, $x = 0$ and $y = 1/2$. Right: Dimensionless emissive power at $y = z = 1/2$.

The next problem considered is a forward scattering case ($\gamma = 1$), this time the optical thickness is computed with $a = b = 5$. The boundary conditions and medium temperature are the same of the anisotropic scattering case, and the medium is also at radiative equillibrium. The emissive power and the surface heat flux for this case are shown in figure 3.13. The dimensionless emissive power is given by $\sigma_B T(x)^4$.

The emissive power and surface heat flux given by the DOM agree very well with those of the YIX and Monte Carlo methods. The discrepancy between the DOM and the other methods is lower in this case, partly because the ray effect impact is reduced due to the higher optical thickness, as explained in section 3.4.1.

3.5.5 Results in cylindrical coordinates

In order to validate the cylindrical symmetry implementation of the DOM, two different cases, one with fixed temperature field and the other at radiative equilibrium, have been solved. The first of them, known as Delft furnace, is described by Truelove [11]. For such case, experimental results are available. The furnace is a $5m$ tall cylinder, with a radius of $0.45m$. The walls are kept at $425K$, with an emissivity $\varepsilon = 0.8$. The burner is located at the bottom of the furnace. There is a hole with a radius of $15cm$, starting at the symmetry axis, which is assumed to be at room temperature, $300K$. The absorption coefficient is homogeneous, $\kappa = 0.3m^{-1}$. The fixed temperature field comes from experimental measures.

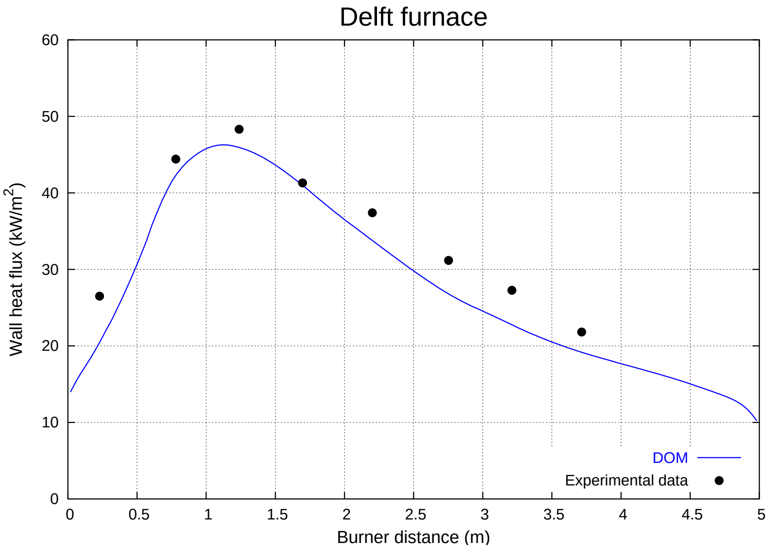

Figure 3.14: Long wall heat flux for the Delft furnace. The DOM solution was obtained with the S_8 quadrature set and a 24×136 control volume mesh.

In figure 3.14 the wall heat flux along the side, tall wall, calculated by the DOM, is shown and compared to experimental data. Although a disagreement of about a 10% is observed far off the burner, the numerical results are good enough. The main source of the difference may reside on the assumption of homogeneous absorption coefficient, scattering neglection, and the experimental inferred temperature field.

The second case follows the work by Baek and Kim [18], where a modified version of the DOM is presented. A cylindrical furnace is solved, $4m$ long and with a diamter of $2m$. The long, side wall is kept at $900K$, and the caps of the cylinder have temperatures of $400K$ and $1200K$. The emissivity of the walls is $\varepsilon = 0.7$ except for the hot wall, with emissivity $\varepsilon = 0.85$. Two homogeneous extinction coefficient, $\beta = \kappa + \sigma_s$, are considered: $\beta = 0.1m^{-1}$ and $\beta = 5m^{-1}$. The albedo $\omega = \sigma_s/\beta$ is set to 0.7. The scattering is isotropical, i. e., $\phi(\hat{\mathbf{s}}'; \hat{\mathbf{s}}) = 1$. Radiative equilibrium hypothesis is assumed, therefore the temperature field will be calculated. The mesh used had 24×32 control volumes, and the ordinate set used was the T_4 set. For the optically thick case, the temperature field is shown in figure 3.15. The heat flux through the long wall is presented in figure 3.16, where the DOM and the Finite Volume Method

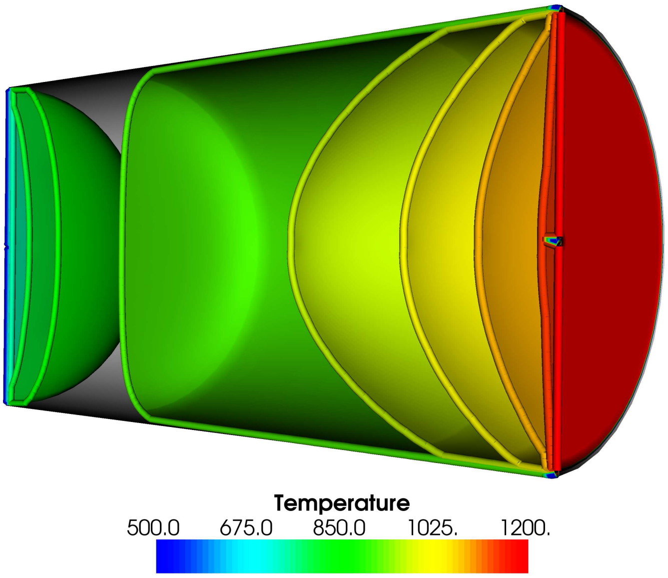

Figure 3.15: Isothermal surfaces in the furnace for the optically thick case.

(FVM) are compared. The FVM [19] can also be applied to the angular integration of the RTE, instead of using the Gaussian quadrature approach of the DOM. The agreement between the two methods are quite good, particularly for the optically thick case.

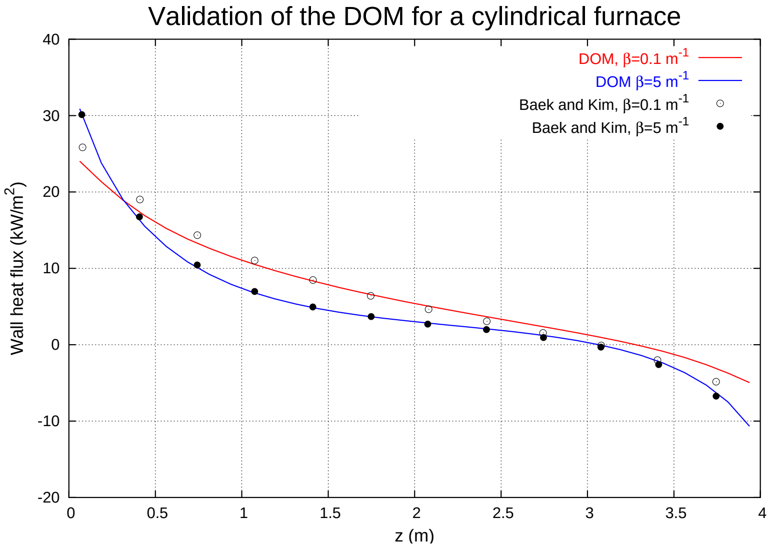

Figure 3.16: Heat flux through side wall. Results from [18] are calculated with the finite volume method for the angular integration.

3.6 Conclusions

In this chapter, the Discrete Ordinates Method has been described. The key feature of this method is the selection of the ordinate sets to be used to integrate the angular part of the radiative transfer equation. The fundamental properties that must hold for these sets have been laid out. In addition, it is detailed the discretization of the radiative transfer equation, for both cartesian and cylindrical geometries.

With the goal of validate the discretizations presented in section 3.3, several problems have been solved. The appropriateness of the finite volume method to discretize the spatial part of the RTE is seen when the numerical solution for the intensity radiation field is compared to the analytical one (section 3.5.1). The agreement between the RIM and the DOM is shown in section 3.5.2, where only surface heat exchange has been taken into account. A scattering medium, which poses a direct test to any ordinate set chosen to integrate the RTE, has been considered in section 3.5.3. In this section it is also shown the impact of the ray effect, if the mesh and the number of directions are not properly linked. Inhomogeneous, anisotropically scattering media can also be handled, as it is demonstrated in section 3.5.4. In this section, the energy equation has been used to determine the temperature, instead of using a prescribed temperature field. Finally, problems with cylindrical symmetry have been solved as well, in section 3.5.5. The performance of the DOM in this variety of situations is deemed to be completely satisfying.

References

[1] A. Yücel, S. Acharya, and M. L. Williams. Natural convection and radiation in a square enclosure. *Numerical Heat Transfer, Part A*, 15:261–278, 1989.

[2] K. H. Lee and R. Viskanta. Two-dimensional combined conduction and radiation heat transfer: comparison of the discrete ordinates method and the diffusion approximation methods. *Numerical Heat Transfer, Part A*, 39:205–225, 2001.

[3] Sandip Mazumder and Michael F. Modest. Application of the Full Spectrum Correlated-*k* Distribution Approach to Modeling Non-Gray Radiation in Combustion Gases. *Combustion and Flame*, 129(4):416–438, 2002.

[4] P. J. Coelho, O. J. Teerling, and D. Roekaerts. Spectral radiative effects and turbulence/radiation interaction in a non-luminous turbulent jet diffusion flame. *Combustion and Flame*, 133(1–2):75–91, 2003.

[5] R. Koch, W. Krebs, S. Wittig, and R. Viskanta. Discrete ordinates quadrature schemes for multidimensional radiative transfer. *J. Quant. Spectrosc. Radiat. Transfer*, 53(4):353–372, 1995.

[6] Rainier Koch and Ralf Becker. Evaluation of quadrature schemes for the discrete ordinates method. *J. Quant. Spectrosc. Radiat. Transfer*, 84(4):423–435, 2004.

[7] A. Sànchez and T. F. Smith. Surface radiation exchange for two-dimensional rectangular enclosures using the discrete ordinates method. *Journal of Heat Transfer*, 114:465–472, May 1992.

[8] T. Götz. Coupling heat conduction and radiative transfer. *J. Quant. Spectrosc. Radiat. Transfer*, 72:57–73, 2002.

[9] W. A. Fiveland. The selection of discrete ordinate quadrature sets for anisotropic scattering. *HTD-Fundamentals of Radiation Heat Transfer*, 160:89–96, 1991.

[10] C. P. Thurgood, A. Pollard, and H. A. Becker. The T_n quadrature set for the discrete ordinates method. *Journal of Heat Transfer*, 117:1068–1070, November 1995.

[11] J. S. Truelove. Evaluation of a multi-flux model for radiative heat transfer in cylindrical furnaces. HTFS Report, May 1978.

[12] G. Colomer, J. Cadafalch, and M. Costa. Numerical study of a solar collector. In *Proceedings of the Forum International Sur les Energies Renouvelables*, volume I, pages 66–71, 2002.

[13] S. V. Patankar. *Numerical Heat Transfer and Fluid Flow.* McGraw Hill, 1980.

[14] G. Colomer, M. Costa, R. Cònsul, and A. Oliva. Radiant exchange in domains with obstacles using the discrete ordinates method. In *Proceedings of the Fifth European Congress on Computational Methods in Applied Sciences and Engineering (ECCOMAS)*, pages 1–20, 2000.

[15] W. A. Fiveland. Discrete-ordinates solutions of the radiative transport equation for rectangular enclosures. *Journal of Heat Transfer*, 106:699–706, November 1984.

[16] A. C. Ratzell III and J. R. Howell. Two-dimensional radiation in absorbing-emitting-scattering media using the P_N approximation. Paper 82-HT-19, 1982.

[17] P. Hsu and J. T. Farmer. Benchmark Solutions of Radiative Heat Transfer Within Nonhomogeneous Participating Media Using the Monte Carlo and YIX Method. *Journal of Heat Transfer*, 119:185–188, February 1997.

[18] Seung Wook Baek and M. Y. Kim. Modification of the Discrete Ordinates Method in an axisymmetric cylindrical geometry. *Numerical Heat Transfer, Part B*, 31:313–326, 1997.

[19] G. D. Raithby and E. H. Chui. A finite volume method for predicting radiant heat transfer in enclosures with participating media. *Journal of Heat Transfer*, 112:415–423, 1990.

4

Radiative heat transfer in non gray media

4.1 Introduction

The radiative transfer equation is formulated in terms of two properties: the absorption coefficient κ and the scattering coefficient σ_s. In real gases both properties depend on the radiation wavenumber η (the inverse of the photon wavelength λ). While the scattering coefficient is expected to depend smoothly on η, the absorption coefficient presents thousands of absorption lines, due to the quantum nature of the absorption process. An absorption line is, therefore, represented by a wavenumber η_i, among other variables, meaning that the probability of a photon of wavenumber η_i being absorbed by one molecule presents a maximum, while photons with slightly different wavenumber are absorbed with a probability orders of magnitude lower. Absorption lines are suposed to exhibit a profile $f(\eta, \eta_i)$, meaning that photons with wavenumber very close to η_i still can be absorbed with perceptible probability. The most commonly assumed profile is the so called Lorentz profile, which is

$$f(\eta, \eta_i) = \frac{1}{\pi} \frac{\gamma_i}{\gamma_i^2 + (\eta - \eta_i)^2}, \tag{4.1}$$

where γ_i is another line parameter, the half width. This effect is called broadening of the line, and is due mainly to collisions between molecules and to the Doppler effect. The magnitude of such broadening depends on the temperature, partial pressure, species concentration...The positions of the lines depend mainly on the geometry of the molecule, which determines the energy levels of the rotational and vibrational degrees of freedom. All these efects combined make the absorption coefficient of real gases look like the plots on figure 4.1.

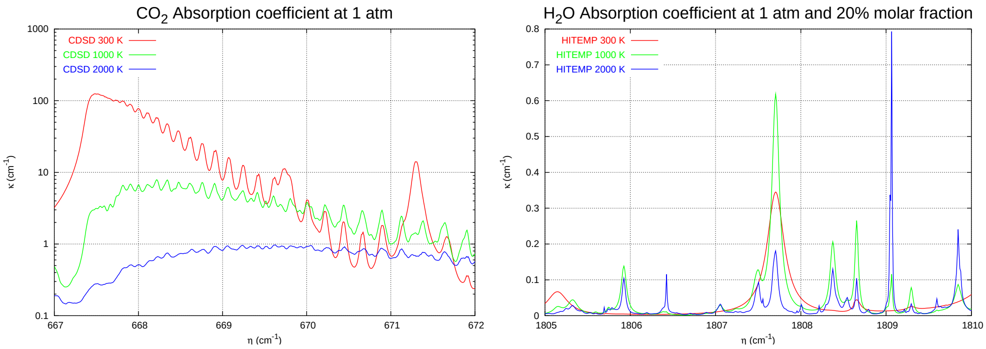

Figure 4.1: Absorption coefficient for a tiny part of the spectrum, at different temperatures. Left: CO_2. As it can be seen, the absorption coefficient varies in several orders of magnitude in a few cm^{-1}. Right: H_2O. Several hot lines are apparent.

There are several research groups that provide detailed information, i. e., high resolution spectral data, of the absorption lines of many gases. The most important, and publicly available via the internet, include the CDSD-1000 [1], HITRAN, and HITEMP [2]. These databases contain information of the absorption lines for several molecules, ranging from few tens of thousands to several million lines, as shown in table 4.1. These absorption lines are in part experimental and in part calculated from quantum mechanics. The most complete database is the HITRAN, with data from 37 different molecules, while the HITEMP includes only the absorption lines of four gases, and the CDSD-1000 databank is devoted only to CO_2.

A key feature for such databases is to correctly predict the so called "hot lines", that is, lines that are not important, concerning to the radiation absorption, at room temperatures, but are important at the high temperatures reached in combustion

Database	Molecule	Number of lines	Year
CDSD-1000	CO_2	3147603	2003
HITEMP	CO_2	1032609	2000
HITEMP	H_2O	1283468	2000
HITRAN	CO_2	62913	2004
HITRAN	H_2O	63196	2004

Table 4.1: Different data bases and number of lines for water vapor and carbon dioxide. Taking into account these numbers, it is clear that approximation methods to non gray properties are needed.

processes. Moreover, the existence of these hot lines makes assumptions like scaled absorption coefficient (see equation 4.17) fail. These hot lines are crearly seen in figure 4.1, for water vapor. For example, lines near $1806.4cm^{-1}$, $1809cm^{-1}$, and $1809.8cm^{-1}$ are hot lines. There are other hot lines, as the line near $1807.7cm^{-1}$, which is hot but at lower temperature. For instance, the HITRAN database does not contain such lines, hence it is suitable for room temperature applications only; therefore the HITEMP database must be used for high (above $1000K$) temperatures. The CDSD-1000 database, on the other hand, is used on a wide range of temperatures.

In heat transfer applications, only scattering by spherical particles is accounted for. This is a good approximation since integration over many irregular particles tends to the same result with spherical particles. The wavelengths of interest are lower than the mean distance between scattering particles, thus independent scattering is assumed to be a good approximation. The scattering by one particle is not influenced by its neighboring particles, and its analisys is simplified. Moreover, the wavelength of radiation is assumed to be larger than the particle size, and therefore the conditions of Rayleigh scattering apply. Under such conditions, which apply for both gas molecules and soot particles, the phase function is relatively smooth and, in addition, the radiation scattering of these particles is negligible compared to the absorption. Therefore, in combustion problems scattering is often not taken into account (Modest [3], p. 398).

The phase function is assumed to depend only on the in-scattering and out-scattering directions (elastic scattering), that is, the energy of a photon does not change during the scattering process. The redistribution of energy, therefore, does not depend on wavelength. Again it is a usual approximation in heat transfer applications [3,4], but for example in optics or when high energy photons (γ-rays) are involved the phase function should account for photon energy change, in the later case due to Compton effect.

4.2 Overview of non gray methods

The wavenumber dependence of the optical properties of real gases is significant mainly in combustion and atmospherical calculations. The former are characterized by large temperature gradients and near constant pressure, thus making the usual assumptions of the optical properties behavior, namely the scaling approximation, less accurate. This is due to the fact that optical properties are more sensible to temperature than to pressure. On the other hand, the atmospherical calculations deal with large variations of pressure, and almost constant temperature field. The situation is now reversed, yielding more accurate predictions in this case.

There are several methods which allows us to take into account non gray radiative heat transfer. By non gray model, or spectral model, we mean any numerical method capable of handle the wavenumber dependence of the optical properties of real gases. Non gray heat transfer implies therefore that such dependence is taken into account. In the following sections some of these non gray models are explained, emphasizing the WSGG and the SLW models, which have been implemented and tested as a part of this thesis.

Non gray methods can be divided roughly in band models and full spectrum models. The former include the SNB and SNBCK models. These methods are more accurate, but far more expensive from a computational point of view. Moreover, band methods provide wavenumber based information, which is rather useless since we are interested only on the total, i. e., spectral integrated, heat transfer. The latter models include the WSGG, the SLW, and the FSCK methods. The main advantage of full spectrum models is that they give directly the spectral integrated heat transfer, with only a few resolutions of the RTE. Thus, it is more appropriate to use full spectrum methods when solving combined heat transfer problems.

Although the non gray methods explained in this work can be used for any gas, provided that the absorption coefficient is known, results concerning CO_2 and H_2O are emphasized. A common approach is to consider the absorption coefficient of CO_2 independent of molar fraction, and take molar fraction effect into account only for H_2O. The reason for such simplification is that, in combustion applications, which are the long term target of the present work, these two gases are by far the most important contributors to radiative transfer for combustion of methane fueled flames in air. Apart from being the most abundant products of the chemical reactions, the contribution of these two gases to radiative transfer at the same molar fractions is also bigger than the contributions of the remaining gases [5].

4.2.1 WSGG Model

The weighted sum of gray gases model is the simplest non gray model, and was first introduced by Hottel and Sarofim [6]. Modest [7] showed that this method can be used for any arbitrary RTE solver. As the main goal of our calculations is the total heat transfer due to radiation, we are not interested on solve each wavenumber in detail. Therefore, global properties such whole spectrum emissivity are considered to obtain numerical parameters for solving the spectral integrated RTE with low computational effort. The analytical solution of the wavenumber dependant RTE is (see section A.1)

$$I_\eta(\ell) = I_{bw\eta}(T_w)e^{-\int_0^\ell \kappa_\eta(\ell')\,d\ell'} + \int_0^\ell I_{b\eta}(\ell')\kappa_\eta(\ell')e^{-\int_{\ell'}^\ell \kappa_\eta(\ell'')\,d\ell''}\,d\ell'. \tag{4.2}$$

The monochromatic intensity radiation field $I_\eta(\ell)$ integrated over the whole spectrum, $I(\ell)$, can be written by means of the total absorptivity, $\alpha(T, 0 \to \ell)$, as

$$I(\ell) = I_{bw}\left(1 - \alpha(T_w, 0 \to \ell)\right) - \int_0^\ell I_b(\ell')\frac{\partial\alpha}{\partial\ell'}(T(\ell'), \ell' \to \ell)\,d\ell' \tag{4.3}$$

provided that the boundaries are black, and

$$\alpha(T, 0 \rightarrow \ell) = \frac{1}{I_b(T)} \int_\eta I_{b\eta}(T) \left(1 - e^{-\int_0^\ell \kappa_\eta(\ell')\, d\ell'}\right) d\eta.$$

In an homogeneous medium, of characteristic length L, the total emissivity $\epsilon(T, L)$ (which equals the total absorptivity) is approximated by a weighted summation of gray gases emissivities:

$$\epsilon(T, L) = \frac{1}{I_b(T)} \int_\eta I_{b\eta}(T) \left(1 - e^{-\kappa_\eta L}\right) d\eta \simeq \sum_{k=0}^{N} a_k(T)(1 - e^{-k_k^* L}). \tag{4.4}$$

The homogeneity requirement allows constant k_k^* coefficients. Plugging the approximated total emissivity from equation 4.4 into equation 4.3, the full spectrum integrated intensity is obtained in this approximation as

$$I(\ell) = \sum_{k=0}^{N} \left\{ I_{bw}(T_w) a_k(T_w) e^{-k_k^* \ell} + \int_0^\ell I_b(\ell') a_k(\ell') k_k^* e^{-k_k^*(\ell - \ell')}\, d\ell' \right\}. \tag{4.5}$$

If the integrated intensity $I(\ell)$ is understood as a summation of gray gas intensities, $I(\ell) = \sum_k I_k(\ell)$, then by comparison between equations 4.2 and 4.5 it becomes clear that the intensity I_k verifies the equation

$$\frac{dI_k}{d\ell} = -k_k^*(I_k - a_k I_b). \tag{4.6}$$

With global (i. e. full spectrum) emissivity data is possible to calculate values for the parameters $a_k(T)$ and k_k^* previously defined. The fit from real emissivity data and the right hand side of equation 4.4 is made for $1 \leq k \leq N$, and for $k = 0$, $k_0^* = 0$ is assumed, and $a_0 = 1 - \sum a_k$ for $1 \leq k \leq N$. Also a range of different characteristic lengths L (or optical depths) is considered. This is to account for the wavenumber ranges where the gas is transparent.

To completely solve the problem, some models are needed to estimate the total emissivity of a gas layer, $\epsilon(T, \tau)$. Modest [3], chapter 9, gives an extensive list of such models. Thus, the required coefficients a_k and k_k^* can be found. The optical thickness of the layer runs from 0 to a big enough value (Modest [7] suggests 100 or 1000 as the upper limit). The emissivity is fitted using N coefficients, from $k = 1$ to $k = N$, according to equation 4.4, where N ranges between 3 and 5.

For instance, we develop the WSGG method for a fictious medium, where the absorption coefficient consists of a single absorption line, with the exponential profile $\kappa(\eta) = \kappa_0 e^{-2|\eta - \eta_0|/\omega}$. We also assume that the black body intensity I_b is almost constant in the line width η_0. Under these conditions, the emissivity can be expressed as

$$\epsilon(T,\tau) \simeq \frac{\pi I_{b\eta_0}}{\sigma_B T^4} \int_0^\infty \left[1 - e^{\tau_\eta}\right] d\eta \simeq b(T)A(\tau), \tag{4.7}$$

where, for an homogeneous medium, $\tau_\eta = L\kappa_\eta$. For an absorption coefficient given by a single line, it is possible to find several models in the literature for the term $A(\tau)$. The dependence of the temperature is reduced to a simple expression. For instance, we can use the approximation given by Modest [3], p. 351, namely

$$A(\tau) \simeq \left\{ \begin{array}{ll} \tau & \text{for } 0 \le \tau \le 1 \\ 1 + \ln\tau & \text{for } 1 \le \tau \end{array} \right. . \tag{4.8}$$

Another choice is to assume the explicit wavenumber dependence of the absorption coefficient. Then, the integral in equation 4.7, $A(\tau)$ can be calculated exactly as

$$A(\tau) = \frac{\omega}{2}\left(\gamma + \ln\tau + \frac{\eta_0}{\omega} + 2E_1(\tau) - E_1(\tau e^{-\eta_0/\omega})\right) \simeq \omega\left(\gamma + \ln\tau + E_1(\tau)\right). \tag{4.9}$$

No matter how $A(\tau)$ is estimated, it is tabulated for several values of τ, from $\tau = 0$ to $\tau = \tau_{\max}$. Since the dependence of the approximated emissivity on the temperature and the optical thickness is separated, we will adjust a set of coefficients c_k and d_k, by demanding that

$$A(\tau) \simeq \sum_{k=1}^{N} d_k(1 - e^{-c_k\tau}),$$

where the coefficients d_k do not depend on the temperature. The coefficients are adjusted by means of a non linear least squares procedure, so that

$$\sum_\tau \left(A(\tau) - \sum_{k=1}^{N} d_k(1 - e^{-c_k\tau})\right)^2$$

is minimal. Table 4.2 shows the values of the coefficients c_k and d_k, for several values of $\tau_{\max}$ and N.

Now, the coefficient k_k^* in equation 4.6 is readily calculated as $k_k^* = c_k\kappa_0$, and the emission related coefficient is given by $a_k = d_k b(T)$. The coefficients given in table 4.2 differ slightly from the coefficients given by Modest [7], especially for large N. This can be attributed to the possibly different functions $A(\tau)$ employed to fit the coefficients. Nevertheless, the fitted $A(\tau)$ is in very good agreement with the fitted $A(\tau)$ reported in the work by Modest.

In a general fashion, the optical thickness and temperature dependence will not be so cleanly separable, resulting in coefficients a_k in equation 4.4 depending on the

$A(\tau)$ approximated				
	$\tau_{\max} = 100$		$\tau_{\max} = 1000$	
N	d_k	c_k	d_k	c_k
2	2.746	0.364	4.576	0.110
	3.046	0.025	3.334	0.0033
3	1.764	0.093	2.512	0.030
	1.883	0.587	2.629	0.404
	2.553	0.014	2.999	0.0024
4	1.291	0.039	1.834	0.011
	1.364	0.193	1.936	0.075
	1.473	0.652	2.040	0.545
	1.974	0.014	2.663	0.0015

$A(\tau)$ analytic				
	$\tau_{\max} = 100$		$\tau_{\max} = 1000$	
N	d_k	c_k	d_k	c_k
2	2.4146	0.2995	4.1934	0.0945
	2.9968	0.0239	3.3068	0.0033
3	1.6257	0.1008	2.2012	0.0211
	1.4963	0.4947	2.7361	0.2420
	2.7219	0.0141	2.8926	0.00205
4	1.2608	0.0339	1.6839	0.0104
	1.4207	0.1301	1.8101	0.0577
	1.3189	0.5448	1.9253	0.3916
	2.3639	0.0073	2.7327	0.0014

Table 4.2: WSGG model coefficients for a fictious medium with only one absorption line. Approximated table fits equation 4.8 and analytic table fits equation 4.9.

temperature. Such temperature dependence of the coefficients a_k is fitted with a polinomial: $a_k(T) = \sum_j h_{kj} T^j$. Smith et al. [8] provide coefficients for H_2O, CO_2, and a mixture of both gases, for a range of partial pressures. The coefficients a_k may also depend on position, for the case in which a non isothermal medium is considered.

The main drawback of the WSGG model is that, for its formulation to be as simple as presented here, only homogeneous media are allowed, although the isothermal condition is not required. This fact restricts its usability in combustion problems where the participating gases are certainly not homogeneously distributed.

4.2.2 SLW Model

Denison and Webb [9] introduced the Spectral Line Weighted sum of gray gases model, SLW, which can be considered as a refinement to the WSGG model, since it can be applied to inhomogeneous media. The monochromatic RTE in a purely absorbing medium is again considered:

$$\frac{dI_\eta}{d\ell} = -\kappa_\eta (I_\eta - I_{b\eta}). \tag{4.10}$$

The absorption coefficient domain is divided into m ranges, bounded by k_{j+1} (high) and k_j (low). A representative absorption coefficient value within each range is chosen, namely $k_j^* = (k_j k_{j+1})^{1/2}$, with $1 \leq j \leq m$. For each absorption coefficient range j, an associated wavenumber range $\Delta\eta_j$ is naturally defined, see figure 4.2, such that for each η in $\Delta\eta_j$, the actual absorption coefficient κ_η lies in the range $[k_j, k_{j+1}]$. Thus, the whole spectrum is divided in m non overlapping bands, in which the absorption coefficient is assumed to be the constant k_j^*. In order to include the spectral zones where the gas is transparent, it is assumed that $k_0^* = 0$. The absorption coefficient ranges, defined by k_j, are usually obtained by equally partitioning a suitable range of cross sections in a logarithmic scale. Usually, it suffices to take $m = 10$ cross section

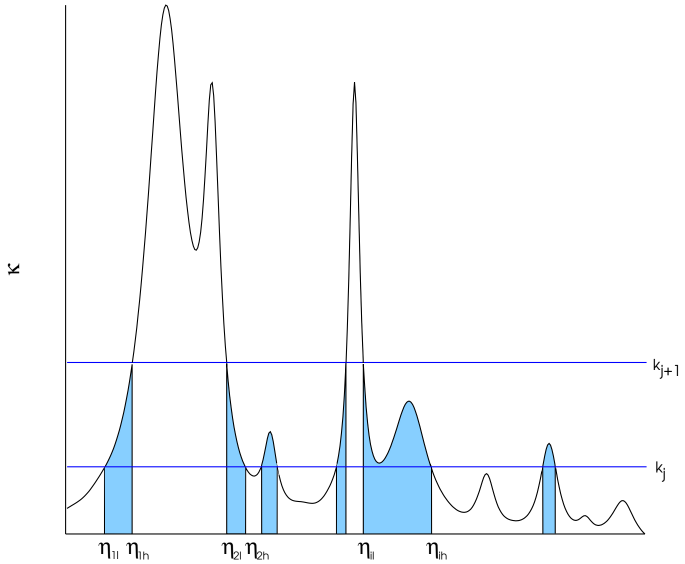

Figure 4.2: Spectral line weighted absorption cross section domain partition, and associated spectral ranges $\Delta\eta_j = \bigcup_i [\eta_{il}, \eta_{ih}]$. The spectral interval $\Delta\eta_j$ is shaded for this particular cross section range j, and the absorption coefficient is assumed to be $(k_{j+1}k_j)^{1/2}$ for all the wavenumbers in $\Delta\eta_j$.

ranges.

The integration of equation 4.10 over all the wavenumbers belonging to the range $\Delta\eta_j$ is carried out. The absorption coefficient is assumed to be the constant k_j^*, as explained before, so it is taken out of the integral. Therefore,

$$\int_{\Delta\eta_j} \frac{dI_\eta}{d\ell}\, d\eta = -k_j^* \left(I_j - \int_{\Delta\eta_j} I_{b\eta}\, d\eta \right), \quad I_j = \int_{\Delta\eta_j} I_\eta\, d\eta. \tag{4.11}$$

Taking into account the Leibniz rule to differentiate under the integral sign, the later expression is equivalent to

$$\frac{dI_j}{d\ell} = -k_j^* \left(I_j - \int_{\Delta_\eta j} I_{b\eta}\, d\eta \right) + \sum_i I(\eta_{h,i,j}) \frac{d\eta_{h,i,j}}{d\ell} - \sum_i I(\eta_{l,i,j}) \frac{d\eta_{l,i,j}}{d\ell}. \tag{4.12}$$

In the above expression, the index i runs over all the sub-ranges of which the $\Delta\eta_j$ is composed (see figure 4.2). In non homogeneous media the two latter terms of equation 4.12 are not necesarily zero. However, as to the total heat transfer, it is assumed that these terms can be ignored. Thus, the radiative transfer equation for each absorption coefficient range can be written as

$$\frac{dI_j}{d\ell} = -k_j^*(I_j - a_j I_b), \quad a_j = \frac{1}{I_b}\sum_i \int_{\Delta\eta_{i,j}} I_{b\eta}\, d\eta. \tag{4.13}$$

Since, by definition, the wavenumber intervals $\Delta\eta_j$ are non overlapping and cover all the spectrum, the integrated intensity over the whole spectrum is simply $I = \sum_j I_j$. A black body distribution function is defined as

$$F(T_b, \bar{\xi}, k) = \frac{1}{I_b(T_b)} \int_{\kappa_\eta(\bar{\xi})<k} I_{b\eta}(T_b)\, d\eta, \tag{4.14}$$

where $\bar{\xi}$ represents the quantities, other than the wavenumber η, on which the absorption coefficient may depend on, basically the temperature and the species molar fraction. Then, the coefficient a_j is readily obtained as $a_j = F(k_{j+1}) - F(k_j)$. It can be easily seen that $\sum_j a_j = 1$ if the appropriate absorption coefficient ranges are selected, that is, if k_m is greater than the maximum κ_η. Notice that the T_b in equation 4.14 is not necessarily the temperature of the gas, included in the set $\bar{\xi}$. The detailed dependence of the absorption coefficient on the wavenumber is needed to compute the black body distribution function F.

There are several ways of obtaining the distribution function F. The first approach is to attempt a fit for the function F. By construction, it is clear that $F(0) = 0$ and $F(k \rightarrow \infty) = 1$, so the target function must behave in the same way. The common choice is a function of the form $F \simeq 0.5 \tanh(P) + 0.5$, where P contains all the details of the absorption coefficient. Correlations based on this function exist in the literature for the computation of the function F for CO_2 [10,11,12] and for H_2O [13].

On the other hand, given the detailed spectral dependence of the absorption coefficient, the distribution function can be calculated for a given physical condition. The procedure explained in [14] is used. Thus, it is possible to build a database of calculated distribution functions, for a set of properties $\bar{\xi}$. To calculate the value of F for any $\bar{\xi}$, linear interpolation is used. The calculations involved prior to use the more accurate F are computationally expensive, but have to be carried out only once. The difference between calculated and fitted distribution functions is shown in figure 4.3, for both CO_2 and H_2O. In addition, since linear interpolation is much faster than numerical computation of a complex function, such as the hyperbolic tangent, solutions using the SLW with interpolated distribution functions are much faster, the maximum speed up achieved for one dimensional problems. The typical speed up in two dimensional cases is about five, while for one dimensional cases, computational time is decreased by a factor of ten or more.

The high resolution absorption coefficient, κ_η, is obtained from the absorption line databases. For CO_2, the CDSD-1000 and the HITEMP are used, while for H_2O

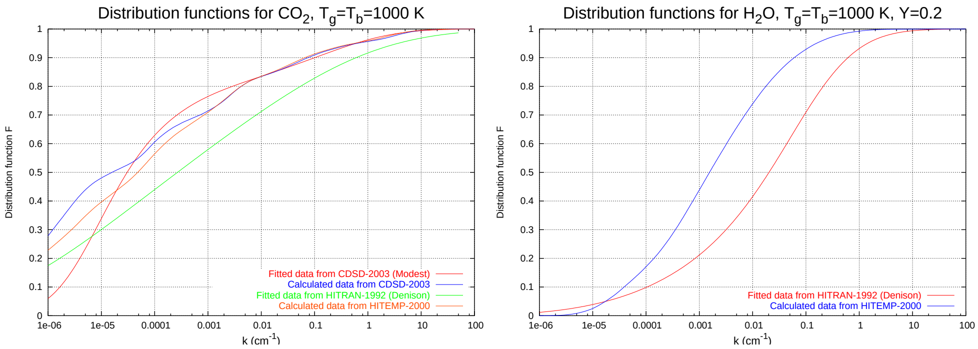

Figure 4.3: Left: Distribution function for CO_2, for a gas temperature T_g of $1000K$. The calculated functions give rather similar values for F, especially for large k. Also, it is clear that the fit by Modest [11] is better. Right: Distribution function for H_2O, for a gas temperature T_g of $1000K$. The difference is due to the different databases used, being the HITEMP more reliable.

only the latter is considered. Following the steps given by Rothman et al. [15], for each absorption line the Lorentz profile is assumed. Next, the desired resolution $\Delta\eta$ of the absorption coefficient is defined, typically $\Delta\eta = 0.01cm^{-1}$, and the spectrum is divided in bins of such width. For each line, the absorption coefficient for the center of the line is calculated, and the computation continues over a number of adjacent bins following the Lorentz profile of the line. One such bin may receive contributions of many lines, and those contributions are added up.

In essence, the SLW model generates a fictious, simplified, absorption coefficient which is based on the actual absorption coefficient. Instead of integrating over wavenumber, we integrate over the absorption coefficient. The wavenumber integral is implicitly carried out in the definition of the distribution function, equation 4.14. From the above formulation of the SLW method, it is clear that it is also applicable in the same form for gray scattering medium, the equation to solve being in this case

$$\frac{dI_j}{d\ell} = -(k_j^* + \sigma_s)I_j + k_j^* a_j I_b + \frac{\sigma_s}{4\pi}\int_{4\pi} I_j \phi \, d\Omega. \tag{4.15}$$

Bounding surfaces need not to be black, as in the WSGG model, although non gray behavior is required. In fact, this gray requirement may be dropped if the wall emissivity is proportional to the absorption coefficient.

An alternative way of defining the weights a_j and the mean absorption coefficients k_j^* that appear in equation 4.13, is by means of an optimization procedure [9]. The total emissivity of a gas layer of thickness between 0 and L is calculated from the distribution function with a large number of absorption cross sections. Such data is then fitted to the function

$$\epsilon(x) \simeq \sum_{i=1}^{m'} a_j \left(1 - e^{-k_j^* x}\right), \quad 0 \leq x \leq L, \tag{4.16}$$

with m' ranges, being m' significantly lower than m, by means of a non linear least squares procedure. These optimized coefficients still can be used for non isothermal, non homogeneous media [5].

In the present work, the total emissivity at a single temperature is considered when finding the optimal a_j and k_j^* coefficients. For an isothermal, homogeneous medium, the weights a_j contain all the information, but for a general case, also the range boundaries k_j are needed. The way to get the boundaries of the spectral ranges from the weights a_j is as follows: first, fit the coefficients for the total emissivity, omitting the transparent band (that is, find a_j and k_j^*, $1 \leq j \leq m'$). Second, compute the transparent band weight, $a_0 = 1 - \sum a_j$. Then set $k_0 = 0$ and $k_j = F^{-1}(\sum a_i)$, for $0 \leq i < j$, so, for example, $k_1 = F^{-1}(a_0)$, $k_2 = F^{-1}(a_0 + a_1)$ and so on. However, it is possible that the mean value k_j^* does not lie between k_j and k_{j+1}, but this fact apparently does not affect the quality of the results obtained with this optimization procedure.

Denison and Webb [10] used the SLW method for non-homogeneous and non isothermal gas layers. In such situations, the absorption coefficient depends on the location. This fact is handled by making both the weights a_j and the coefficients k_j^* position dependent. Thus, the RTE will be solved by taking into account local physical conditions. To determine the best values for these local SLW model coefficients, Denison and Webb [16] considered the absorption coefficient to be scaled, i. e., that it can be written as

$$\kappa_\eta(\bar{\xi}) = \Psi(\eta)\Xi(\bar{\xi}), \tag{4.17}$$

where $\bar{\xi}$ is a set of all the variables (other than the wavenumber η) on which the absorption coefficient may depend on: temperature, pressure, molar fraction... and so on. The scalability property implies that the same spectral intervals $\Delta\eta_j$ can be easily obtained at each point of the domain for a cleverly selected k_{local}^*, therefore the additional terms in equation 4.12 do not appear, making equation 4.13 exact. First, we must pick a reference state ξ_{ref}, and compute the spectral intervals $\Delta\eta_j$ for this reference conditions. For a truly scaled absorption coefficient, the $k_{j,\text{local}}^*$ that yields the same spectral intervals $\Delta\eta_j$ is $k_{j,\text{local}}^* = k_{j,\text{ref}}^* \Xi(\bar{\xi})$, or, if the intervals are the same,

$$F(T_{\text{ref}}, \bar{\xi}_{\text{local}}, k_{j,\text{local}}^*) = F(T_{\text{ref}}, \bar{\xi}_{\text{ref}}, k_j^*) \tag{4.18}$$

must hold. Here we have considered that $\Psi(\eta) = \kappa_\eta(\bar{\xi}_{\text{ref}})$.

The scalability approxmiation, however, is not a very good representation of real gases absorption coefficients, in situations where temperature varies significantly. Nonetheless, we could still pretend that the absorption coefficient is scaled, and assume that there is a value $k^*_{j,\text{local}}$ that yields the same intervals verifies equation 4.18.

The reference state, $\bar{\xi}_{\text{ref}}$, can be calculated by spatial averaging the relevant magnitudes. On the other hand, for some cases, this reference state has been taken by considering the maximum attained by the relevant magnitudes. The choice of this $\bar{\xi}_{\text{ref}}$ has a slight influence on the final result. In order to find the equivalent absorption coefficient, if the scaling approximation does not hold, the Newton method or the bisection method for finding equation roots can be used.

The black body fraction coefficients a_j also depend on the spatial location, via the local temperature. The coefficient $a_{j,\text{local}}$ is calculated as

$$a_{j,\text{local}} = F(T_{\text{local}}, \bar{\xi}_{\text{ref}}, k_{j+1}) - F(T_{\text{local}}, \bar{\xi}_{\text{ref}}, k_j).$$

The spectrum intervals bounded by k_j, with $0 \leq j < m$, are the same over the whole domain, according to the assumptions that hold on the SLW formulation.

The formulation of the SLW method given above is based on the knowledge of the full resolution absorption coefficient. Denison and Webb [17] suggest a method to deal with gas mixtures, using the coefficients of the individual gases. Their approach has been adopted in this work. Consider a mixture of p elements, each of them approximated by m_i cross sections, $1 \leq i \leq p$. The radiative transfer equation is solved $\Pi_i m_i$ times (which gives m^p if all the components are approximated by m ranges), considering all possible combinations of spectral ranges taking exactly one range for each element. Explitictly,

$$a_{\text{mix}} = a_{i,1} a_{j,2} \cdots a_{r,p} \qquad k^*_{\text{mix}} = k^*_{i,1} + k^*_{j,2} + \cdots + k^*_{r,p}, \tag{4.19}$$

where the subindex $i, 1$ indicates the ith range of the first component, and so on. As the number of species increases, the number of times that the RTE has to be solved grows exponentially.

Webb and Solovjov [18] propose several ways to deal with gas mixtures. Its main idea is to obtain equivalent F distribution functions from the monocomponent ones. This is an improvement from previous works [17], where the computation time increases as m^p for a mixture with p species, if the ratio of the mole fractions is not homogeneous. However, several tests conducted seems to point out that these methods are reliable only for optically thick mixtures.

Usually, absorption line databases give the molecular absorption cross section C instead of the absorption coefficient. Both are related by the molar density N, being $\kappa = NC$. Thus, an equation of state for the molar density is needed, and the ideal gas state equation is used. For an ideal, monocomponent gas, the molar density N in mol/m^3 is obtained as $N = 12186.65 P/T$, where the pressure P is in atm and the temperature in K. If the molar density is desired in $molec/cm^3$, then $N = 7.34 \times 10^{21} P/T$. For a gas mixture, the above equation of state holds independently for each gas, $N_i = P_i/RT$, and also for the total pressure and molar density, $N = P/RT$. Solving for RT, we get $P_i = Y_i P$, and $N_i = Y_i P/RT$.

The main advantage of the SLW method is that, once the correlation functions F are fitted from line by line data, the method gives relatively accurate results without the computational requirements of a fully detailed spectral calculation, and thus fully coupled radiation heat transfer plus other heat transfer modes calculations can be carried out with an affordable computational cost.

It is clear that both the SLW and the WSGG methods are very similar, in the sense that the final form of the approximated, spectral integrated, RTE, is the same. The only difference is the calculation of the weights and absorption coefficients, being the SLW more reliable since it is based on the precise position of the absorption lines, instead of being based on a global property such the spectral integrated emissivity. Being so close, numerically speaking, it should not be a surprise that the approximation of the Planck mean absorption coefficient κ_P by both methods is the same. Recalling the assumptions on which the SLW is formulated, κ_P can be written as

$$\kappa_P = \frac{1}{I_b} \int_\eta \kappa_\eta I_{b\eta} \, d\eta \simeq \sum_j a_j k_j^*, \tag{4.20}$$

and the same form is valid also for the WSGG model.

4.2.3 Optically Thin Model (OTM)

Although the optically thin model, OTM, is not a non gray model, it is described here because it is the simplest way to take into account radiation effects in a combined numerical simulation, and is commonly used in combustion applications. It consists of the addition of a source term due to radiation of the form

$$\nabla \cdot \mathbf{q}_r = 4\sigma_B(\kappa_P T^4 - \kappa_{P0} T_0^4), \tag{4.21}$$

where κ_P and κ_{P0} are the Planck mean absorption coefficient (equation 1.21) at temperatures T and T_0 respectively. This approximation assumes that the emission of the flame is much larger than the self absorption, i. e., each photon generated within the flame due to the extremely high temperatures is not absorbed, and thus represents a heat loss wherever the temperature is high. The T_0 is the background temperature, the temperature of the boundaries of the system. In combustion applications, for example, T_0 is usually taken to be the lowest temperature on the domain, thus the OTM overestimates the radiative source term, which results on an underestimation of the temperature field.

This method is often used to compare its results with more sophisticated non gray methods, due to the inherent simplicity of its formulation: in particular, it is very fast, compared to all of the other methods, since the RTE needs not to be solved. Used mainly in combustion problems, it also indicates wether self-absorption is important in the flame under consideration [19,5,20,21,22]. However, in general, radiation self-absorption is important and thus the OTM is not reliable. Wang et al. [21,23] stated that self-absorption plays an important role in NO_x formation in flames. Also, Liu et al. [19] criticize the blind use of this approximation without enough justification.

When using the optically thin model, the Planck mean absorption coefficient used, κ_P, could be obtained from existant correlations, for instance those by Barlow et al. [24]. On the other hand, the value of κ_P could also be obtained from high resolution spectral data, either by detailed line-by-line integration or using approximated methods like the WSGG or the SLW, which are explained in detail in sections 4.2.1 and 4.2.2 respectively.

4.2.4 Statistical Narrow Band Model (SNB-SNBCK)

The statistical narrow band model is based on the formal solution of the RTE along the direction of photon propagation. The fundamental property used is not the absorption coefficient, as in the DOM, but the transmissivity of a layer of gas. Therefore, the use of the DOM is very difficult in this case; for two or three dimensional problems the computational cost of this method comes very high, since the RTE must be solved along the direction of the radiation beam. Kim et al. [25] use the SNB model with the DOM for an unidimensional case.

This model divides the whole spectrum in a number of narrow bands, and the transmissivity is calculated for each band. The RTE has to be solved for each band, and a typical number of such bands is of the order of 300. For inhomogeneous media, approximations for the transmissivity should be employed, being the Curtis-Godson approximation (see Modest [3], p. 346) the most widely used. Liu et al. [26] proposed a new strategy, which is to define an absorption coefficient from the transmissivity of a narrow band, thus allowing the use of any conventional, absorption coefficient based, RTE solver.

On the other hand, the SNBCK model (statistical narrow band correlated-*k*) also divides the whole spectrum in a number of narrow bands, and the black body emissive power is assumed to be constant whithin each band. Thus, the precise knowledge of the absorption lines positions is not needed. Any wavenumber dependant property, such as the transmissivity, originally posed in terms of an integral over the wavenumber, can be rearranged in a smoother, more convenient integral, which allows the use of Gaussian-like integration. From this integral, several absorption coefficients, the number depending on the order of the quadrature, can be inferred, and the RTE is solved by using the DOM and these absorption coefficients. The process is repeated for each narrow band. A deeper explanation of this method can be found elsewhere, for instance the one given by Liu et al. [27].

Several works [19,28,29] use the SNBCK model to consider the radiation effects on combustion problems. The main drawback of such models are that high resolution spectral data is needed, resulting in an increase of the calculation time with respect methods such the SLW. Either the SNB and the SNBCK models provide wavenumber based results, which are useful to compare to experimental results. However, as the total heat transfer, such information is superfluous, and the computational time associated to this extra information is high. A mixture of gases can also be dealt with these models, increasing again the calculation time. Liu et al. [27] explain several strategies to reduce this extra computational effort.

The SNBCK method yields results that agree very well with the SNB, often considered the reference results. Furthermore, the resources needed by the SNBCK are lower, thus reducing the total calculation time. The SNBCK can be viewed as a reformulation of the SNB, with the aim of obtaining the absorption coefficient as the fundamental property, instead of the transmissivity. Thus, efficient methods such as the DOM may be used to solve the RTE.

The SNBCK method is the best choice if the intensity radiation field (or the radiative heat flux) is needed in a wavenumber basis. However, the extra computations required makes this method not very competitive against methods such the SLW or the FSCK if we are only interested in spectral integrated quantities, which is often the case in practical engineering problems.

4.2.5 Full Spectrum Correlated-k Method (FSCK)

Mazumder and Modest [14] developped a precise, mathematical, more rigurous version of the SLW method, and it should be considered its natural replacement. Essentially, a reordering of the wavenumber integration is performed, and a integration over absorption coefficient (instead of an integration over wavenumber) is performed. This is the same principle on which the SLW is based. In the case of scalable absorption coefficient, that is, the absorption coefficient can be writen according to equation 4.17, this method yields exact results, affected only by numerical errors. The prior, absorption data line process that provides the needed parameters of the method is computationally expensive, but it has to be done only once. Detailed, high resolution spectral data of the absorption coefficient is needed. This method, however, cannot handle non-gray surfaces. In their work the FSCK method is applied in a propane combustor, with a simple kinetic model. The same combustor is also solved considering gray properties, and signigicant diferences are observed.

Based on the scaling approximation for the absorption coefficient, Zhang and Modest [30] showed that accuracy of the FSCK method can be significantly improved, by first dividing the spectrum in several, conveniently selected groups. Within each group, the absorption coefficient is approximately scaled, thus giving near LBL accuracy in a reasonable ammount of time.

This method has approximately the same computational cost of the SLW method, once the preprocessing has been completed. The main advantage is that it can be readily used with the existing, DOM based, RTE solver.

4.2.6 Line by line (LBL)

The line-by-line method, LBL, is considered the most accurate method to account for non gray radiation. This method involves, as its name suggests, the solution of the RTE several times for each absorption line. For instance, Denison and Webb [9] solved the RTE as many as ten times between two consecutive lines. Given the number of lines in spectral databases, summarized in table 4.1, it is clear that the demand of computational resources is overwhelming, nowadays and in the years to come.

Furhtermore, the precise knowledge of the contribution of radiation heat transfer is desired usually as a part of more complex problems, thus making the situation worse. For this reason, the use of LBL is not feasible for practical purposes. The importance of line-by-line calculations is that they serve as a benchmark to the simpler models described above, models that are the only real option when non gray radiative heat transfer is to be taken into account in a numerical experiment.

4.3 Comparison between non gray models

Goutière et al. [31] compare several non gray methods in simple cases, where radiation is the dominant mode of heat transfer. Homogeneous as well as inhomogeneous media are considered. They judge the SLW method as the best, taking into account the computational cost, in terms of calculation time and memory requirements, and the quality of the results. However, the best results are obtained with the SNB and SNBCK models. The same conclusion, referring to the SLW, is stated by Coelho [32]. Furthermore, Bedir et al. [33] compare both the SNB and SLW models for a one dimensional diffusion flame, and stated that the two models are in good agreement.

Liu et al. [19] solved a two dimensional coflow flame, by using the SNBCK model. The influence of the number of bands is analyzed, and these results are compared to the OTM model. The difference between both methods exists, although is not very significant. This fact may indicate that, for combustion problems at least, there could be other models, not related to radiation, such as the kinetic or sooting models, that have greater influence on the numerical solution. Thus, it makes no sense to solve a flame with a poor kinetic model and a very accurate non gray model for the radiative transfer of the participant species. Also, the differences between non gray models may be reduced if additional modes of energy transfer are considered.

As stated before, one of the fields where radiation heat transfer is important is the combustion field, mainly due to the high temperatures reached in the reaction zone, while there are zones in the domain at room temperature as well. Amazingly enough, most of the works where numerical simulations of flames are performed, did not consider radiative heat transfer at all. There are few papers where radiation effects are taken into account, and in general the radiation heat transfer is modeled either by a constant source term or by using the OTM method. Others consider the gas mixture to be non participating, thus including only surface radiative heat transfer. This latter aproach does not require the solution of the RTE as explained in chapter 2, and in certain situations seems preferable to the OTM approach, and even to the full solution of the RTE with a gray absorption coefficient (see chapter 6).

The fact that many of the works on numerical simulation of laminar combustion problems do not take into account such refined, non gray models, can be understood considering the huge computational resources that combustion problems require. However, if, when solving flames with accurate reaction models, radiation contributions are neglected or oversimplified, the results may not be better than a simpler reaction model and the finest non gray method. Given the number of non gray models, more numerical experiments should be performed in order to learn how the different levels of detail of non gray and reaction models should be linked.

4.4 Sample calculations

As a part of the work of the present thesis, both SLW and WSGG methods have been coded. The coefficients for the WSGG model used in all calculations are taken from [8]. The motivation to adopt these models is its low computational cost and its simplicity to be incorporated to the implemented DOM solver, explained in chapter 3. Low computational cost is desired, as the next step is to couple radiation heat transfer to the Navier-Stokes and energy equation to simulate more complex problems with non gray gas radiative properties taken into account. With the goal of testing the implementation of both methods, some of the numerical simulations posed by Goutière et al. [31] have been carried out. Their work include both band and full spectrum models, transmissivity or absorption coefficient-based, to solve the RTE for non gray gases.

4.4.1 Homogeneous, isothermal medium

A rectangular cavity of $1m \times 0.5m$, surrounded by cold, black walls, is filled with either CO_2(10%) or H_2O(20%), and maintainted at $1000K$. The wall heat flux and the divergence of heat flux are calculated using both the SLW method and the WSGG method. A good agreement is observed between the calculated values and those reported in the literature. The mesh used has 61×31 nodes, and the step scheme is used within the DOM. The angular quadrature scheme chosen was the T_7 [34], the same used in [31].

From figure 4.4 it is clear that the WSGG model and the SLW model differ in as much as a 4% in the wall heat flux and the heat flux divergence. Part of this difference is due to the fact that different data was employed to fit, respectively, the WSGG model coefficients (data is generated from exponential wide band model) and the

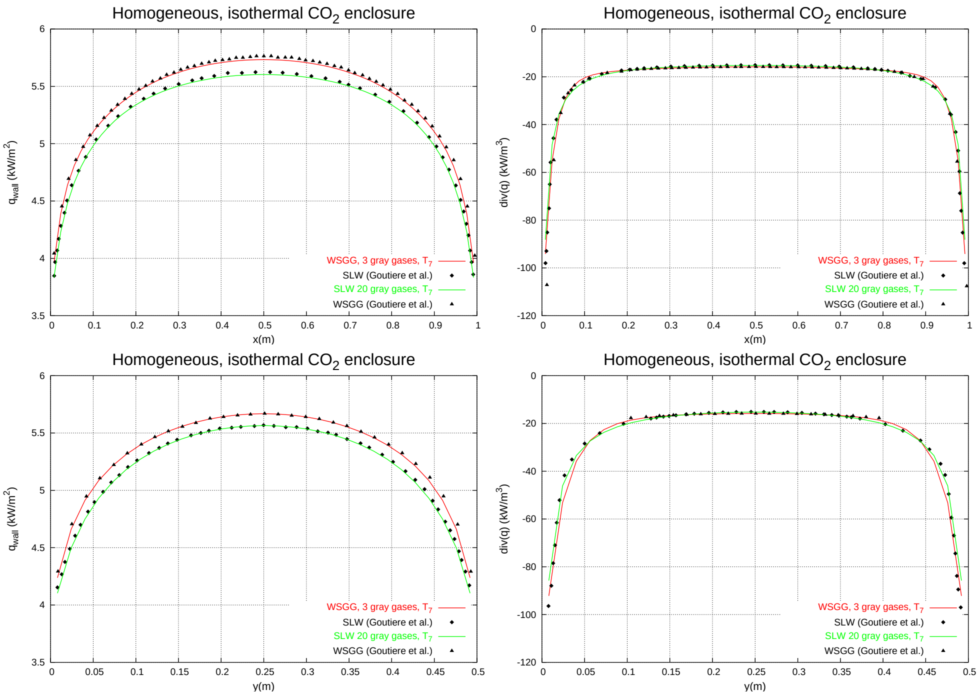

Figure 4.4: Enclosure homogeneously filled with CO_2(10%). Wall heat flux (left) and heat flux divergence on the middle of the cavity (right) are plotted and compared to the values given in [31].

SLW model correlation function (data is from the HITRAN database). Figure 4.5 shows the same problem with H_2O as the radiating gas. The difference between both WSGG and SLW models is much greater. From both figures it is clear that the agreement between our own calculations and the results presented in [31] is quite good.

4.4.2 Homogeneous, non isothermal mixture

The same rectangular enclosure for the cases defined above is considered, this time filled with a mixture of H_2O(20%) and CO_2(10%), total pressure of $1atm$ and the temperature field described in [31], under the label "case 5", intending to reproduce that of a gas combustion in a furnace. The mesh used was the same for the previous cases. Again, the WSGG and the SLW methods are considered. Results plotted in figure 4.6 show the disagreement bewteen the SLW and the WSGG methods.

The divergence of radiative heat flux in the present calculation, using the SLW

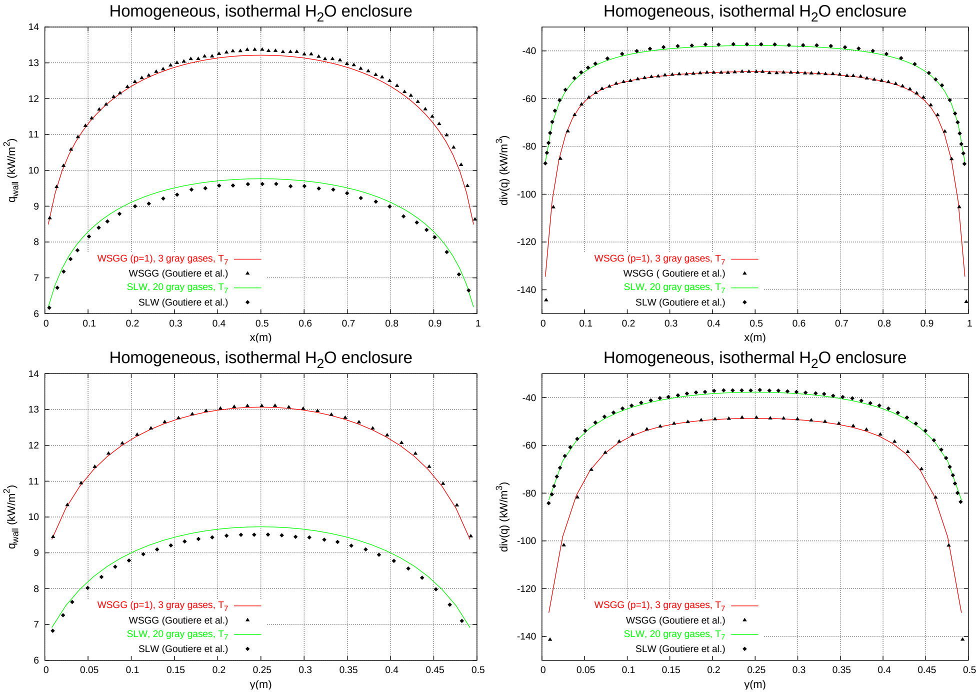

Figure 4.5: Enclosure homogeneously filled with H_2O(20%). Wall heat flux (left) and heat flux divergence on the middle of the cavity (right) are plotted and compared to the values given in [31].

model, shows a fairly good agreement with the reported data, while the radiative heat flux at the walls shows a maximum difference of about a 4%. Notabily, the overall agreement between calculations and reported data is clearly better when the WSGG method is used. The reason may reside on the fact that no free parameters are left in the WSGG method, while the choice of a reference temperature in the SLW method has some influence in the final result, at least on radiation dominated problems.

4.4.3 Homogeneous, isothermal mixture

The SLW model can be, as stated before, very time consuming when a mixture of gases is considered. An alternate implementation to the double integral model for gas mixtures presented by Denison and Webb [16], is developped by Webb and Solovjov [18] to circumvent this limitation. Only homogeneous, isothermal mixtures

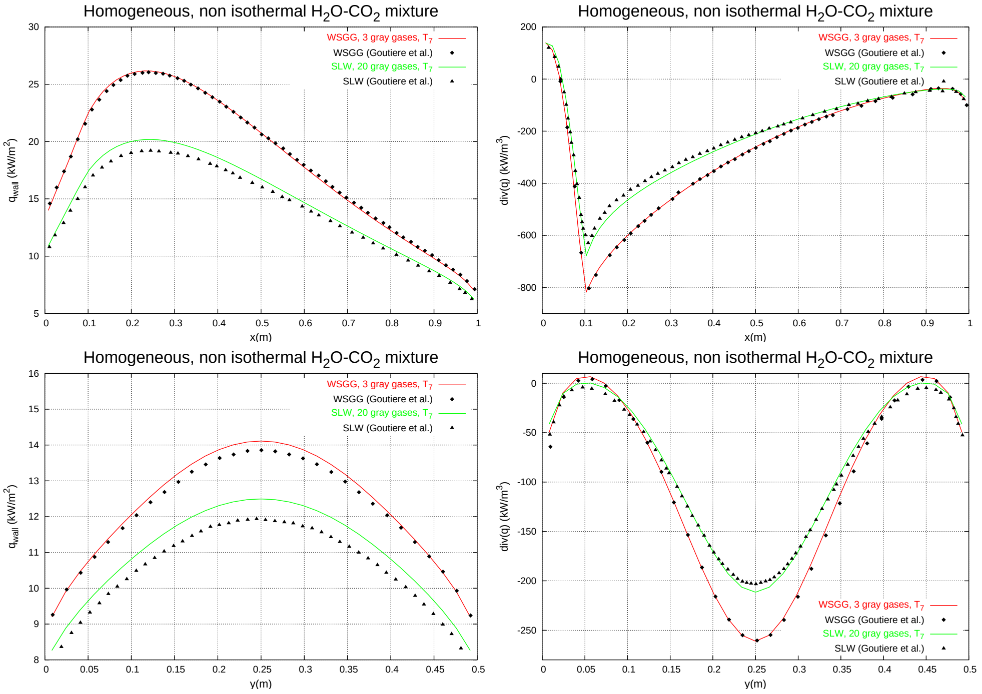

Figure 4.6: Enclosure homogeneously filled with a mixture of CO_2(20%) and H_2O(20%). The temperature field is not constant. Wall heat flux (left) and heat flux divergence on the middle of the cavity (right) are plotted and compared to the values given in [31].

are considered at this stage. The agreement between the double integration approximation and the supperposition or multiplication approaches increases as the optical thickness of the mixture increases. The superposition and multiplication approaches consist on consider a single distribution function for a mixture, F_{mix}. In the superposition approach, we have $F_{\text{mix}}(k) = F_{\text{CO}_2}(k/Y_{\text{CO}_2}) + F_{\text{H}_2\text{O}}(k/Y_{\text{H}_2\text{O}}) - 1$, while the multiplication approach implies $F_{\text{mix}}(k) = F_{\text{CO}_2}(k/Y_{\text{CO}_2})F_{\text{H}_2\text{O}}(k/Y_{\text{H}_2\text{O}})$. Figure 4.7 shows an isothermal, homogeneous layer at $1000K$, bounded by gray walls with an emissivity $\varepsilon = 0.8$, at $0K$ and $2000K$ respectively. The agreement between the different approximations to deal with the gas mixture is clearly better with higher concentrations of participating gases, that is, optically thicker mixtures.

Next, the same situation considered by Denison and Webb [17], consisting on a $3m$ thick layer, surrounded by gray walls with $\varepsilon = 0.8$ and at $400K$ and $1500K$,

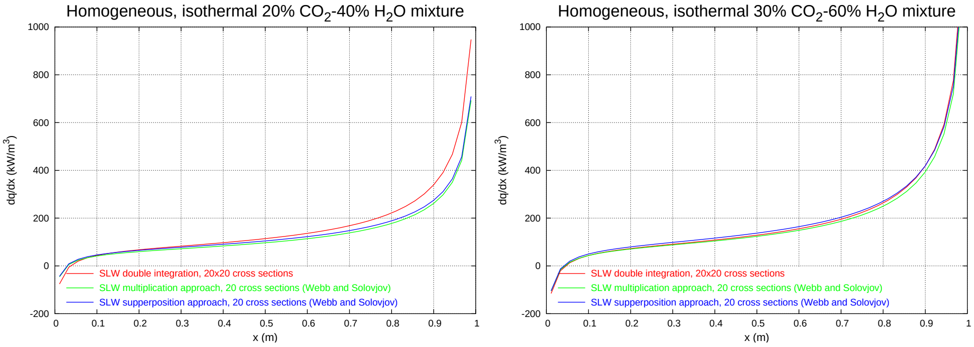

Figure 4.7: Enclosure homogeneously filled with H_2O (left: 40%, right: 60%) and CO_2(left: 20%, right: 30%). The heat flux divergence is plotted.

containing a mixture of 40% H_2O and 20% CO_2 at $1250K$, is solved with several modelizations of the gas mixture, and compared to the line-by-line solution in figure 4.8 (left). The results of the calculation agree with those given in the literature. Further tests suggest that the approximations given by Webb and Solovjov [18] are reliable only for both isothermal and non isothermal, optically thick, homogeneous mixtures. Although only one-dimensional cases are presented, the conclusions still hold for multidimensional problems, as shown in figure 4.8 (right), where the case presented in the previous section is solved for two different species concentration. The relative difference between direct integration and the multiplication approach is seen to be clearly less for the optically thick case —higher concentrations of participating gases.

4.4.4 Non homogeneous, non isothermal medium

The cavity is the same as in the cases above, this time with variable temperature and concentration of the radiating gases, CO_2 or H_2O, according to the functions given in [31] under the labels "case 2" and "case 4". The mesh used is the same of that one used in the previous cases. As the concentration varies throughout the cavity, the WSGG was not used, and results are presented only for the SLW model, using the correlations given in [10, 13]. As stated in section 4.2.2, when the SLW model is employed, the reference temperature from which the effective absorption coefficient is implicitly determined has some impact on the final result. For this particular case, the reference temperature has been taken to be the volumetric mean, that is, $VT_{ref} = \int_V T\,dV$, and a similar criterion has been used to define the reference concentration for the H_2O radiating gas case.

As it is apparent from figure 4.9, the results compare very well, appart from a

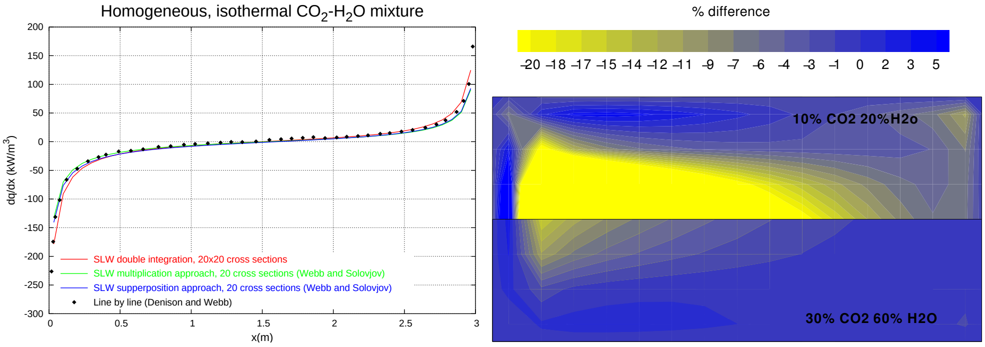

Figure 4.8: Left: Enclosure homogeneously filled with H_2O(40%) and CO_2(20%). Heat flux divergence is plotted and compared to the values given by Denison and Webb [17]. Right: Comparison of the homogeneous, non isothermal mixture case for different concentrations of radiating gases. The difference between direct integration and multiplication approach is plotted.

slight difference for the wall heat flux in the wall at $x = 0$ (about a 2% difference). The greatest difference between the present calculations and the results reported in the literature are those shown in figure 4.10, for radiating gas H_2O. The calculated wall heat flux at the wall at $y = 0$ shows a very good agreement with the reported data. As to the wall at $x = 0$, there are some differences, that are also present in figure 4.9. The heat flux divergence is underpredicted in the center of the cavity, where the concentration of H_2O peaks. This fact is probably due to the different reference concentration used in both calculations. Since the correlation function for CO_2, given in [10], does not depend on the concentration, the difference of the divergence of the radiative heat in the center of the cavity, shown in figure 4.9, is lower than the observed in figure 4.10.

4.4.5 Using optimized coefficients.

Next we perform a comparison between results obtained with optimized and non optimized weights and absorption coefficients, using the SLW model. The optimization procedure is detailed in section 4.2.2. Three one dimensional cases involving gas mixtures are considered, and solved by using either 10 absorption coefficient cross sections and $m' = 5$ optimized coefficients, including the transparent band. The double integration approach [17] is used in both cases. The quadrature scheme selected for the DOM is the S_{12}.

The first case is an homogeneous (10% CO_2, 20% H_2O), isothermal layer set at $T = 1000K$, bounded by cold black walls. The second case, with $L = 1m$, is again

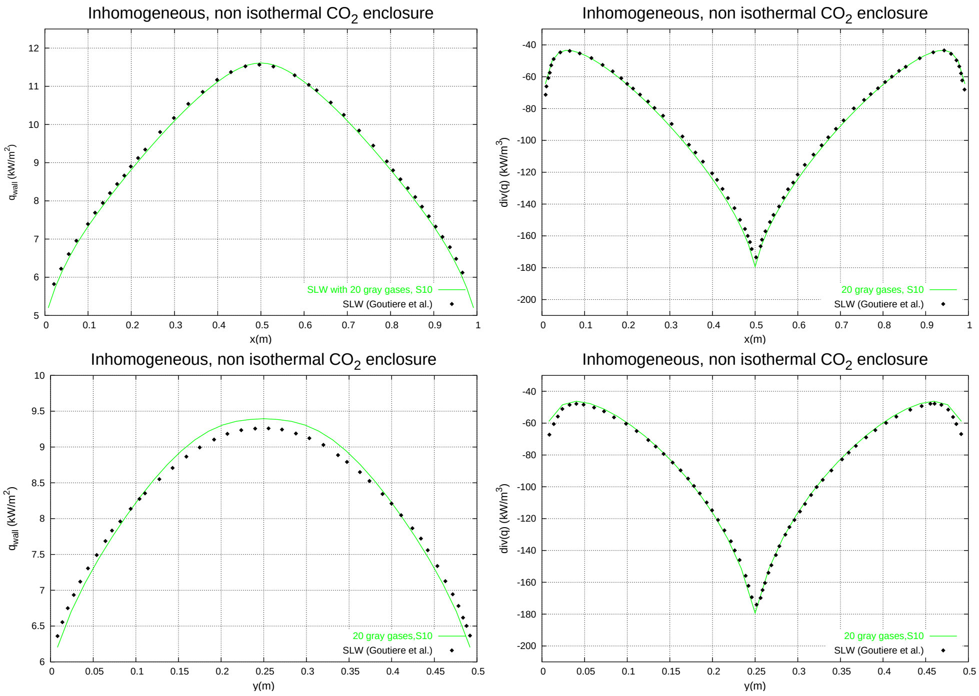

Figure 4.9: Enclosure filled with variable temperature and CO$_2$ concentration. Wall heat flux and heat flux divergence on the middle of the cavity are plotted and compared to the values given in [31].

an homogeneous mixture with the same molar fractions for CO$_2$ and H$_2$O. The temperature profile is $T(x) = 700 - 300\cos(\pi x/L)$, and the enclosing walls are black. In the third case, with $L = 3m$, the temperature is given by the former expression, and the molar fraction varies as $Y_{\mathrm{H_2O}} = 0.2 - 0.15\cos(\pi x/3)$, with $Y_{\mathrm{CO_2}} = 2/3 Y_{\mathrm{H_2O}}$. Again the boundaries are black. For the non isothermal cases, the coefficients for the SLW method were optimized by fitting the total emission data at a reference temperature of $T_0 = 1000K$. The best results using the optimized method are obtained with $L = 10m$ (see table 4.3). In figure 4.11 the results for the above tests are plotted. The agreement between the two approaches is quite good, and the use of the optimized method reduces the computation time approximately by a factor of five.

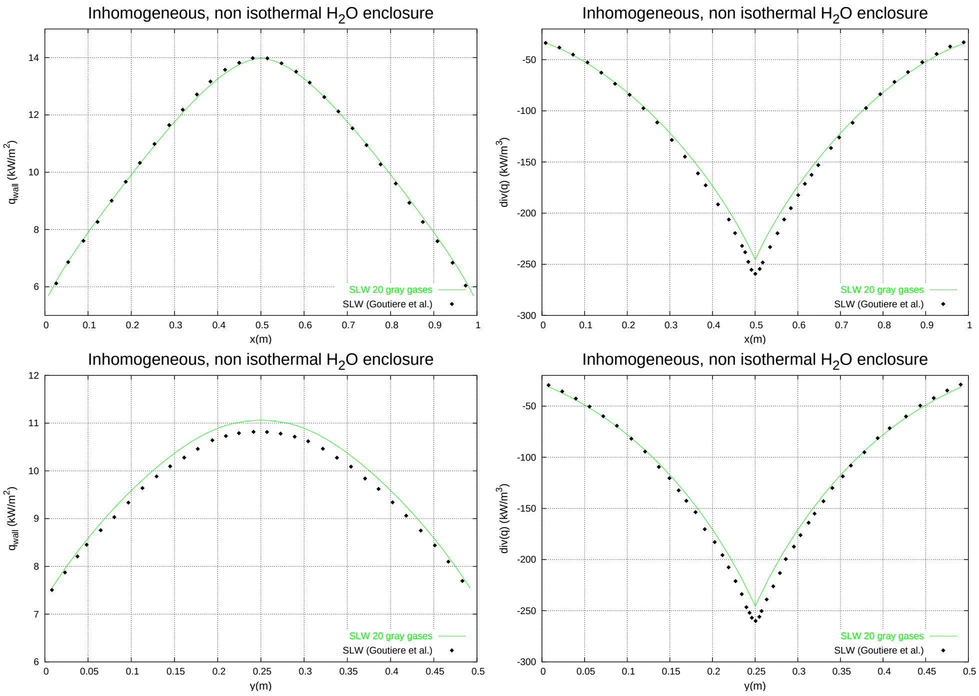

Figure 4.10: Enclosure filled with variable temperature and H_2O concentration. Wall heat flux and heat flux divergence on the middle of the cavity are plotted and compared to the values given in [31].

4.4.6 Using interpolated distribution function

This test case is based on a case described in the previous section: a one dimensional gas layer gas, with the temperature in Kelvin given by $T(x) = 700 - 300\cos(\pi x)$, and two different kinds of layer: first, a single component, homogeneous CO_2 layer with a molar fraction of 10%, and second, a two species, homogeneous, $CO_2{-}H_2O$ layer with molar fractions of 10% and 20% respectively. We have solved the problem using both the correlations for the distribution function F, and interpolated distribution functions. Only CO_2 is expected to give consistent results, since no correlation function for the water vapor is available for the data for which the distribution function could be interpolated, but, for the sake of completeness, results of both simulations are reported.

For the CO_2 layer, the absorption line data from which the distribution function values comes is taken from CDSD-1000 database, and the correlation for the same

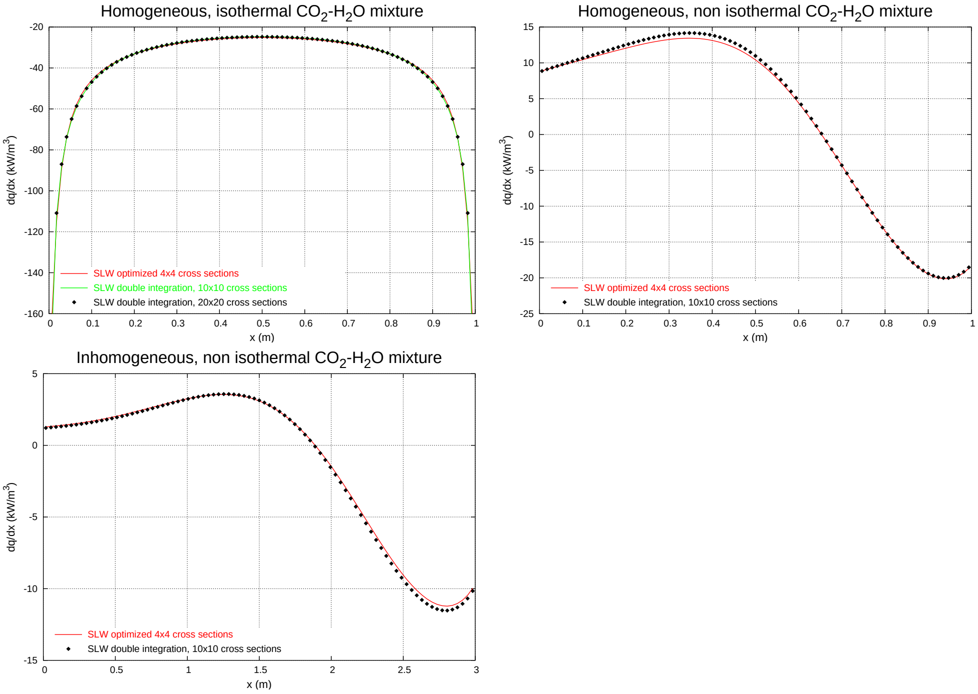

Figure 4.11: Comparison between odrinary absorption cross section range and optimized coefficients SLW.

distribution function is that of Modest and Mehta [11]. For the mixture layer, the same correlation is used for CO_2, while the correlation of H_2O is that given by Denison and Webb [13], based on HITRAN-1992 database. The calculated distribution function comes from the more recent HITEMP-2000 database.

In figure 4.12, left, it can be observed that a good agreement is achieved by both types of distribution function. The wiggles that appear in the interpolated distribution function results arise because the data from which the interpolation is performed is available in ranges of $100K$. On the right plot we can see that the results differ a lot, as expected. It is interesting to note that the wiggles now tend to disappear.

4.5 Conclusions

Both WSGG model and SLW model, for taking into account the strong dependence of the optical properties with the wavenumber, have been successfully coupled with

CO_2	
$k_{s,j}$	a_j
2.304640×10^{-1}	1.662185×10^{-1}
$2.938490 \times 10^{+0}$	9.226138×10^{-2}
$3.103885 \times 10^{+1}$	5.956892×10^{-2}
$5.185114 \times 10^{+2}$	2.879061×10^{-2}
H_2O	
$k_{s,j}$	a_j
2.674673×10^{-1}	3.449689×10^{-1}
$2.468391 \times 10^{+0}$	2.219550×10^{-1}
$1.687439 \times 10^{+1}$	8.874926×10^{-2}
$1.303009 \times 10^{+2}$	1.667433×10^{-2}

Table 4.3: Optimized coefficients from minimization of total emissivity data for $L = 10m$ and $T = 1000K$.

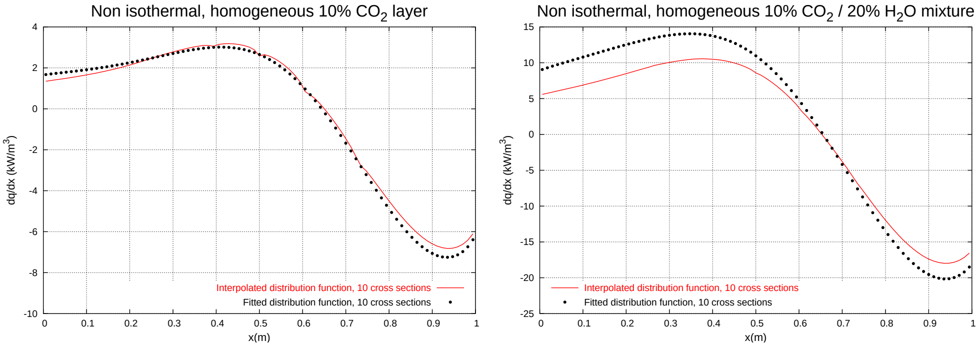

Figure 4.12: Results of interpolated distribution function, obtained from latest absorption line data available, compared to the standard, fitted distribution function, for which several correlations exist. Left: A layer composed of CO_2 only. Right: A composed of a mixture of CO_2 and H_2O.

a general RTE solver such as the DOM. Full spectrum methods, such as the ones explained in this work, are preferred over the band methods, because of the higher computational demands of the latter ones.

With respect to the computation time, WSGG model is clearly faster than the SLW model, but the latter will be affordable even when coupled with the Navier-Stokes and energy equations, and has the advantage of being capable to handle non homogeneous concentration of radiating gases, which will be the case for combustion problems, which are the long term target of our interest. The main problem of the SLW is the lack of correlated functions data for gases other than CO_2 and H_2O, albeit in most combustion problems the only radiating gases are assumed to be CO_2 and H_2O [5], due in part to the inherent gas properties and in part to the low values of the concentration expected for the other gases than CO_2 and H_2O (fuel and products).

The main drawback of the SLW model is the high computation time it takes to solve a problem which involves a mixture of CO_2 and H_2O. In order to overcome this limitation, the approximations presented by Webb and Solovjov [18] are examined, and it is established that these are useful for homogeneous, isothermal mixtures, but for nonisothermal situations, the mixture must be optically thick in order to reliably apply the approximations.

For the reasons above mentioned, mainly its accuracy and affordable computationla cost, the SLW method is judged to be the best choice for a non gray method at the time of writting of this thesis. In addition, this method can be improved further, by using techniques analogous to these described in [30].

References

[1] S. A. Tashkun, V. I. Perevalov, J-L. Teffo, A. D. Bykov, and N. N. Lavrentieva. CDSD-1000, the high-temperature carbon dioxide spectroscopic databank. *J. Quant. Spectrosc. Radiat. Transfer*, 82:165–196, 2003.

[2] L. S. Rothman et al. The HITRAN 2004 molecular spectroscopic databased. *J. Quant. Spectrosc. Radiat. Transfer*, 96(2):139–204, 2005.

[3] Michael F. Modest. *Radiative Heat Transfer*. McGraw Hill, 1993.

[4] M. Necati Özişik. *Radiative transfer and interactions with conduction and convection*. John Wiley & Sons, 1973.

[5] P. J. Coelho, O. J. Teerling, and D. Roekaerts. Spectral radiative effects and turbulence/radiation interaction in a non-luminous turbulent jet diffusion flame. *Combustion and Flame*, 133(1–2):75–91, 2003.

[6] H. C. Hottel and A. F. Sarofim. *Radiative Transfer*. McGraw Hill, 1967.

[7] Michael F. Modest. The Weighted-Sum-of-Gray-Gases Model for Arbitrary Solution Methods in Radiative Transfer. *Journal of Heat Transfer*, 113:650–656, August 1991.

[8] T. F. Smith, Z. F. Shen, and J. N. Friedman. Evaluation of Coefficients for the Weighted Sum of Gray Gases Model. *Journal of Heat Transfer*, 104:602–608, November 1982.

[9] M. K. Denison and Brent W. Webb. A spectral line based weighted sum of gray gases model for arbitrary RTE solvers. *Journal of Heat Transfer*, 115(4):1004–1012, November 1993.

[10] M. K. Denison and Brent W. Webb. Development and application of an absorption-line blackbody distribution function for CO_2. *Int. J. Heat and Mass Transfer*, 38(10):1813–1821, 1995.

[11] Michael F. Modest and Ranjan S. Mehta. Full spectrum k-distribution correlatons for CO_2 from the CDSD-1000 spectroscopic database. *Int. J. Heat and Mass Transfer*, 47(10–11):2487–2491, 2004.

[12] Hongmei Zhang and Michael F. Modest. Full-spectrum k-distribution correlations for carbon dioxide mixtures. *Journal of Thermophysics and Heat Transfer*, 17(2):259–263, 2003.

[13] M. K. Denison and Brent W. Webb. An absorption-line blackbody distribution function for efficient calculation of total gas radiative transfer. *J. Quant. Spectrosc. Radiat. Transfer*, 50(5):499–510, 1993.

[14] Sandip Mazumder and Michael F. Modest. Application of the Full Spectrum Correlated-k Distribution Approach to Modeling Non-Gray Radiation in Combustion Gases. *Combustion and Flame*, 129(4):416–438, 2002.

[15] L. S. Rothman et al. The HITRAN molecular spectroscopic database and HAWKS (HITRAN atmospheric workstation): 1996 edition. *J. Quant. Spectrosc. Radiat. Transfer*, 60(5):665–710, 1998.

[16] M. K. Denison and Brent W. Webb. The spectral line-based weighted-sum-of-gray-gases model in nonisothermal nonhomogeneous media. *Journal of Heat Transfer*, 117(2):359–365, 1995.

[17] M. K. Denison and Brent W. Webb. The spectral line weighted sum of gray gases model for H_2O/CO_2 mixtures. *Journal of Heat Transfer*, 117(3):788–792, 1995.

[18] Brent W. Webb and Vladimir P. Solovjov. SLW modeling of radiative transfer in multicomponent gas mixtures. *J. Quant. Spectrosc. Radiat. Transfer*, 65(4):655–672, 2000.

[19] Fengshan Liu, Hongsheng Guo, and Gregory J. Smallwood. Effects of radiation model on the modeling of a laminar coflow methane/air diffusion flame. *Combustion and Flame*, 138:136–154, 2004.

[20] O. J. Kim, J. P. Gore, R. Viskanta, and X. L. Zhu. Prediction of self-absorption in opposed flow diffusion and partially premixed flames using a weighted sum of gray gases model (WSGGM)-based spectral model. *Numerical Heat Transfer, Part A*, 44:335–353, 2003.

[21] Jingfu Wang and Takashi Niioka. The effect of radiation reabsorption on NO formation in CH_4/air counterflow diffusion flames. *Combust. Theory Modelling*, 5(3):385–398, 2001.

[22] Hongsheng Guo, Yiguang Ju, and Takashi Niioka. Effects of radiative heat loss on the extinction of counterflow premixed H_2-air flames. *Combust. Theory Modelling*, 4(4):459–475, 2000.

[23] Jingfu Wang and Takashi Niioka. Numerical study of radiation reabsorption effect on NO_x formation in CH_4/air counterflow premixed flames. In *Proceedings of the Combustion Institute*, volume 29, pages 2211–2218, 2002.

[24] R.S. Barlow, A.N. Karpetis, and J.Y. Frank, J.H. Chen. Scalar profiles and NO formation in laminar opposed-flow partially premixed methane/air flames. *Combustion and Flame*, 127:2102–2118, 2001.

[25] T. K. Kim, J. A. Menart, and H. S. Lee. Nongray radiative gas analyses using the $S-N$ discrete ordinates method. *Journal of Heat Transfer*, 113:946–952, 1991.

[26] Fengshan Liu, Ömer L Gülder, Gregory J. Smallwood, and Y. Ju. Non-grey gas radiative transfer analyses using the statistical narrow-band model. *Int. J. Heat and Mass Transfer*, 41(14):2227–2236, 1998.

[27] Fengshan Liu, Gregory J. Smallwood, and Ömer L. Gülder. Application of the statistical narrow band correlated-k method to non grey gas radiation in CO_2-H_2O mixtures: approximate treatments for overlapping bands. *J. Quant. Spectrosc. Radiat. Transfer*, 68(4):401–417, 2001.

[28] Fengshan Liu, Hongsheng Guo, Gregory J. Smallwood, and Ömer L. Gülder. Numerical modelling of soot formation and oxidation in laminar coflow nonsmoking and smoking ethylene diffusion flames. *Combust. Theory Modelling*, 7(2):301–315, 2003.

[29] Hongsheng Guo, Fengshan Liu, Gregory J. Smallwood, and Ömer L. Gülder. The flame preheating effect on numerical modelling of soot formation in a two-dimensional laminar ethylene-air diffusion flame. *Combust. Theory Modelling*, 6(2):173–187, 2002.

[30] Hongmei Zhang and Michael F. Modest. Scalable multi-group full spectrum correlated k distributions for radiative transfer calculations. *Journal of Heat Transfer*, 125(3):454–461, 2003.

[31] Vincent Goutière, Fengshan Liu, and André Charette. An assessment of real-gas modelling in 2D enclosures. *J. Quant. Spectrosc. Radiat. Transfer*, 64(3):299–326, 2000.

[32] P. J. Coelho. Numerical simulation of radiative heat transfer from non-gray gases in three-dimensional enclosures. *J. Quant. Spectrosc. Radiat. Transfer*, 74(3):307–328, 2002.

[33] Hasan Bedir, James S. T'ien, and HaeOk Skarda Lee. Comparison of different radiation treatments for a one-dimensional diffusion flame. *Combust. Theory Modelling*, 1(4):395–404, 1997.

[34] C. P. Thurgood, A. Pollard, and H. A. Becker. The T_n quadrature set for the discrete ordinates method. *Journal of Heat Transfer*, 117:1068–1070, November 1995.

5

Combined heat transfer (I): Gray media

Main contents of this chapter have been published as

G. Colomer, M. Costa, R. Cònsul and A. Oliva. Three dimensional numerical simulation of convection and radiation in a differential heated cavity using the discrete ordinates method. *International Journal of Heat and Mass Transfer*, 47(2):257–269, 2004.

5.1 Introduction

Research on the analysis and numerical resolution of heat transfer and fluid flow phenomena where radiant heat exchange has an essential contribution, becomes a key aspect for the employment of Computational Fluid Dynamics (CFD) simulations as a worthwhile complement to experimental research into industry-related problems. These problems involve the resolution of the Navier-Stokes equations and the Radiative Transfer Equation (RTE). The resolution of the RTE implies a considerable computational cost due to the directional nature of the intensity radiation field. This high computational cost limits detail in the simulation of coupled radiation and convection. Therefore, improvements of the numerical methods and fundamental analysis of this complex phenomena have motivated interest in the scientific community.

The main purpose of this chapter is the analysis of the natural convection phenomenon coupled with radiant exchange in a three dimensional differentially heated cavity. The differential heated cavity problem is a classical benchmark test commonly used in the process of CFD codes verification. In this sense, numerical results presented in this work are also addressed to the CFD developers in the task of verifying their codes. Although benchmark solutions can be found for both 2D and 3D discretizations, as in [1,2,3,4,5], the consideration of radiation effects is restricted to 2D geometries. There are also reported solutions to three dimensional problems [6,7], but only taking into account the radiative heat transfer.

The proposed problem has been solved for a range of Rayleigh and Planck numbers, which are the relevant dimensionless numbers for this case, and considering both transparent and gray, purely absorbing homogeneous medium. In the latter case different optical thickness are considered. The effects of radiation are shown and compared to the case where radiation is neglected. The radiation contribution is solved using the Discrete Ordinates Method (DOM), first developed in radiative transfer problems by Truelove [8] and Fiveland [9]. Special emphasis is given to its special features when solving three dimensional problems.

5.2 Choosing the discrete ordinates

The proper choice of weights and ordinates is very important, even in the simplest case where weights are taken to be constant. All results presented in this work make use of such a constant weight scheme.

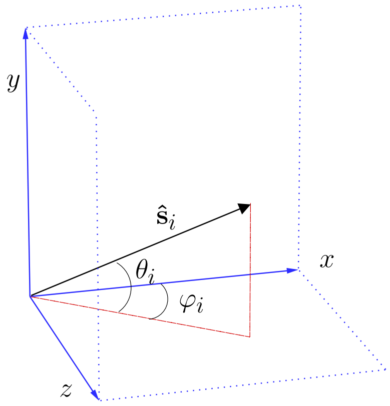

Figure 5.1: Definition of the ordinate $\hat{\mathbf{s}}_i$.

One special requirement when choosing the discrete ordinates is the conservation of energy, that is, discrete ordinates and weights must satisfy the first moment condition (see section 3.2). Whatever the set of ordinates chosen, it must satisfy the discretized equivalent condition which, according to figure 5.1, can be written as

$$\sum_i \mu_i \gamma_i = \sum_i \mu_i^* = \sum_i \mu_i \gamma_i^*, \tag{5.1}$$

where $\mu_i = \cos\theta_i$, $\nu_i = \cos\varphi_i$, $\mu_i^* = \sin\theta_i$, and $\nu_i^* = \sin\varphi_i$.

The condition of energy conservation that should satisfy the set $\{\hat{\mathbf{s}}_i\}$ comes from equation 3.8 with $\hat{\mathbf{n}} \in \{\hat{\mathbf{\imath}}, \hat{\mathbf{\jmath}}, \hat{\mathbf{k}}\}$ and $\hat{\mathbf{n}} \cdot \hat{\mathbf{s}}_i \geq 0$. In order to find the correct weight, it should be noted that, for example, the evaluation of equation 3.8 for $\hat{\mathbf{n}}$ parallel to the x-axis and constant intensity radiation field yields

$$\pi = \int_{\hat{\mathbf{\imath}} \cdot \hat{\mathbf{s}}_i \geq 0} (\hat{\mathbf{\imath}} \cdot \hat{\mathbf{s}}_i) d\Omega \simeq 4\omega \sum_i \mu_i \nu_i, \tag{5.2}$$

where an additional factor of 4 appears since the ordinates are only defined for one octant and the sum extends over four octants. A set of directions verifying the above conditions can be obtained as follows: given N_p and N_a directions with constant polar (resp. azimuthal) angle θ_l (resp. φ_m), N is the total number of ordinates in a quadrant $N = N_a N_p$. Therefore the values of the angles are

$$\varphi_m = \frac{\pi}{4N_a}(2m-1) \quad \text{and} \quad \theta_l = \alpha + (l-1)\gamma,$$

where $1 \leq m \leq N_a$ and $1 \leq l \leq N_p$. Also $\alpha = \arctan\xi - \pi(N_p - 1)/6N_p$, $1/\xi = 2N_a \sin(\pi/4N_a)$ and $\gamma = \pi/3N_p$.

With those definitions of the discretized directions, it can be seen, by taking the limits $N_p \to \infty$ and $N_a \to \infty$, that while the azimuthal angles φ_m lie in the range between 0 and $\pi/2$, the polar angles θ_l lie in a narrower range, approximately $\pi/6$ radians above and below an angle of $\arctan(2/\pi)$ ($\simeq 32.5°$), thus not covering the whole octant. Despite this limitation, when the results obtained with this set of ordinates are compared to the results obtained with more general sets, such as those presented in table 3.1 (the S_{10} ordinate set), there is a good agreement. The comparison was made for radiative equilibrium as well as for combined conduction and radiation cases.

A number of ordinates must be chosen taking into account that accurate results with admissible computational cost are desired. Three dimensional DOM calculations for rectangular furnaces (such as the one in [6]) give accurate results with three directions per octant. Assuming that this accuracy will also hold for the differentially-heated cavity, the choice $N_p = 3$ and $N_a = 2$ seems to be a reliable one. The resulting weights and ordinates are given in table 5.1. Once the ordinate set is obtained, the RTE is solved as explained in section 3.3.

5.3 The coupling between radiation and convection

The flow is assumed to be laminar and steady state. All physical properties are taken to be constant, except for the density to allow natural convection. The usual

Direction	θ_i	φ_i	Weight
$\hat{\mathbf{s}}_1$	0.229613	0.392699	0.261799
$\hat{\mathbf{s}}_2$	0.229613	1.178097	0.261799
$\hat{\mathbf{s}}_3$	0.578679	0.392699	0.261799
$\hat{\mathbf{s}}_4$	0.578679	1.178097	0.261799
$\hat{\mathbf{s}}_5$	0.927745	0.392699	0.261799
$\hat{\mathbf{s}}_6$	0.927745	1.178097	0.261799

Table 5.1: Directions and weights in the first octant ($x \geq 0$, $y \geq 0$, and $z \geq 0$) used to solve the RTE, all angles are in radians.

Boussinesq approximation is used for the density in the body force term

$$\rho = \rho_0(1 - \beta(T - T_0)).$$

Under these assumptions, the Navier-Stokes Equations together with the energy equation can be written in dimensionless form as follows:

$$\begin{aligned} \boldsymbol{\nabla}^* \cdot \mathbf{v} &= 0, && (5.3) \\ (\mathbf{v} \cdot \boldsymbol{\nabla}^*)\, \mathbf{v} &= -\boldsymbol{\nabla}^* P^* + \sqrt{\frac{Pr}{Ra}} \nabla^{*2} \mathbf{v} + \left(T^* - \tfrac{1}{2}\right) \hat{\mathbf{u}}_g, && (5.4) \\ \sqrt{Ra\, Pr}\, (\mathbf{v} \cdot \boldsymbol{\nabla}^*)\, T^* &= \nabla^{*2} T^* - \boldsymbol{\nabla}^* \cdot \mathbf{Q}_r^*, && (5.5) \end{aligned}$$

where the radiative dimensionless divergence term is calculated as the difference between the emission and the absorption:

$$\boldsymbol{\nabla}^* \cdot \mathbf{Q}_r^* = \frac{\tau}{Pl} \left[4 \left(\frac{T^*}{T_0^*} + 1 \right)^4 - \int_{4\pi} I^*(\mathbf{r}, \hat{\mathbf{s}})\, d\Omega \right] \tag{5.6}$$

and $I^*(\mathbf{r}, \hat{\mathbf{s}})$ is the dimensionless intensity radiation field which solves the dimensionless version of equation 1.9. Notice that the pressure radiation term is neglected, since it is proportional to the second moment of the intensity divided by the speed of light c. Therefore this term is not relevant for heat transfer applications.

For the optically thick limit (i.e. $\tau \to \infty$) the additive model has been considered. This model consists in independently solving the radiative equilibrium case for a large optical thickness and the Navier-Stokes equations without taking into account radiation effects. Then, the total heat flux is the addition of the heat flux given by each independent solution.

The flow structure and the temperature field are governed, for a given optical thickness τ, by the Rayleigh number (Ra), the Prandtl number (Pr), the Planck number (Pl) and T_0^*, which are

$$Ra = \frac{g\beta \Delta T L^3 \rho_0^2 c_p}{k\mu}; \quad Pr = \frac{\mu c_p}{k}; \quad Pl = \frac{k\Delta T}{L\sigma_B T_c^4}; \quad T_0^* = \frac{T_c}{\Delta T}. \tag{5.7}$$

The Planck number is a measure of the conduction heat transfer relative to a mean heat transfer due to radiation. It is clear from equations 5.6 and 5.7 that, as the thermal conductivity k increases, the Planck number also increases and the radiation effects become less noticeable. The adiabatic boundary condition includes a conduction term and a radiation term $Q_r^*(\hat{\mathbf{n}})$, calculated with the aid of equation 1.2. The temperature at any of the adiabatic walls is such that

$$\hat{\mathbf{n}} \cdot \boldsymbol{\nabla}^* T^* = Q_r^*(\hat{\mathbf{n}}) = \frac{1}{Pl} \int_{4\pi} d\Omega \, (\hat{\mathbf{n}} \cdot \hat{\mathbf{s}}) I^*(\mathbf{r}, \hat{\mathbf{s}}). \tag{5.8}$$

In the case of transparent medium, radiation effects depend only on the temperature of the boundaries, since $\boldsymbol{\nabla} \cdot \mathbf{Q}_r^*$ is zero inside the enclosure. From the above boundary condition it is clear that, for a large Planck number, the radiation effects may be discarded since the temperature gradient will go to zero —the boundary condition required when radiation effects are ignored.

5.4 Code verification

The numerical code employed in this chapter was verified by means of the resolution of several benchmark problems, some of them with analytical solutions and others given in the literature. Among them, the code was verified considering problems where radiation plays a dominant role, problems with transparent and participating media and problems considering 2D-coupled radiation and natural convection. The main results of this verification process are described in [5].

The verification of three-dimensional geometries has been completed, and the simulation of a rectangular furnace has been taken into account, by comparing the results obtained with those presented by Mengüç and Viskanta [7]. This comparison is described in detail in the next section.

5.4.1 Rectangular Furnace

The three-dimensional rectangular furnace studied encloses a purely absorbing medium (see figure 5.2). The dimensions are $2m \times 2m \times 4m$ —in the x, y and z directions respectively. The walls of the small faces are at $1200K$ and $400K$ while the other four walls are maintained at $900K$. The walls are supposed to reflect and emit

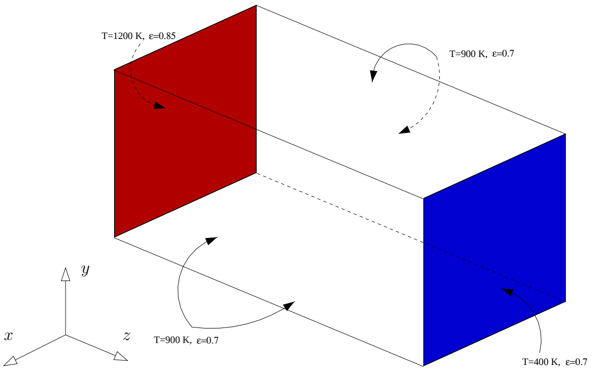

Figure 5.2: Problem description of the validation case.

diffusely, and to have emissivities of 0.85 for the hot wall and 0.7 for the remaining walls.

In this problem, conduction and convection effects are neglected. Hence, the medium is assumed to be at radiative equilibrium, with an additional homogeneous heat source of $\mathcal{S} = 5kW/m^3$. The radiative equilibrium condition implies that the only term in the energy equation is the divergence of radiative heat. In the presence of a source term $\mathcal{S}$, the energy equation is simply $\boldsymbol{\nabla} \cdot \mathbf{Q}_r + \mathcal{S} = 0$. Using the dimensional form of equation 5.6, the temperature that makes the energy equation hold can be calculated as

$$T_{re}(\mathbf{r}) = \left(\frac{1}{4\sigma_B} \left[\int_{4\pi} I(\mathbf{r}, \hat{\mathbf{s}})\, d\Omega - \frac{\mathcal{S}}{\kappa} \right] \right)^{1/4} .$$

Two different absorption coefficients, $\kappa = 0.5m^{-1}$ and $\kappa = 1m^{-1}$, are considered. The results plotted in figure 5.3 and were computed with a $40 \times 40 \times 80$ control volume mesh, considering $N_p = 4$ and $N_a = 3$.

The temperature distribution at mid-height on the hot wall (for $z = 2m$ and $y = 1m$) is plotted as a function of the dimensionless x^* direction in figure 5.3 (left). The agreement between the results presented in [7] and the results obtained with the DOM method is quite good. It can be observed that temperatures near the walls are not exactly the imposed wall temperatures ($900K$); the reason is that heat conduction has been neglected.

The net heat flux on the hot wall and at mid height ($z = 0m$ and $y = 1m$) as a function of the dimensionless x^* direction is plotted in figure 5.3 (right). Lower net heat fluxes in comparison with those reported in [7] are obtained, especially for the optically thinner medium. The differences may be due to the fact that a coarser mesh

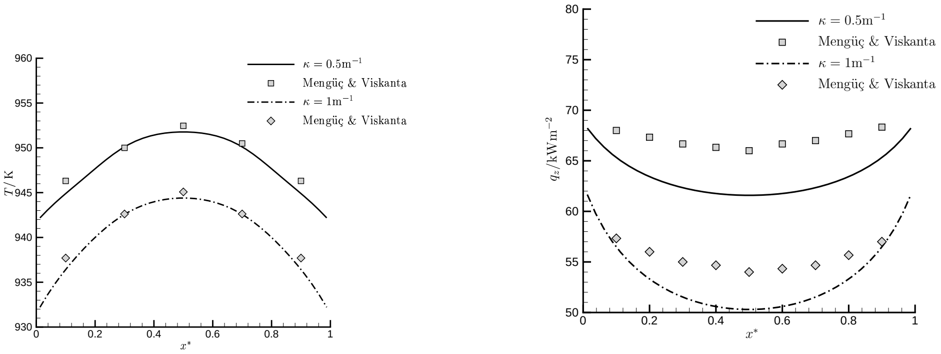

Figure 5.3: Left: Temperature profiles for $z = 2m$. Data from ref. [7] corresponds to zonal method. Right: Radiation heat flux at hot wall. Data from ref. [7] corresponds to P_3 method.

than the one used in this work was used in [7], and also that the RTE was solved using spherical harmonics decomposition (P_3 approximation). It has been shown that the differential approximations of the P_3 method are not reliable for optically thin media ($\kappa < 1$) [10]. In addition, it has also been shown that the P_3 method over-predicts the heat flux values in these situations, which is consistent with the results obtained here with the DOM.

5.5 Numerical results

A cubic enclosure containing a gray fluid is assumed, shown in figure 5.4. Both transparent and participating medium are considered. The west wall is at T_h and the east wall at T_c with $T_h > T_c$. The remaining four walls are adiabatic. The walls of the cavity are black. The Prandtl number has been fixed to 0.71, and a range of Rayleigh numbers, from $Ra = 10^3$ to $Ra = 10^6$, is studied. In the case of a transparent medium, a longer cavity is also solved, where the depth of the domain is four times that of the cube. The solution of this stretched cavity is compared to a purely two-dimensional differentially-heated cavity.

Results are presented for the dimensionless total heat flux at the hot wall, which can be calculated as

$$Q^* = \left(-\frac{\partial T^*}{\partial x^*} + Q_r^* \right)_{x^*=0} . \tag{5.9}$$

Q^* has been considered the significant result to be presented for the three dimen-

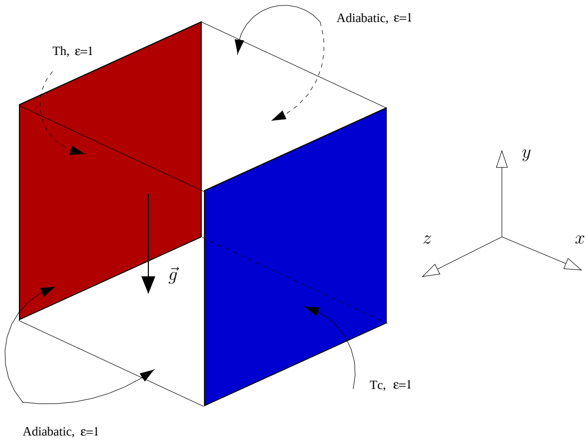

Figure 5.4: Three dimensional differential heated cavity scheme.

sional differential cavity solutions throughout this chapter. Whenever possible, radiation and convection contributions (Q_r^* and Q_c^*) to the total heat transfer are given.

5.5.1 Discretization

A study was performed to analyze the influence of the mesh spacing on the final result. Four different meshes, with 17^3, 33^3, 65^3 and 97^3 control volumes were used for what was considered to be a reference problem ($Ra = 10^6$, $Pr = 0.71$, $Pl = 0.016$, $T_0^* = 17$ and $\tau = 1$). The conclusions obtained in this single problem have been assumed for the range of governing numbers presented in this chapter.

The convergence to an asymptotic solution can be observed by evaluating the mean differences of temperature, radiative heat and velocity fields between one simulation and its previous coarser solution. In table 5.2, the mean differences and mean heat flux at the hot wall are shown. As can be seen, differences lower than 1% are obtained comparing the third and fourth discretizations. These results motivate the selection of the third mesh (i. e. the mesh with 65^3 control volumes) as fine enough to perform the numerical studies. The set of ordinates used for this benchmark problem is that obtained with $N_p = 3$ and $N_a = 2$ (table 5.1).

5.5.2 Transparent medium

The medium is assumed to be non-participating ($\tau = 0$). The Planck number is set to $Pl = 0.043$, and $T_0^* = 15$. For the stretched cavity, the number of control volumes is doubled in the z direction.

The first result presented in figure 5.5 shows the averaged heat flux (in y^* direc-

Mesh	$\overline{\delta(T^*)}$	$\overline{\delta(Q_r{}^*)}$	$\overline{\delta(v_x^*)}$	$\overline{\delta(v_y^*)}$	$\overline{\delta(v_z^*)}$	$\overline{Q^*}$
17 × 17 × 17	—	—	—	—	—	14.42
33 × 33 × 33	2.0%	2.9%	2.7%	2.0%	2.1%	14.28
65 × 65 × 65	1.0%	1.5%	1.5%	1.1%	1.3%	13.84
97 × 97 × 97	0.2%	0.4%	0.6%	0.4%	0.4%	13.75

Table 5.2: Mean difference for temperature, radiative heat and velocity fields between two consecutive meshes, and mean heat flux at hot wall for the benchmark differential heated cavity problem: $Ra = 10^6$, $Pr = 0.71$, $Pl = 0.016$, $T_0^* = 17$, and $\tau = 1$.

tion) at the hot wall as a function of the position along the z axis when radiation is taken into account. The simple case when radiation heat exchange is ignored is plotted in the right side of figure 5.5. When both figures are compared, it can be seen that radiation significantly increases the heat transfer. The increase of the heat flux is greatest for low Rayleigh numbers. The reason is that the contribution of convection heat transfer becomes more important as Rayleigh number increases, and the contribution of radiative heat transfer remains almost constant (the Planck number has been kept constant). The velocity field only affects the radiation field slightly, through the variation of the temperature at the adiabatic walls, according to equation 5.8.

The effect of radiation and convection on the heat flux can clearly be seen in table 5.3, where the average heat flux is given. In table 5.4 some local values of the velocity field and heat flux are given. It can also be observed in figure 5.5 that there is an increase of the heat flux at both ends of the z axis when radiation is present. This effect is more intense for low Rayleigh numbers. This increase is due to the influence of the nearby walls.

	With radiation			Without radiation	
Ra	Q^*	Q_r^*	Q_c^*	Q^*	Fusegi et al. [1]
10^3	4.596	3.162	1.434	1.055	1.085
10^4	5.295	3.233	2.062	2.030	2.100
10^5	7.368	3.385	3.983	4.334	4.361
10^6	11.670	3.568	8.102	8.862	8.770

Table 5.3: Hot wall average heat flux. Q_r^* and Q_c^* are the radiation and convection contribution to the total heat flux. $Pl = 0.043$, $T_0^* = 15$, $\tau = 0$, and $Pr = 0.71$.

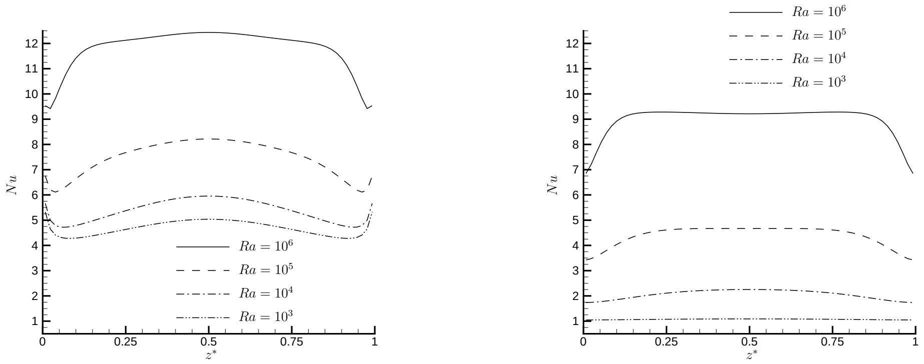

Figure 5.5: Left: Average heat flux in the y^* direction versus depth z^*. Transparent medium, $\tau = 0$, $Pl = 0.043$, $T_0^* = 15$, and $Pr = 0.71$. Right: Average heat flux in the y^* direction versus the depth z^* without radiation. $Pr = 0.71$.

	$Ra = 10^3$	$Ra = 10^4$	$Ra = 10^5$	$Ra = 10^6$
v_x^* max	0.1250	0.2170	0.1869	0.1284
y^*	0.808	0.838	0.869	0.900
z^*	0.500	0.500	$0.285^\dagger$	$0.208^\dagger$
v_y^* max	0.1271	0.2333	0.2865	0.2985
x^*	0.177	0.131	0.069	0.038
z^*	0.500	$0.269^\dagger$	$0.115^\dagger$	$0.069^\dagger$
Q^* max	6.350	7.238	10.793	19.168
y^*	~ 0	~ 0	0.192	0.069
z^*	0.500	0.500	0.500	$0.208^\dagger$
Q^* min	3.960	3.729	3.724	4.025
y^*	0.900	0.900	0.931	0.961
z^*	$0.085^\dagger$	$0.100^\dagger$	$0.085^\dagger$	$0.038^\dagger$

Table 5.4: Local extreme values for velocity and heat flux. v_x^* max. refers the plane $x^* = 0.5$ and v_y^* max. to the plane $y^* = 0.5$. The maximum and minimum heat flux refer to the hot wall ($x^* = 0$). The ~ 0 indicates that the maximum was obtained at the first calculation node. The † symbol indicates that the same value was also obtained at location $1 - z^*$. All variables are symmetric respect to the plane $z^* = 0.5$. Transparent medium, $\tau = 0$, $Pl = 0.043$, $T_0^* = 15$, and $Pr = 0.71$.

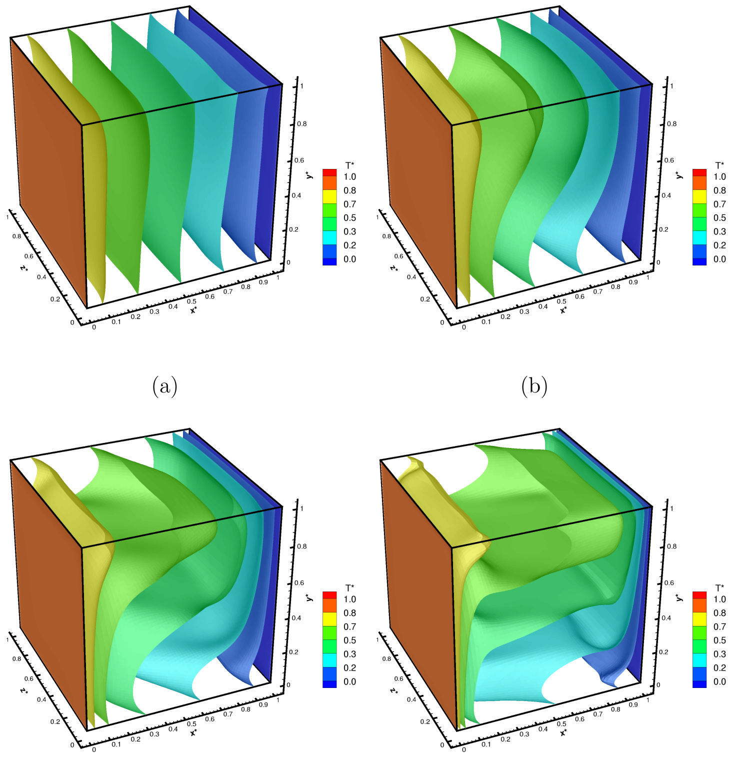

(a) (b)

(c) (d)

Figure 5.6: Transparent medium, $\tau = 0$. Isothermal surfaces for $Pl = 0.043$, $T_0^* = 15$, $Pr = 0.71$, and four Rayleigh numbers: $Ra = 10^3$ (a), $Ra = 10^4$ (b), $Ra = 10^5$ (c) and $Ra = 10^6$ (d)

In figure 5.6, isothermal surfaces are shown for all Rayleigh numbers considered. For low Rayleigh numbers the conduction heat transfer prevails and the isotherms are nearly vertical (parallel to the gravity field). For high Rayleigh numbers, the isotherms become more horizontal, since the natural convection term, which dominates the conductive term, tends to convey the hottest fluid above the coldest. Thus the isotherms are nearly horizontal (perpendicular to gravity field) in the middle region of the enclosure.

The three-dimensional simulations have been compared to two-dimensional results. The two-dimensional enclosure is discretized in a 65 × 65 control volume mesh. In figure 5.7a the isotherms of the three-dimensional cavity at $z = 2$ (solid lines) and the isotherms of the purely two-dimensional case (dashed lines) are plotted. A good agreement is achieved between both solutions. This means that the effect of the end walls ($z = 0$ and $z = L_z$) is small.

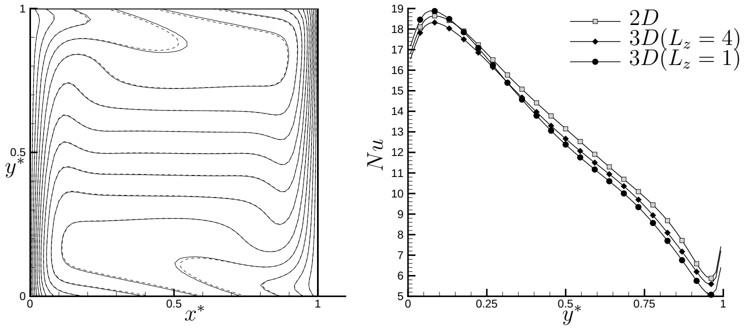

(a) (b)

Figure 5.7: Comparison between the two-dimensional solution and the three-dimensional stretched cavity. Transparent medium, $\tau = 0$, $Pl = 0.043$, $Pr = 0.71$, and $Ra = 10^6$. Isothermals (solid lines for $3D$ cavity, dashed lines for $2D$ cavity)(a). Local heat flux number at hot wall (b).

In figure 5.7b the local heat flux at the hot wall as a function of the dimensionless height y^* is plotted for the two-dimensional case, for a cubic three-dimensional case and for the mid-plane of the 3D stretched cavity. As the depth L_z of the box increases, the heat flux is closer to the two-dimensional solution. Some differences persist between three-dimensional and two-dimensional cases, probably due to the effects of the end wall.

5.5.3 Participating medium

Now the medium is assumed to be participating, with a specified optical thickness. The dimensionless reference temperature is fixed to $T_0^* = 17$. In order to emphasize the radiative effects, the Planck number is decreased to $Pl = 0.016$. In figure 5.8, isothermal surfaces are shown for all Rayleigh numbers tested, and for an optical thickness of $\tau = 10$.

A comparison of the averaged heat flux (in the y^* direction) for three dimensional cavity enclosing a participating medium has been carried out. Figure 5.9 shows the averaged heat flux versus the depth z^* for several optical thicknesses: $\tau = 0$ (non

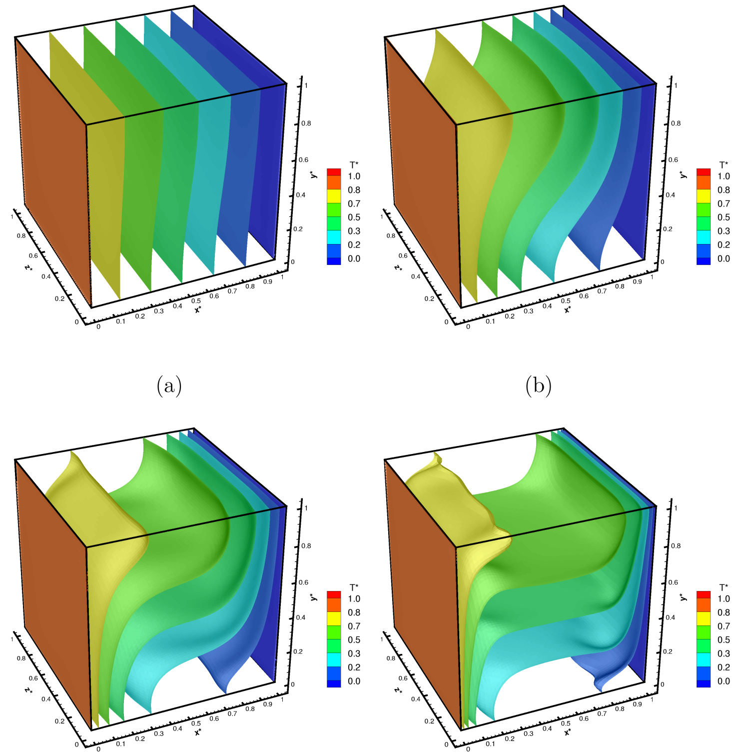

(a) (b)

(c) (d)

Figure 5.8: Transparent medium, $\tau = 0$. Isothermal surfaces for $Pl = 0.043$, $T_0^* = 15$, $Pr = 0.71$, and four Rayleigh numbers: $Ra = 10^3$ (a), $Ra = 10^4$ (b), $Ra = 10^5$ (c) and $Ra = 10^6$ (d)

participating medium), $\tau = 1$, $\tau = 10$, additive model (optically thick limit, $\tau \to \infty$) and a non radiating enclosure.

The participating medium gives lower values of the heat flux than the transparent one. This decrease is due to the fact that part of the energy emitted from the surfaces is absorbed within the medium. Radiative heat exchange takes place between the hot wall and an effective plane which has a higher temperature than the cold wall. It is worth noting that the effect of the increase of the local heat flux at both ends of the z-axis is more important for transparent fluids. As the opacity of the fluid increases,

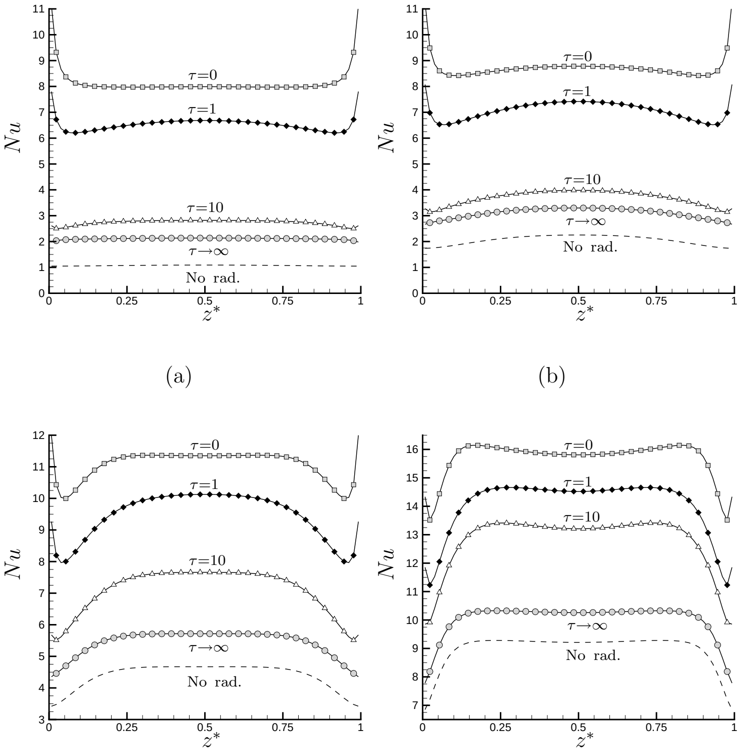

(a) (b)

(c) (d)

Figure 5.9: Average heat flux at hot wall versus depth z^*. Participating medium, $Pl = 0.016$, $T_0^* = 17$, $Pr = 0.71$, and four Rayleigh numbers: $Ra = 10^3$ (a), $Ra = 10^4$ (b), $Ra = 10^5$ (c) and $Ra = 10^6$ (d).

this effect tends to disappear.

In figure 5.10 the detailed contribution of convection and radiation to the total heat flux is shown for different values of Rayleigh number and the optical thickness. The radiation contribution highly depends on the optical thickness τ, while the convection contribution is nearly independent of τ, appart from wall effects on the lower $Ra = 10^3$ case (figure 5.10a). Also notice that for the $\tau = 0$ case, the radiation contribution is almost the same for both values of Ra.

The mean heat flux, together with the convection and radiation contribution at

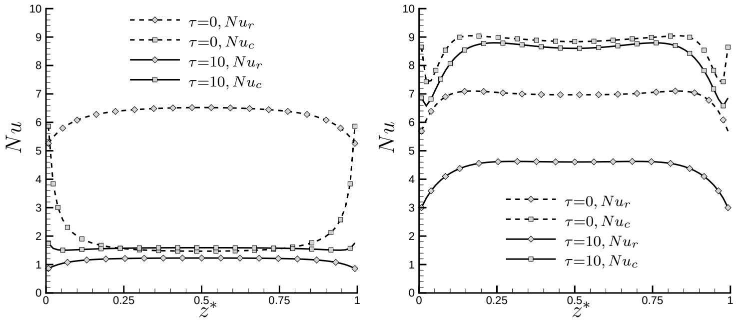

(a) (b)

Figure 5.10: Plot of detailed convection and radiation contribution to total heat flux through hot wall versus depth z^*. Participating medium, $Pl = 0.016$, $T_0^* = 17$, and $Pr = 0.71$. Two values of Ra are presented: $Ra = 10^3$ (a) and $Ra = 10^6$ (b).

the hot wall for different Rayleigh numbers and optical thickness are presented in table 5.5. Notice that Q_c^* is nearly independent of the optical thickness, while for $\tau = 0$, Q_r^* remains almost constant for increasing values of the Rayleigh number. In table 5.6, local values of the velocity field and heat flux are given for a participating medium with $\tau = 10$.

Additional results are presented in figure 5.11. The heat flux increases if the Rayleigh number increases, and it decreases for larger optical thickness. The figure also shows the validity of the additive model for low Rayleigh numbers. Although the additive model is only strictly valid for $\tau \to \infty$, it can be seen in figure 5.11 that

Ra	$\tau = 30$	$\tau = 10$	$\tau = 1$	$\tau = 0$
10^3	1.80(0.50,1.30)	2.70(1.16,1.54)	6.40(4.64,1.76)	7.96(6.20,1.76)
10^4	2.87(0.79,2.08)	3.65(1.54,2.11)	6.94(4.69,2.25)	8.54(6.28,2.26)
10^5	5.94(1.60,4.34)	7.01(2.80,4.21)	9.32(5.44,3.92)	10.89(6.52,4.37)
10^6	11.54(2.86,8.68)	12.64(4.36,8.28)	13.88(6.25,7.63)	15.48(6.84,8.64)

Table 5.5: Average heat flux at the hot wall for a range of Rayleigh numbers. Radiative and convective contributions to total heat transfer are shown in parentheses, i.e. (Q_r^*, Q_c^*). Participating medium, with $Pl = 0.016$, $T_0^* = 17$, and $Pr = 0.71$.

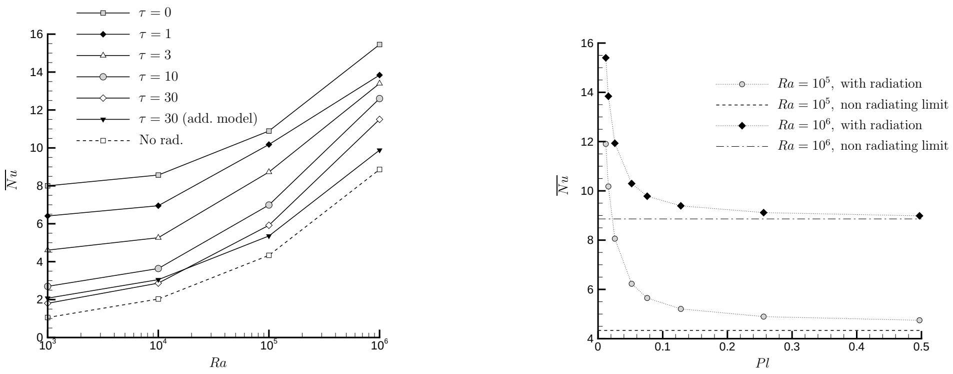

Figure 5.11: Left: Mean heat flux at hot wall for several Rayleigh numbers. Participating medium, $Pl = 0.016$, $T_0^* = 17$, and $Pr = 0.71$. Right: Total heat flux at hot wall versus Planck number. Participating medium, $\tau = 1$, $T_0^* = 17$, $Pr = 0.71$.

	$Ra = 10^3$	$Ra = 10^4$	$Ra = 10^5$	$Ra = 10^6$
v_x^* max	0.1304	0.2720	0.2620	0.1796
y^*	0.823	0.838	0.869	0.900
z^*	0.500	0.500	$0.269^\dagger$	$0.223^\dagger$
v_y^* max	0.1296	0.2805	0.3275	0.3282
x^*	0.177	0.131	0.085	0.038
z^*	0.500	0.500	$0.131^\dagger$	$0.069^\dagger$
Q^* max	3.115	5.767	11.569	22.260
y^*	0.208	0.162	0.161	0.069
z^*	0.500	0.500	$0.346^\dagger$	$0.238^\dagger$
Q^* min	2.147	1.593	1.864	2.658
y^*	~ 1	~ 1	~ 1	~ 1
z^*	$\sim 1^\dagger$	$\sim 1^\dagger$	$\sim 1^\dagger$	$\sim 1^\dagger$

Table 5.6: Local extreme values for velocity and heat flux. v_x^* max. refers the plane $x^* = 0.5$ and v_y^* max. to the plane $y^* = 0.5$. The maximum and minimum heat flux refer to the hot wall ($x^* = 0$). The ~ 1 indicates that the maximum was obtained at the last calculation node. The † symbol indicates that the same value was also obtained at location $1 - z^*$. All variables are symmetric respect to the plane $z^* = 0.5$. Participating medium, $\tau = 10$, $Pl = 0.016$, $T_0^* = 17$, and $Pr = 0.71$.

it gives reasonable results for low Rayleigh numbers from $\tau \geq 30$. For higher values of *Ra* the optical thickness should be larger in order to apply the additive model.

The problem has also been solved for a range of Planck numbers, for $Ra = 10^6$ and $Ra = 10^5$, $Pr = 0.71$, $T_0^* = 17$, and optical thickness $\tau = 1$. The total heat flux at the hot wall versus the Planck number is plotted in figure 5.11 (right). The two limiting cases are for $Pl \to \infty$, when the conduction heat transfer is more important than the radiative heat transfer (the medium behaves as if no radiation heat transfer takes place), and for $Pl \to 0$ $(k \to 0)$, when the medium is at a radiative equilibrium (there is no heat flux due to conduction, and hence $Q^* \to \infty$). The average heat flux behaves as expected and tends to the limiting cases explained above.

5.6 Conclusions

In this chapter, the coupling between radiation and convection has been studied, for both transparent and participating media, in a differentially-heated cavity. The influence of Rayleigh and Planck numbers, as well as the optical thickness, have been analyzed.

It has been shown that, in a transparent medium, radiation significantly increases the heat flux, and that for a given Planck number and constant reference temperature ratio T_0^*, the contribution of radiation remains almost constant for a range of Rayleigh numbers.

For participating media, defined by its optical thickness, the total heat flux also increases as the Rayleigh number increases. On the other hand, an increase on the optical thickness causes a decrease in the heat flux. The optically thick limit tends to the case where radiation is neglected, but with a higher thermal conductivity. The explanation seems to be that, for large optical thickness, radiation becomes a local phenomenon, behaving as a conduction phenomenon, which, according to [11], can be described with the Rosseland radiative conductivity (the so-called diffusion approximation). The additive model has been shown to be accurate for low values of *Ra*. For higher values of the Rayleigh number, the optical thickness should be larger in order to apply the additive model, which saves computational time and resources.

The effect of the Planck number has also been studied. It has been shown that, for $Pl > 0.5$, the radiation effects can be neglected for low optical thickness. For low Planck numbers ($Pl < 0.01$), the radiation effects dominate and the convection terms of the governing equations can be ignored, and the so-called radiative equilibrium hypothesis can be applied.

All computations presented in this work were performed on a AMD K7 900 Mhz processor with 512 MB of RAM memory. A converged solution of the benchmark problem, with the normalized residual of the temperature field lower than 10^{-9}, takes an average of three days with this computer.

References

[1] T. Fusegi and J. Min Hyun. Laminar and transitional natural convection in an enclosure with complex and realistic conditions. *Int. J. Heat and Fluid Flow*, 15(4):258–268, August 1994.

[2] G. De Vahl Davis. Natural convection of air in a square cavity: a benchmark numerical solution. *International Journal for Numerical Methods in Fluids*, 3:249–264, 1983.

[3] A. Yücel, S. Acharya, and M. L. Williams. Natural convection and radiation in a square enclosure. *Numerical Heat Transfer, Part A*, 15:261–278, 1989.

[4] Abdeslam Draoui, Francis Allard, and Claudine Beghein. Numerical analysis of heat transfer by natural convection and radiation in absorbing, emitting and scattering fluids enclosed in square cavities. *Heat and Technology*, 10(1–2):160–177, 1992.

[5] G. Colomer, M. Costa, R. Cònsul, and A. Oliva. Radiant exchange in domains with obstacles using the discrete ordinates method. In *Proceedings of the Fifth European Congress on Computational Methods in Applied Sciences and Engineering (ECCOMAS)*, pages 1–20, 2000.

[6] Selçuk, N. and Kayakol, N. Evaluation of discrete ordinates method for radiative transfer in rectangular furnaces. *Int. J. Heat and Mass Transfer*, 40(2):213–222, 1997.

[7] M. P. Mengüç and R. Viskanta. Radiative transfer in three-dimensional rectangular enclosures containing inhomogeneous, anisotropically scattering media. *J. Quant. Spectrosc. Radiat. Transfer*, 33(6):533–549, 1985.

[8] J. S. Truelove. Discrete-ordinate solutions of the radiation transport equations. *Journal of Heat Transfer*, 109(4):1048–1051, 1987.

[9] W. A. Fiveland. Discrete-ordinates solutions of the radiative transport equation for rectangular enclosures. *Journal of Heat Transfer*, 106:699–706, November 1984.

[10] A. C. Ratzell III and J. R. Howell. Two-dimensional radiation in absorbing-emitting media using the $P - N$ approximation. *Journal of Heat Transfer*, 105:333–340, 1983.

[11] K. H. Lee and R. Viskanta. Two-dimensional combined conduction and radiation heat transfer: comparison of the discrete ordinates method and the diffusion approximation methods. *Numerical Heat Transfer, Part A*, 39:205–225, 2001.

6

Combined heat transfer (II): Non gray media

Main contents of this chapter have been submitted for publication to the *Journal of Quantitative Spectroscopy and Radiative Transfer*

6.1 Introduction

In the early days of computational fluid dynamics, radiative heat transfer was not taken into account because of the overwhelming amount of computational resources it required. The following, natural step, was to consider only radiative exchange between surfaces, which does not involve the solution of the Radiative Transfer Equation (RTE). As the computational resources increased, detailed numerical models were conceived, such as the Discrete Ordinates Method (DOM), which allowed the resolution of participating media. In the last decade of the last century, feasible, as well as accurated, non gray radiation models, were formulated. These models can be broadly divided in full spectrum models and band models. The former, which include the Weighted Sum of Gray Gases (WSGG) model [1], the Absorption Distribution Function (ADF) model [2], and the Spectral Line Weighted sum of gray gases (SLW) model [3], are accurate enough, particularly in homogeneous cases. The later, which include the Statistical Narrow Band (SNB), and the Statistical Narrow Band Correlated$-k$ (SNBCK) model [4], are more precise than global models, but far more resource demanding.

The simplest non gray model ever formulated is the WSGG, and it was used by Mesyngier and Farouk [5] to analyze the coupling between non-gray gas radiation and turbulent natural convection. In their work, the radiating gases were considered as an homogeneous mixture. Soufiani and Djavdan [6] compared this method to the SNB method for combustion applications. While the WSGG predicted well radiative heat source for a hot medium surrounded by black walls, the absorption by a cold gas of radiation emitted by hot walls was generally underestimated. The authors attributed this discrepancy on total absorption to the fact that the weights in WSGG model were always taken at the temperature of the emitting body.

Belonging to the full spectrum group, both the SLW and ADF models are more precise than the WSGG. For instance, the SLW weights, depend on the local temperature and could lead to more accurate predictions. Coelho et al. [7] used the SLW model to account for turbulence-radiation interaction in a diffusion flame. The inclusion of non gray radiative properties improved the agreement between the computed and the measured data. Soufiani et al. [8] employed the ADF model for a mixed laminar convection case, considering an homogeneous gas mixture. Their conclusion was that, by taking radiation into account, the flow is affected significantly.

On the other hand, band models are more accurate than full spectrum, or global, models. Liu et al. used the SNBCK model for laminar ethylene [9] and laminar methane/air [10] flames. In the latter flame, which can be considered optically thin, it turns out that radiation model did not have much influence in the outcome. Coelho [11] also used a correlated$-k$ band model, this time with a prescribed temperature and concentration fields, obtained from experimental measures. The works by Liu et al. [10] and Coelho [11], however, pointed out that turbulence and combustion models may have greater influence in the final result than the non gray radiation model. Soufiani et al. [12] also used a correlated$-k$ model to solve a forced convection situation, considering pure gases only. In their work, preheating or precooling of the gas in the entrance of a circular duct due to radiation was studied. Comparison with the ADF model showed that for the precooling condition the ADF performs well, while bigger differences between the band and the global models were obtained for higher temperatures. Lacroix et al. [13] considered radiation and conduction energy transport in a water curtain. Non gray radiation absorption, as well as scattering, were taken into account, by using a band-like model with a reduced number of bands.

Among the different non-gray models mentioned above, the SLW model stands out for its level of accuracy and for the low (compared to band models) computational resources it requires. In this chapter the performance and implementation of the SLW model is analyzed in detail. When considering a non-gray model, the SLW in our case, one realizes that there are plenty of strategies that can be adopted. There are several databases with absorption line data which can be used, one may opt for use fitted distribution functions or calculated ones, one may use high resolution partitions of the absorption coefficient domains or optimized coefficients. . . All of these factors possibly have an impact on the results, which may, or may not, be significant. If radiation is not the only mode of heat transfer, this significance can be different wheter radiation is globally meaningful or not.

In order to study the impact of these different approaches of the SLW model, this chapter presents the numerical analysis performed in a thermal driven cavity where the coupling of non-gray radiation and convection is taken into account: first, by varying the convective contribution, and second, by considering two cases, one of which is radiation dominated and the other where radiation and conduction are roughly equally significant. These calculations are compared to gray solutions, to stress the appropriateness of the use of the non-gray SLW model, with the different approaches detailed in section 6.2.3.

6.2 Mathematical model

We consider a non reactive, steady state mixture of gases in order to study the influence of the SLW model parameters on a complex problem, which combines also convection and conduction heat transfer. The mixture of gases consists of N_2, which is considered transparent to radiation, and CO_2 and H_2O, which absorb and emit, but do not scatter, radiation. The relevant governing equations are adapted from [14], which are valid for reactive flows, and hold for low Mach number, with frictional heating and pressure time variation neglected.

6.2.1 Convection and conduction transport

For the above mentioned steady-state gas mixture, with average velocity $\mathbf{u}$, the mass conservation equation reads

$$\boldsymbol{\nabla} \cdot (\rho \mathbf{u}) = 0. \tag{6.1}$$

Momentum conservation leads to

$$\rho \left(\mathbf{u} \cdot \boldsymbol{\nabla} \right) \mathbf{u} = -\boldsymbol{\nabla} p + \rho \mathbf{g} + \boldsymbol{\nabla} \cdot \mathbf{S}, \tag{6.2}$$

where $\mathbf{S}$ is the shear stress tensor, and the energy conservation equation reads

$$\rho c_p \left(\mathbf{u} \cdot \boldsymbol{\nabla} \right) T = \boldsymbol{\nabla} \cdot (k \boldsymbol{\nabla} T) - \boldsymbol{\nabla} \cdot \mathbf{q}_r. \tag{6.3}$$

Notice that the pressure radiation term is neglected, since it is proportional to the second moment of the intensity divided by the speed of light c. Therefore this term is unimportant for heat transfer applications.

The physical properties are considered to be temperature dependent. In order to find the individual molecular transport properties, the CHEMKIN database is used to generate the coefficients of its temperature expansion. For the mixture, each individual property is properly averaged [14].

6.2.2 Radiation transport

The radiative transfer equation, abbreviated RTE (see section 1.4), is solved in detail, taking into account the real, wavenumber dependent, absorption coefficient of CO_2 and H_2O. The monochromatic radiative transfer equation for a non scattering medium is considered. For a given direction defined by coordinates $\{\mu, \xi\}$, the RTE is

$$\mu \frac{\partial I_\eta}{\partial x} + \xi \frac{\partial I_\eta}{\partial y} = -\kappa_\eta \left(I_\eta - I_{b\eta} \right), \tag{6.4}$$

where $\mu = \cos\theta \cos\varphi$ and $\xi = \sin\theta$, see figure 3.1 (left). Both the intensity radiation field I, and the absorption coefficient κ, depend on wavenumber η. The radiative source term $\nabla \cdot \mathbf{q}_r$ can be obtained from the RTE solution as

$$\nabla \cdot \mathbf{q}_r = 4\kappa_P \sigma_B T^4 - \kappa_G G, \tag{6.5}$$

where $\kappa_P I_b = \int_\eta \kappa_\eta I_{b\eta}\, d\eta$ and $\kappa_G G = \int_\eta \kappa_\eta G_\eta\, d\eta$. The monochromatic incident radiation on a control volume is $G_\eta = \int_{4\pi} I_\eta\, d\Omega$. This term is then plugged into the energy equation 6.3.

6.2.3 Modeling of the absorption coefficient

As stated before, e use the SLW model, outlined here for convenience. Following the work by Denison and Webb [3], the monochromatic RTE in a purely absorbing medium, equation 6.4, is considered. The absorption coefficient domain is then divided into m ranges, bounded by k_{j+1} and k_j with $k_{j+1} > k_j$. A characteristic absorption coefficient value within each range is defined, namely $k_j^* = (k_j k_{j+1})^{1/2}$, with $1 \leq j \leq m$. For each absorption coefficient range j, an associated wavenumber range $\Delta\eta_j$ is naturally defined, such that for each η in $\Delta\eta_j$, the actual absorption coefficient κ_η lies in the range $[k_j, k_{j+1}]$. Thus, the whole spectrum is divided in m non overlapping bands, in which the absorption coefficient is assumed to be the constant k_j^*. In order to include the spectral ranges where the gas is transparent, it is assumed that $k_0^* = k_0 = 0$.

An integration of equation 6.4 over all of the wavenumber ranges is carried out, for each absorption coefficient range j. After some manipulation, detailed in section 4.2.2, the RTE acquires the form

$$\mu \frac{\partial I_j}{\partial x} + \xi \frac{\partial I_j}{\partial y} = -k_j^* (I_j - a_j I_b), \tag{6.6}$$

where a_j is a weight sensible to the particular wavenumber dependence of the absorption coefficient of the media under consideration. The integrated intensity over the whole spectrum, in this model, is simply $I = \sum_j I_j$. The validity of this model is investigated in section 4.4.

In order to be able to calculate the above mentioned weight a_j (and in some cases also k_j^*), and to calculate the corresponding local characteristic absorption coefficient k_j^*, it is common to define a so called blackbody distribution function, F, as the integral of the blackbody intensity for all wavenumbers for which the absorption coefficient is below a prescribed value:

$$F(T_b, \bar{\xi}, k) = \frac{1}{I_b(T_b)} \int_{\kappa_\eta(\bar{\xi})<k} I_{b\eta}(T_b)\, d\eta. \tag{6.7}$$

In the above expression, the set $\bar{\xi}$ contains all the variables that the absorption coefficient may depend on: temperature, pressure, species concentration…The detailed dependence of the absorption coefficient on the wavenumber is needed to compute the function F.

There are two ways to obtain these distribution functions. First of all, there exist correlations in the literature for the computation of the function F for CO_2 [15,16,17] and for H_2O [18], obtained from a least squares fitting procedure. On the other hand, these distribution functions can be directly calculated from detailed absorption line data (see page 75 for more details). In this chapter, the latest version of the CDSD-1000 [19] and HITEMP [20] databases are used for the distribution functions for CO_2 and H_2O respectively. These functions have been calculated at several temperatures and concentrations (in the case of H_2O), as outlined in a work by Mazumder and Modest [21]. The distribution function at local conditions is then obtained by linear interpolation. Once the distribution function is known, it can be used to different levels of detail.

High resolution partition. In this case, two suitable values are used as lower and upper bounds of the absorption coefficient domain partition, namely k_1 and k_m. The absorption coefficient boundaries k_j are logarithmically equidistant, i. e., $k_j = k_1(k_m/k_1)^{(j-1)/(m-1)}$, for $1 \leq j \leq m$. Then, the coefficient a_j in equation 6.6 is easily obtained as the difference $a_j = F(k_{j+1}) - F(k_j)$. It can be easily seen that the sum of all the weights a_j equals one if the appropriate absorption coefficient ranges are selected, that is, if $F(k_m) = 1$ and $F(k_1) = 0$. The mean absorption coefficient is $k_j^* = (k_j k_{j+1})^{1/2}$.

Using optimized coefficients. An alternative way of defining the weights a_j and the mean absorption coefficients k_j^* is by means of an optimization procedure [3]. The details can be found in page 76. For the absorption cross section domain partition using optimized coefficients, fitted distribution functions are used: the correlation given by Modest and Mehta [16] for CO_2, and the correlation given by Denison and Webb [18] for H_2O.

Gray absorption coefficient. A wavenumber averaged absorption coefficient for the mixture of the two species can be inferred with the aid of the SLW model. This averaged absorption coefficient, κ_P (Planck mean absorption coefficient), is calculated independently for the participating species CO_2 and H_2O, as

$$\kappa_P = \frac{1}{I_b} \int_\eta \kappa_\eta I_{b\eta}\, d\eta \simeq \sum_j \left\{ F(k_{j+1}) - F(k_j) \right\} k_j^*, \tag{6.8}$$

which depends also on the temperature. The Planck mean absorption coefficient has been computed using the F distribution functions (equation 6.7) obtained from the latest HITRAN and HITEMP databases [20] for CO_2 and H_2O respectively, and $k_1 = 10^{-8} cm^{-1}$ and $k_m = 200 cm^{-1}$. The κ_P of the mixture is computed as the sum of the individual absorption coefficients, weighted by the molar fraction of each species [21]. The use of the Planck mean absorption coefficient yields faster calculations, although simplifying the non gray behavior of the radiant gas.

6.2.4 Dimensionless describing parameters

In order to describe the flow, the normal approach is to use a set of dimensionless governing numbers (the Rayleigh number, the Prandtl number, and so on…). In this chapter we characterize the flow by using the time scale concept, which arises from the fact that, when trying to write the dimensionless form of the governing equations, several combinations of the relevant magnitudes have dimensions of time. Therefore, there are several choices for the time scale, each one associated with a different dominating mode of energy transfer. A rough approximation of such scales will help both on characterize the solution and choose an optimal time step when numerically solving the coupled equations 6.1, 6.2, and 6.3.

We can think of a *conduction time scale*, which will be the time that takes a medium to reach thermal equilibrium with its environment by means of heat conduction. Under the simplest conditions, such time is

$$\tau_c = \frac{\rho c_p L^2}{k}. \tag{6.9}$$

Notice that this particular time scale does not depend on neither initial nor final temperature. The explanation seems to be that the conductive heat transfer depends only on linear differences of temperature.

If we think of a medium with temperature depending density, then convective energy transport will take place, and so a *buoyancy time scale* can be defined. We consider this scale to be the time that takes a bubble of hot fluid to move upwards in a colder, isothermal fluid. Assuming that the temperature of the bubble remains constant, such time is

$$\tau_b = \sqrt{\frac{L}{g\beta\Delta T}}, \tag{6.10}$$

where ΔT stands for the difference between the maximal and minimal temperatures, and β for the thermal expansion coefficient.

At high temperatures, radiation becomes an important mode of energy transfer, and thus we can define a *radiation time scale*. Considering now the energy equation with the divergence of $\mathbf{q}_r$ as the only source, and a volume of hot gas of length L and behaving like a black body, the time for that volume to reach thermal equilibrium with the surrounding medium is given by

$$\tau_r = \frac{\rho c_p L \Delta T}{\sigma_B T_0^4}, \tag{6.11}$$

being L a suitable volume/surface ratio and ΔT the difference between initial and final temperatures. This time scale is roughly the energy that is to be extracted to the volume of gas to vary its temperature in an amount of ΔT divided by the power emission of the gas.

The viscosity, which is responsible of generating a velocity gradient in the flow —from non-slip boundary condition to the velocity of the fluid far of any boundary, may be thought as a diffusion coefficient of the velocity and acts in its own *viscous time scale*. If viscosity is dominant, then the momentum equation becomes a diffusion equation on velocity analogous to the conduction equation, with a diffusion coefficient of μ/ρ. The time needed to establish the gradient at a distance L from the boundary is then

$$\tau_v = \frac{\rho L^2}{\mu}, \tag{6.12}$$

obtained by replacing the diffusion coefficient by μ/ρ in the conduction time scale.

If the Navier-Stokes equations are written in dimensionless form, as in section C.3, each source term, except the pressure gradient term, is weighted by a ratio of time scales (for instance the divergence of radiative heat term in the energy equation is weighted by τ_α/τ_r, where τ_α is the time scale chosen as a reference). Thus, a simple estimate of the relative importance of the source terms is easily obtained. The shortest time scale induces the behavior of the fluid flow. For example, if τ_c is the fastest time, the solution will be conduction dominated (nearly vertical isothermal lines), while if the fastest scale is τ_b, the solution will be convection dominated, that is, with near horizontal isothermal lines.

The time scales discussed above are related in a very simple way to the more commonly used dimensionless numbers to completely characterize the flow. In the case we have solved, the relevant numbers are the Prandtl number Pr, the Rayleigh number Ra, the Planck number Pl and the temperature ratio $\phi = \Delta T/T_{\text{cold}}$. It turns out that the relation between the dimensionless numbers and the time scales is

$$Ra = \frac{\tau_c \tau_v}{\tau_b^2}; \qquad Pr = \frac{\tau_c}{\tau_v}; \qquad Pl = \phi \frac{\tau_r}{\tau_c}. \tag{6.13}$$

6.3 Numerical method

The discretization of the Navier-Stokes equations is carried out using fully implicit finite volume techniques on cartesian staggered grids. To account for the velocity-pressure coupling, the SIMPLEC procedure is adopted. The interpolation numerical scheme was the simplest, upwind like, in order to facilitate the convergence, which is affected by the high non linearity of the radiative source term $\boldsymbol{\nabla} \cdot \mathbf{q}_r$. The mesh was concentrated near the walls, by means of an hyperbolic tangent function.

The radiation source term is calculated by solving equation 6.4, and integrating for all the spectrum by using the SLW model. The radiative transfer equation, RTE, is solved for a discrete set of directions $\{\mu_i, \xi_i\}$, following the Discrete Ordinates Method (DOM). The finite volume technique is used to discretize the spatial part of the RTE, and an explicit, step by step procedure, is employed to determine the intensity radiation field. The discretization details can be found in chapter 3. Orthogonal meshes have been used to solve the RTE. The angular quadrature set employed was the T_n by Thurgood et al. [22].

With respect to the numerical parameters of the SLW method, the high resolution absorption cross section partition consists of $m = 11$ cross sections, while the optimized coefficients strategy consists of $m' = 5$ cross sections, both including the transparent band. For the high resolution case, the integration interval k_1 is set to $3 \times 10^{-5} cm^{-1}$ and k_{10} is set to $600 cm^{-1}$ for CO_2 and to $60 cm^{-1}$ for H_2O, following the suggestions given in [15, 18].

The influence of different databases on the optical properties of CO_2 and H_2O is analyzed by calculating the total emissivity from Denison and Webb correlations [15, 18], which are fairly outdated. The total emissivity is calculated at a reference temperature T_{ref}; the resulting coefficients from the fitting process to be used in the SLW model are shown in table 6.1. These coefficients are referred to as optimized coefficients.

CO_2		H_2O	
k_j^*	a_j	k_j^*	a_j
$2.123118e-01$	$1.557237e-01$	$2.188490e-01$	$2.888546e-01$
$2.615123e+00$	$9.144159e-02$	$1.952972e+00$	$2.157405e-01$
$2.803898e+01$	$6.119854e-02$	$1.378076e+01$	$1.497009e-01$
$4.652916e+02$	$2.902018e-02$	$1.273570e+02$	$5.291578e-02$

Table 6.1: Optimized coefficients obtained by fitting total emissivity data to equation 4.16, with $L = 10m$ and $T_{\text{ref}} = 600K$.

Independently of what coefficients a_j, k_j^*, for the individual participating species are used, the mixture is treated as a single gas. The equivalent coefficients for the

SLW model are found from the individual coefficients as $a_{i,j} = a_{i,\mathrm{CO_2}} a_{j,\mathrm{H_2O}}$ and $k^*_{i,j} = k^*_{i,\mathrm{CO_2}} + k^*_{j,\mathrm{H_2O}}$ [23, 24]. It turns out, then, that the RTE has to be solved m^2 (or m'^2) times. This fact explains the interest on decreasing the number of cross sections considered, thus reducing the number of operations to perform. However, the use of mathematical correlations for the optimized coefficients case, instead of interpolated data, increases the computation time, and the solutions with and without optimized coefficients are obtained within the same time (in fact, the calculation using optimized coefficients takes more time to complete).

6.4 Problem description and research approach

We have selected a two dimensional differential heated cavity, homogeneously filled with a gas mixture consisting of N_2, CO_2, and H_2O, with a mass fraction of 0.7, 0.1, and 0.2 respectively, in order to evaluate the influence of the way in which the SLW model parameters of the participating species are calculated. The flow is driven by natural convection, when gravity is different from zero. The vertical walls are kept at $300K$ and $600K$, while the horizontal walls are insulated. All surfaces are black and N_2 is considered not to participate on the radiative exchange. A scheme of the solved problem is depicted on figure 6.1. The length of the sides of the square cavity is L. Although it makes not much sense to talk about dimensionless governing numbers or time scales if thermal properties are thought as temperature functions, it will help to describe the fluid, and therefore all the time scales, and hence the dimensionless numbers, are calculated with termal properties evaluated at a reference temperature $T_0 = (T_{\mathrm{cold}} + T_{\mathrm{hot}})/2$.

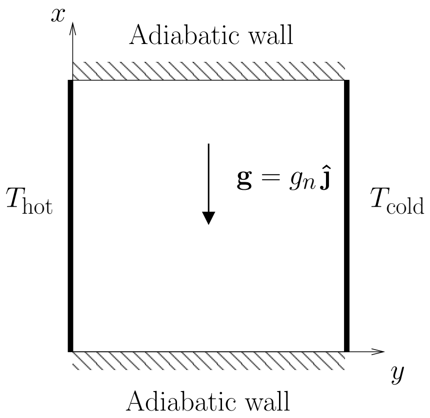

Figure 6.1: Scheme of the solved thermal driven cavity.

The posed problem is solved with four radiation approaches: (i) transparent medium, (ii) gray medium, (iii) non gray medium using the SLW model with optimized coefficients, and (iv) non gray medium using the SLW model with high resolution absorption coefficient domain partition. In the first case, only radiation energy exchange between surfaces is considered, i. e., the gas mixture is assumed to be non participating ($\kappa_\eta = 0$). In the second case, the mixture is assumed to be participating, but with a gray absorption coefficient. For this situation, the absorption coefficient κ_P is obtained as explained in section 6.2.3. Both these solutions are some 30 or more times faster than the detailed spectral models. To overcome the simplifications involved in the two above models, full spectral calculations are performed by means of the SLW model, by using both a high resolution partition of the absorption coefficient domain, section 6.2.3, and optimized coefficients, section 6.2.3. Although the goal of this chapter is to study coupled convection and non gray radiation, gray radiation calculations are carried out in order to compare them to non gray calculations, and to judge if the differences between these two approaches are significant enough to justify the use of non gray models.

The problem is solved for a range of the previously defined time scales, first by varying the convective contribution (radiation vs. convection heat transfer), and second by considering two additional cavity sizes, one which is radiation dominated and other where radiation and conduction are roughly equally significant (radiation vs. conduction heat transfer).

6.4.1 Radiation vs. convection heat transfer

In a first step, the problem is solved keeping the time scales constant except for τ_b, the buoyancy scale, which varies in order to represent different ammount of contributions of the convective energy transfer to the total. These different values of τ_b are achieved by varying the gravity strength, that is, by setting $g_n = 2^{n-1}/800ms^{-2}$, $n \geq 1$, and $g_0 = 0$. The values of the fixed time scales, in units of τ_r, are $\tau_c = 41$ and $\tau_v = 57.6$, meaning that radiation heat transfer dominates over heat conduction. The commonly used corresponding dimensionless numbers to these time scales are $Pr = 0.711$ (near to that of the air), $Pl = 0.024$, and $\phi = 1$. The relevant dimensionless parameters for the solved cases are summarized in table 6.2. It is clear from this table that all problems solved with the fixed length $L_0 = 1m$ configuration are convection dominated (except for the g_0 case, which is radiation dominated).

6.4.2 Radiation vs. conduction heat transfer

Since all the time scales depend on the size of the domain L, other solved configurations include smaller cavities, with lengths $L_1 = 0.025m$ and $L_2 = 0.4m$, in order to take into account situations where the relevance of radiation respect to conduction contribution varies. In these cases, gravity was set to zero, and the only dimensionless numbers that are kept constant are the Prandtl number, $Pr = 0.711$, and the temperature ratio, $\phi = 1$. Table 6.2 shows that, for the small cavities, an appreciable difference on the ratios of time scales is observed, meaning that rather different behavior is expected: the L_1 case is, in principle, dominated by radiation and conduction equally, while the L_2 case is clearly radiation dominated.

Convection dominated ($L_0 = 1m$) $Pl = 0.024$, $\phi = 1$, $Pr = 0.711$				
	g_0	g_1	g_5	g_9
τ_b/τ_r	∞	0.059	0.015	0.0037
$Ra/10^6$	0	0.686	10.98	175

Conduction and radiation heat transfer $Ra = 0$, $\phi = 1$, $Pr = 0.711$		
	L_1	L_2
τ_c/τ_r	1.02	16.4
Pl	0.976	0.061

Table 6.2: Values of the non dimensional relevant parameters for the different configurations. First, the buoyancy time scale and Rayleigh number for the different values of gravity field are shown. In all cases with $g \neq 0$ the convection time scale is the fastest. Last, conduction time scale and Planck number are shown for the different cavity lengths $L_1 = 0.025m$ and $L_2 = 0.4m$.

The time scales introduced in section 6.2.4 give an idea of which discrete time increment should be used while solving the coupled equations: it has been found that the best choice is few times (say 2) the shortest time scale. If a bigger time step is selected, some physics is missing and sometimes convergence is not achieved; on the other hand, a much smaller discrete time step will lead to an unnecessary high number of iterations (and thus higher calculation time). For the calculations carried out in this chapter, the discrete time step was set to a conservative 1.5 times the minimum of $\{\tau_c, \tau_b, \tau_r, \tau_v\}$.

6.5 Illustrative results

6.5.1 Verification of the numerical solutions

All the cases presented hereinafter were solved using three levels of refinement, that is, three grids of 16^2, 32^2, and 64^2 control volumes. These grids are concentrated near the walls in order to avoid excessive temperature steps imposed by the boundary conditions. With this information available, it is possible to estimate the error between the finest mesh and the grid independant solution, following the work by

Cadafalch et al. [25]. By using the Richardson extrapolation technique for the several cases for the finest, 64^2 control volume mesh, the mean uncertainity due to discretization is estimated to be, on average (without significant deviations), $\pm 0.5K$ for the temperature field, and about $\pm 0.3\%$, in average, with respect to the maximum value of the divergence of radiative heat field, although for the g_5 case this uncertainity peaks to $\pm 1.1\%$. These figures are assumed to be representative for all the cases, and hence the 64^2 mesh is considered as fine enough to perform the numerical experiments reported in this work.

6.5.2 Radiation vs. convection heat transfer

The effect of the model of the absorption coefficient of the participating gases is hereinafter analyzed. The same problem is solved for several values of the gravity acceleration, in order to inspect a range of qualitative different solutions, i. e., where radiation heat transfer looses significance with respect to convective heat transfer as the strength of gravity increases. It is possible to achieve this since the gravity appears only in the buoyancy time scale (equation 6.10), thus affecting only the convective contribution. Figures 6.2 and 6.3 present the temperature profile in x direction at the middle of the cavity ($y = 0.5m$). The solution given by SLW and SLW with optimized coefficients are in good agreement, despite the absorption coefficient is calculated in a rather different way for each case. Gray medium (results calculated using the Planck coefficient) and transparent medium (only heat exchange between surfaces) differs notably from the non gray solution, although for increasing gravity strength, the temperature profiles tend to converge, specially for the g_9 case.

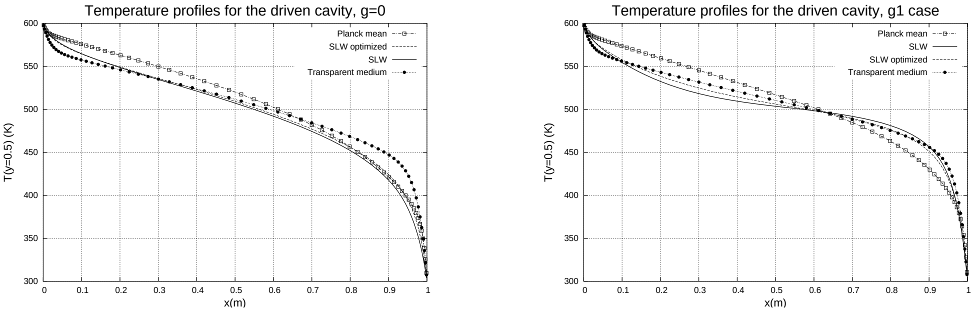

Figure 6.2: Left: temperature profile at $y = 0.5m$, for all optical models considered. Radiation dominated case, $g = 0$. Right: same as left, with g_1.

This trend is reversed if we look at the velocity field. By decreasing the buoyancy time scale, the differences on the velocity profiles increase, as it is apparent in figure 6.4. Transparent media, approach (i), performs quite well for the $g = 0$

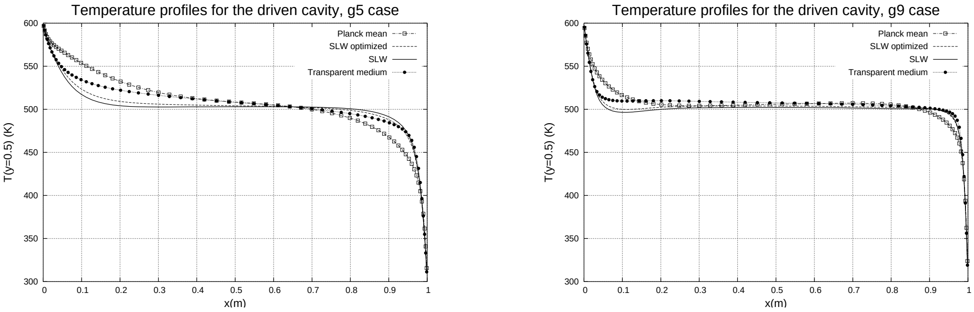

Figure 6.3: Left: temperature profile at $y = 0.5m$, for all optical models considered, with g_5. Right: same as left, with g_9.

case. The high value of ϕ we use implies that radiation has a noticeable effect on the flow. Therefore, the influence of the absorption coefficient model on the velocity field should be bigger for larger velocities, i. e., strongest gravity field. If forced convection were considered instead of natural convection, we do not expect the effect of the radiation model on the velocity field to be so relevant.

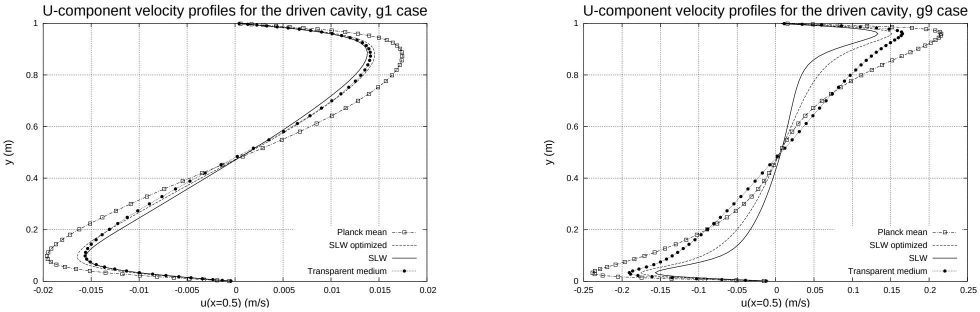

Figure 6.4: Left: Profile of the horizontal component of the velocity at $x = 0.5m$, for all the optical models considered, g_1 case. Right: same as left, g_9 case. The difference between the SLW and the other models is larger in this situation.

It is interesting to note that it seems that the transparent medium assumption it is preferable to the participating, gray medium assumption, using the Planck coefficient. This is due to the fact that the transparent band of the CO_2 alone contributes in more than a 50% of the total weighting coefficient $a_{i,j}$ (see section 6.3), i. e., $\sum_j a_{0,j} > 0.5$.

In figure 6.5, isotherms and streamlines are plotted for the two extreme cases solved, namely g_1 and g_9. The effect of radiation heat transfer in the flow structure, reported for instance by Yücel et al. [26], is apparent: the flow circulates clockwise around the cavity center. For the stronger gravity field considered, the temperature is near homogeneous, instead of the stratified temperature field observed when radiation is not taken into account. Both effects are due to the high temperature ratio $\phi = 1$ assumed. Notice that, although the Rayleigh number for the g_1 case is high according to table 6.2, the flow is not as stratified as one would expect. This can be attributed to the fact that the buoyancy time scale is not much faster than the radiation time scale. If radiation were not considered, the convection time scale would dominate (being the dimensionless numbers and time scales the same of the radiation case), and the flow would be homogeneously stratified.

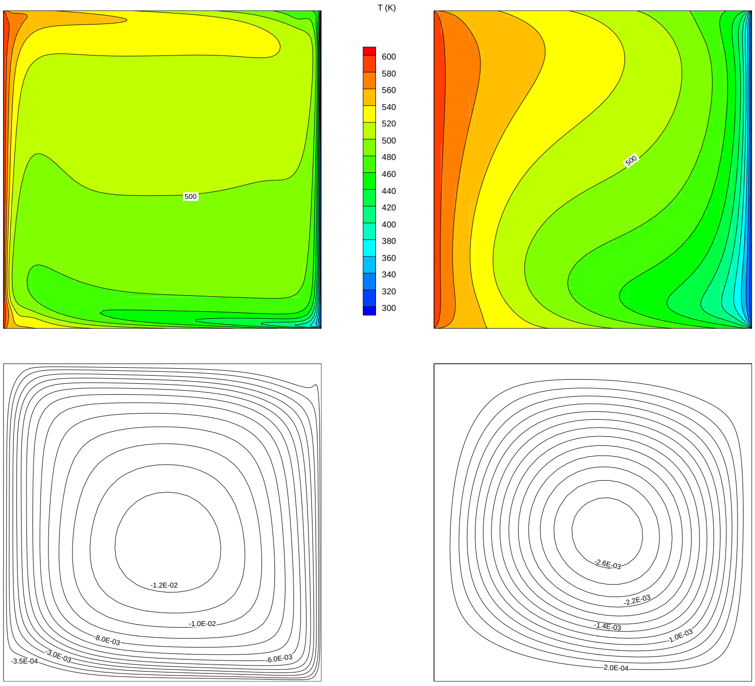

Figure 6.5: Left: isotherms (up) and streamlines (down) for the g_9 case, using the SLW approach (iv). Right: same as left, for the g_1 case.

While middle cavity temperature profiles are relatively similar for all models for the strongest gravity considered, the differences in hot wall total heat flux are more apparent. Results for the total heat flux through the hot wall are presented in table 6.3.

	g_0	g_1	g_5	g_9
Transparent (i)	291.1	294.0	312.0	341.6
Planck mean (ii)	106.5	114.1	163.9	239.7
SLW optimized (iii)	325.5	331.2	349.9	377.9
SLW (iv)	348.1	354.2	369.9	394.4

Table 6.3: Non dimensional heat flux through hot wall: the non dimensional factor is the conductive heat flux, $k_0 \Delta T / L$.

The difference between the non-gray radiation models is studied, by means of the integral of the deviation σ, with

$$\sigma^2(T) = \frac{1}{V} \int_V \left(T_{\text{app.}} - T_{\text{SLW}} \right)^2 dV, \tag{6.14}$$

where T_{SLW} refers to approach (iv), SLW with high resolution partition of the absorption coefficient domain, and $T_{\text{app.}}$ refers to any of the other approaches. Analogous indicators are used for the velocity components, u and v. These magnitudes are tabulated in table 6.4. The increasing velocity deviation trend is clear for the three approaches (i), (ii), and (iii). The temperature deviation seems to decrease, irregularly, for increasing g, except when the Planck mean absorption coefficient is used. As expected, table 6.4 shows that the smallest deviation occurs indeed when approach (iii) is employed. Notice that, according to this table, the velocity fields for the $g1$ case, in approaches (i) and (iii), are expected to be similar. This is clearly seen in figure 6.4 (left).

	$\sigma(T)/T_0(\%)$	$\sigma(u)/\lvert u_{\max}\rvert(\%)$	$\sigma(v)/\lvert v_{\max}\rvert(\%)$
g_0	0.65/2.67/2.57	—	—
g_1	0.91/3.92/2.53	3.18/13.6/3.38	3.25/14.0/3.55
g_5	0.72/4.39/1.92	5.74/24.8/13.1	5.89/25.8/13.6
g_9	0.50/3.35/1.57	6.81/27.2/18.0	6.22/25.3/16.4

Table 6.4: Deviation of the different models from the SLW solution. Each triplet represents the deviation of the SLW with optimized coeffcients, the Planck assumption, and the transparent gas behavior solutions respectively.

6.5.3 Radiation vs. conduction heat transfer

The different dependance of the time scales with the cavity length allows us to select a range of lengths in which the ratio between radiation and conduction time scale varies in a large amount. If the length is short enough, conduction time scale will become the fastest one, and consequently the heat transfer will be conduction dominated. The effect of the optical model is plotted in figure 6.6, for two different lengths. It is clear that, for the L_1 case, the transparent approximation is preferable than the Planck mean model, while for the bigger, L_2 cavity, the difference between the models clearly shows up. This is because the optical depth of the mixture is proportional to the cavity size, and thus, the transparent behavior is more evident for the smaller enclosure.

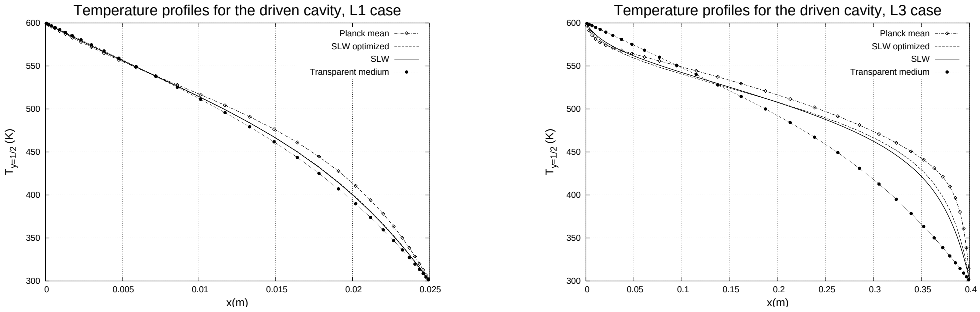

Figure 6.6: Left: temperature profile at $y/L = 0.5$, for all the optical models considered. Small cavity $L_1 = 0.025m$. Right: same as left, for a bigger cavity $L_2 = 0.4m$.

In figure 6.7, the temperature profiles for different cavity sizes, obtained using the high resolution SLW method, approach (iv), are plotted, and compared to the profile obtained when radiation is neglected. As we can expect from table 6.2, for the smallest cavity, in addition that all radiation models tend to the transparent behavior, the results obtained are also close to the purely conduction case, because of the relative significance of radiation and conduction time scales. The L_0 and L_2 cavities exhibit a very similar temperature profile, meaning that for cavity lengths larger than L_2, radiation transfer dominates over heat conduction.

6.6 Conclusions

Several absorption coefficient approaches using the SLW model have been taken into account, in order to consider the effect of non gray radiative heat transfer in a participating medium on a thermal driven cavity problem. The use of any of the non gray methods is justified since neither the gray gas nor the transparent model captures well the real gas behavior. The optimized coefficients approach (iii) yields results very close to those from the high resolution approach (iv), except for the velocity field for the strongest gravity considered. The use of optimized coefficients

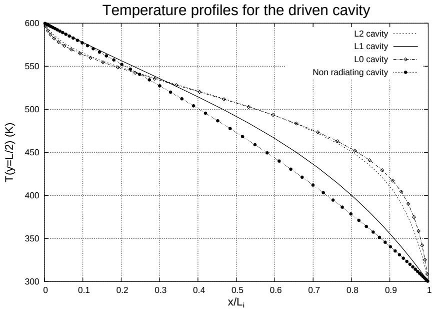

Figure 6.7: Temperature profile for different size enclosures. Except for the non radiating case, the temperature profiles are obtained with the high resolution SLW method. $L_0 = 1m$, $L_1 = 0.025m$, and $L_2 = 0.4m$.

is therefore recommended, in order to reduce the number of calculations to perform. Further tests, considering mixed or forced convection, should be done to check the performance of approach (iii) in these cases. In all cases solved, the Planck mean approximation gives the worse results compared to non gray models. This fact can be seen in temperature profile plots, in the velocity profile plots, in the total heat flux table, and in the deviation with respect to approach (iv) table.

It has been observed that, increasing the convection contribution (by decreasing the associated time scale τ_b), the effects of the radiation approach become less significant to determine the temperature field and the total heat flux through the isothermal walls. In these cases, the transparent media approximation seems to offer a good result, both in temperature profiles and total heat flux, and is clearly preferable to the gray gas assumption, albeit being the crudest, cheapest (computationally speaking), model.

On the other hand, increasing the gravity strength, the differences on the velocity field with respect to the high resolution SLW solution tend to increase. This can be attributed to the fact that the temperature ratio is high ($\phi = 1$), meaning that the flow structure is largely affected by radiation, and also to the fact that the velocity field itself is larger, thus magnifying the differences between the different strategies employed.

It has also been checked that, for small enclosures, the choice of the radiation approach has less impact on the outcome, because the participaing gases are nearly transparent. For larger enclosures, heat conduction, whose time scale grows with the square of the cavity size, plays no significant role on the energy transfer. The above mentioned time scales are good parameters to describe what kind of flow is expected, in addition to provide a natural choice of the discrete time step when solving the Navier-Stokes equations.

References

[1] Michael F. Modest. The Weighted-Sum-of-Gray-Gases Model for Arbitrary Solution Methods in Radiative Transfer. *Journal of Heat Transfer*, 113:650–656, August 1991.

[2] Laurent Pierrot, Philippe Rivière, Anouar Soufiani, and Jean Taine. A fictious-gas-based absorption distribution function global model for radiative transfer in hot gases. *J. Quant. Spectrosc. Radiat. Transfer*, 62:609–624, 1999.

[3] M. K. Denison and Brent W. Webb. A spectral line based weighted sum of gray gases model for arbitrary RTE solvers. *Journal of Heat Transfer*, 115(4):1004–1012, November 1993.

[4] Fengshan Liu, Gregory J. Smallwood, and Ömer L. Gülder. Application of the statistical narrow band correlated-*k* method to low-resolution spectral intensity and radiative heat transfer calculations — effects of the quadrature scheme. *Int. J. Heat and Mass Transfer*, 43(17):3119–3135, 2000.

[5] Claudio Mesyngier and Bakhtier Farouk. Turbulent natural convection - nongray gas radiation analysis in a square enclosure. *Numerical Heat Transfer, Part A*, 29:671–687, 1996.

[6] Anouar Soufiani and E. Djavdan. A comparison between weighted sum of gray gases and statistical narrow band radiation models for combustion applications. *Combustion and Flame*, 97(2):240–250, 1994.

[7] P. J. Coelho, O. J. Teerling, and D. Roekaerts. Spectral radiative effects and turbulence/radiation interaction in a non-luminous turbulent jet diffusion flame. *Combustion and Flame*, 133(1–2):75–91, 2003.

[8] EzEddine Sediki, Anouar Soufiani, and Mohamed Salah Sifaoui. Combined gas radiation and laminar mixed convection in vertical circular tubes. *Int. J. Heat and Fluid Flow*, 24(5):736–746, 2003.

[9] Fengshan Liu, Hongsheng Guo, Gregory J. Smallwood, and Ömer L. Gülder. Numerical modelling of soot formation and oxidation in laminar coflow non-smoking and smoking ethylene diffusion flames. *Combust. Theory Modelling*, 7(2):301–315, 2003.

[10] Fengshan Liu, Hongsheng Guo, and Gregory J. Smallwood. Effects of radiation model on the modeling of a laminar coflow methane/air diffusion flame. *Combustion and Flame*, 138:136–154, 2004.

[11] P. J. Coelho. Detailed numerical simulation of radiative transfer in a nonluminous turbulent jet diffusion flame. *Combustion and Flame*, 136(4):481–492, 2004.

[12] EzEddine Sediki, Anouar Soufiani, and Mohamed Salah Sifaoui. Spectrally correlated radiation and laminar forced convection in the entrance region of a circular duct. *Int. J. Heat and Mass Transfer*, 45(25):5069–5081, 2002.

[13] David Lacroix, Nacer Berour, Pascal Boulet, and Gérard Jeandel. Radiative and conductive heat transfer in a nongrey semitransparent medium. Application to fire protection curtains. *J. Quant. Spectrosc. Radiat. Transfer*, 86(1):9–30, 2004.

[14] K. Claramunt, R. Cònsul, C.D. Pérez-Segarra, and A. Oliva. Multidimensional mathematical modeling and numerical investigation of co-flow partially premixed methane/air laminar flames. *Combustion and Flame*, 137:444–457, 2004.

[15] M. K. Denison and Brent W. Webb. Development and application of an absorption-line blackbody distribution function for CO_2. *Int. J. Heat and Mass Transfer*, 38(10):1813–1821, 1995.

[16] Michael F. Modest and Ranjan S. Mehta. Full spectrum k-distribution correlatons for CO_2 from the CDSD-1000 spectroscopic database. *Int. J. Heat and Mass Transfer*, 47(10–11):2487–2491, 2004.

[17] Hongmei Zhang and Michael F. Modest. Full-spectrum k-distribution correlations for carbon dioxide mixtures. *Journal of Thermophysics and Heat Transfer*, 17(2):259–263, 2003.

[18] M. K. Denison and Brent W. Webb. An absorption-line blackbody distribution function for efficient calculation of total gas radiative transfer. *J. Quant. Spectrosc. Radiat. Transfer*, 50(5):499–510, 1993.

[19] S. A. Tashkun, V. I. Perevalov, J-L. Teffo, A. D. Bykov, and N. N. Lavrentieva. CDSD-1000, the high-temperature carbon dioxide spectroscopic databank. *J. Quant. Spectrosc. Radiat. Transfer*, 82:165–196, 2003.

[20] L. S. Rothman et al. The HITRAN 2004 molecular spectroscopic databased. *J. Quant. Spectrosc. Radiat. Transfer*, 96(2):139–204, 2005.

[21] Sandip Mazumder and Michael F. Modest. Application of the Full Spectrum Correlated-k Distribution Approach to Modeling Non-Gray Radiation in Combustion Gases. *Combustion and Flame*, 129(4):416–438, 2002.

[22] C. P. Thurgood, A. Pollard, and H. A. Becker. The T_n quadrature set for the discrete ordinates method. *Journal of Heat Transfer*, 117:1068–1070, November 1995.

[23] M. K. Denison and Brent W. Webb. The spectral line weighted sum of gray gases model for H_2O/CO_2 mixtures. *Journal of Heat Transfer*, 117(3):788–792, 1995.

[24] Laurent Pierrot, Anouar Soufiani, and Jean Taine. Accuracy of narrow-band and global models for radiative transfer in H_2O, CO_2, and $H_2O - CO_2$ mixtures at high temperature. *J. Quant. Spectrosc. Radiat. Transfer*, 62(5):523–548, 1999.

[25] J. Cadafalch, C.D. Pérez-Segarra, R. Cònsul, and A. Oliva. Verification of finite volume computations on steady state fluid flow and heat transfer. *Journal of Fluids Engineering*, 124:11–21, 2002.

[26] A. Yücel, S. Acharya, and M. L. Williams. Natural convection and radiation in a square enclosure. *Numerical Heat Transfer, Part A*, 15:261–278, 1989.

7

Epilogue

7.1 Concluding remarks

The main objective of the present thesis is to analyze heat transfer due to radiation. The integro-differential nature of the radiative transfer equation, forces this thesis to be directed towards the numerical methods to account for radiation transfer. This is one of the first works within the scope of the CTTC which deals with radiation heat transfer in the most general manner possible. Therefore, special care has ben taken to properly introduce the radiative transfer equation, as well as all the related concepts and magnitudes, in chapter 1.

As a wetting feet approach to radiation transfer, my first task was to develop a procedure to calculate the view factors for cylindrical geometries, with axial symmetry, to be used with the RIM method. Internal obstacles can also be handled. The results are summarized in chapter 2. Although a little disconnected from the rest of the present thesis, the algorithm to handle "de facto" three dimensional geometries with computation time just a little longer than two dimensional cases, with no additional memory consumption, is considered worthy enough to be included in this work. As it is clear from the presented results, the major source of error of this method is the presence of internal solids, which causes the view factors not to be correctly evaluated; in particular, equation 2.5 does not hold. Best results are obtained with the simplest geometries, i. e., without internal obstacles.

In chapter 3, the DOM is applied, along with the finite volume method, to discretize and integrate the radiative transfer equation. The basic properties of the ordinate sets, central to the DOM, are described, and numerical error sources are discussed as well. Results obtained with this method, considering transparent and participating media, are presented at the end of this chapter. Inhomogeneous, two and three dimensional, cartesian and cylindrical geometries are considered. Usually, radiation heat transfer calculations are carried out with a given temperature field, but when radiation is the dominant mode of energy transfer, it is possible to calculate the temperature by means of equation 1.20. Two cases where the energy equation is solved are presented, one representing a cubic cavity and the other representing a cylindrical furnace. Also, the ray effect present for any given grid is shown in figure 3.11. The results have been compared with other metods, as well as to analytical solutions when available; these later results are in good agreement with the results obtained using the tools created when elaborating this thesis.

An important remark it must be done is that, in order to exploit the symmetries of axial symmetric cylindrical geometries, the formulation of the DOM becomes rather involved. For other non cartesian coordinate systems, similar problems will arise. The reason for this is that we are assuming that the photons propagate along straight lines, and in curved coordinates the propagation direction is continuously changing, so there appear additional derivatives with respect the direction we are solving.

It is worth noting that, while the RIM requires a transparent medium, the DOM does not. That is, both RIM and DOM can solve radiative heat exchange between surfaces. However, if the geometry is not too complicated, the RIM advantages the DOM in terms of computational speed and memory requirements; therefore the RIM is a valuable alternative in such cases.

The radiative properties of real gases have been studied in chapter 4. The main issue concerning the radiative properties is its strong dependence on the wavenumber. Thus, there is a clear interest to take into account such dependence. This interest resulted on a bibliographical research on how these radiative properties, especially the absorption coefficient, are modeled and estimated. It turns out that the better model of the absorption coefficient is obtained through huge, publicly available databases, which hold data of thousands of absorption lines from which the absorption coefficient may be calculated. Furthermore, this bibliographical research was focussed also on numerical models capable of handle such wavenumber dependence. It was found that non gray models can be classified, mainly, into full spectrum models and band models. The former are suitable for combined heat transfer problems, which are the main objective of this thesis. The later are more reliable, although require much more computational effort. Therefore, only the full spectrum models have been considered in this work.

The results in this chapter show that the implementation of the WSGG method and the SLW method is in good agreement with benchmarked solutions given by other authors. Although the SLW method is more computationally demanding, it is a better choice than the WSGG method: its accuracy for homogeneous media can be increased without limitation, and non homogeneous media can be taken into account (which is not possible with the WSGG metod). Moreover, results of sections 4.4.5 and 4.4.6 show that the performance of the SLW method can be improved, tending to that of the WSGG method, with little loss of accuracy.

Chapter 5 is devoted to combined heat transfer in a gray medium. The results obtained show that radiation and convection are somewhat independent, in the sense that, under the conditions considered, radiative contribution almost does not depend on the Rayleigh number, while convection contribution is highly affected by it. The optical thickness of the medium also affects heat transfer between the isothermal walls; higher optical thickness results in lower heat transfer.

Chapter 6 deals with combined heat transfer within a non gray gas mixture. Results show that, as far as combined heat transfer is considered, a wise selection of the parameters of the SLW model will reduce the computational cost of the solutions, with little loss of accuracy. On the other hand, the same results seem to point out that, in some cases, the transparent medium assumption is more reliable than the non gray assumption, for mixtures containing CO_2.

The contributions of this thesis are mainly valuable to the group within it has been developped. This work covers both physical description of radiation transfer and several numerical approaches. Therefore, the major achievement has been the knowledge acquired on radiative heat transfer, especially when participating media are concerned. All this accumulated experience will be indeed useful when complex problems, where radiation could not be neglected, are to be solved. In addition, the radiation specific computer code, resulting from the elaboration of this thesis, has been succesfully integrated to a wider, general purpose, computational fluid dynamics code (DPC), fruit of the effort of many researchers during many years. The results of this integration lead to the publication of an article [1] (chapter 5), and the submission of another article (chapter 6). The fact that radiation heat transfer has been thought as an independent module allows some flexibility, which is in part analyzed in a work that resulted from the development of the present thesis [2].

Contributions that can be considered original work include the procedure mentioned above and outlined in chapter 2, in order to calculate the view factors for cylindric geometries with axial symmetry; the use of interpolated distributions calculated from high resolution data in section 4.2.2, instead of the use of fitted distribution functions to a prescribed form; the estimation of the mesh size, according to the number of directions, in order to minimize the false scattering effect, as detailed in section B.2; the formulation of the boundary conditions suitable for solar applications, as explained in section 3.3.3; the definition of the time scales to characterize the flow in appendix C, and used also in chapter 6.

7.2 Future actions

Fortunately, there is always room to improve either a physical model, a numerical model, computer performance, etc... Next, I suggest some tasks, in no particular order, that could be performed within the framework of the CTTC, that could be considered a continuation of the research line followed up to date.

With the goal of aplying combined heat transfer to complex combustion problems, a formulation of a non gray radiation model capable of handle also non gray scattering particles will be of paramount importance to numerical analysis of sooty flames, where radiation scattering may be significant. Strategies consisting on spectrum grouping, such as these outlined in [3], are promising. Also, the implementation of more complex, full spectrum models such as the FSCK, section 4.2.5 is desired, since its handling of non-homogeneous media is better than that of the SLW (at least with the present formulation of this method). As a first approach, a similar strategy that is applied in the multi group FSCK [4] could be implemented.

The turbulence-radiation interaction (TRI) should be studied. The usual approach is to solve a time-averaged version of the RTE, modelling the correlated terms in different ways [5,6]. Simpler versions prior to any TRI model just solved the RTE using the average temperature field, and the optical properties evaluated at this temperature also [7]. Implementation of such methods will imply a step forward to simulation of turbulent flames.

The most important improvement to the work presented here is the formulation of the DOM for unstructured, three dimensional meshes. This will allow the resolution of complex geometries, thus permitting the code to solve real life problems. A good candidate to achieve this goal seems to be the finite volume method [8], although ray tracing methods are better suited for such geometries. Another method particularly good at complex geometries seems to be the radiation element method by ray emission model (REM^2) [9], and its recent improvement DOREM.

Another key aspect in which the presented work can be continued refers to parallelization. For combined conduction-convection problems, there exists a deep know how in the group about efficiently solve the Navier-Stokes equations using several computers. In the current stage of its development, the radiative radiative heat transfer solver, object of this thesis, cannot take advantage of the use of several computers to reduce the total computation time. Therefore, it is desirable to implement a version of the DOM suitable to be solved with parallelization techniques. In order to consider combined heat transfer, spatial domain decomposition should be employed, even if the nature of radiation suggests the other way around [10].

References

[1] G. Colomer, M. Costa, R. Cònsul, and A. Oliva. Three dimensional numerical simulation of convection and radiation in a differential heated cavity using the discrete ordinates method. *International Journal of Heat and Mass Transfer*, 47(2):257–269, 2004.

[2] G. Colomer, M. Costa, R. Cònsul, and J. Cadafalch. Simulación numérica de la convección en medios participantes en la radiación. In *Anales de Ingeniería*

Mecánica (Revista de la Asociación Española de Ingeniería Mecánica, Año 12), volume 3, pages 1691–1696, 2000.

[3] Michael F. Modest and Robert J. Riazzi. Assembly of full-spectrum k-distributions from a narrow-band database; effects of mixing gases, gases and nongray absorbing particles, and mixtures with nongray scatterers innongray enclosures. *J. Quant. Spectrosc. Radiat. Transfer*, 90(2):169–189, 2005.

[4] Hongmei Zhang and Michael F. Modest. Scalable multi-group full spectrum correlated k distributions for radiative transfer calculations. *Journal of Heat Transfer*, 125(3):454–461, 2003.

[5] P. J. Coelho. Detailed numerical simulation of radiative transfer in a nonluminous turbulent jet diffusion flame. *Combustion and Flame*, 136(4):481–492, 2004.

[6] D.R. Snelling, F. Liu, G.J. Smallwood, and O.L. Gülder. Determination of the soot absorption function and thermal accomodation coefficient using low-fluence LII in a laminar coflow ethylene diffusion flame. *Combustion and Flame*, 136:180–190, 2004.

[7] Claudio Mesyngier and Bakhtier Farouk. Turbulent natural convection - nongray gas radiation analysis in a square enclosure. *Numerical Heat Transfer, Part A*, 29:671–687, 1996.

[8] G. D. Raithby and E. H. Chui. A finite volume method for predicting radiant heat transfer in enclosures with participating media. *Journal of Heat Transfer*, 112:415–423, 1990.

[9] Shigenao Maruyama and T. Aihara. Radiation heat transfer of arbitrary three-dimensional absorbing, emitting and scattering media and specular and diffuse surfaces. *Journal of Heat Transfer*, 119(1):129–136, 1997.

[10] P. J. Coelho and J. Gonçalves. Parallelization of the finite volume method for radiation heat transfer. *Int. J. Num. Meth. Heat Fluid Flow*, 9(4):388–404, 1999.

Appendix A

Analytical solutions of the radiative transfer equation

It is always useful to have analytical solutions of a given equation for simple cases, in order to test the accuracy of numerical methods used to solve it. Several analytical solutions are presented in this appendix.

A.1 Formal solution

The radiative transfer equation, to be verified by the intensity radiation field, can be written, for a particular direction $\hat{\mathbf{s}}$, as

$$\frac{dI(\hat{\mathbf{s}})}{d\ell} = -(\kappa + \sigma_s)I(\hat{\mathbf{s}}) + \kappa I_b + \frac{\sigma_s}{4\pi}\int_{4\pi} \phi(\hat{\mathbf{s}}';\hat{\mathbf{s}})I(\hat{\mathbf{s}}')\,d\Omega' \equiv -\beta I(\hat{\mathbf{s}}) + \mathcal{S}(\hat{\mathbf{s}}). \tag{A.1}$$

We will drop hereinafter the dependence on $\hat{\mathbf{s}}$ of the intensity radiation field. The optical thickness is defined as the product of the extinction coefficient β by the geometrical length (for length-based extinction coefficient), that is, $d\ell = \beta\,d\tau$. The RTE equation reduces to the simpler form

$$\frac{dI}{d\tau} = -I + \frac{\mathcal{S}}{\beta}. \tag{A.2}$$

The general solution of equation A.2 is obtained assuming a solution of the form $I(\tau) = A(\tau)\exp(-\tau)$ suggested by the solution of the homogeneous version of equation A.2, where $A(\tau)$ is a function to be determined. Under such circumstances,

$$\frac{dI}{d\tau} = -I + \frac{dA}{d\tau}e^{-\tau} \quad \Rightarrow \quad \frac{dA}{d\tau} = e^{\tau}\frac{\mathcal{S}}{\beta}$$

By integrating the above equation, a closed form for $A(\tau)$ is obtained:

$$A(\tau) = \int_{\tau_0}^{\tau} \frac{\mathcal{S}(\tau)}{\beta} e^{-\tau'}\, d\tau' + C, \tag{A.3}$$

where C is an integration constant. This gives the final form of the general solution to equation A.2:

$$I(\tau) = A(\tau)e^{-\tau} = I(\tau_0)e^{-(\tau-\tau_0)} + \int_{\tau_0}^{\tau} \frac{\mathcal{S}(\tau')}{\beta} e^{-(\tau-\tau')}\, d\tau'. \tag{A.4}$$

The general solution, equation A.4, written in terms of the geometrical path ℓ, is

$$I_\eta(\ell) = I_\eta(\ell_0)e^{-\int_{\ell_0}^{\ell}\beta(s)\,ds} + \int_{\ell_0}^{\ell} \mathcal{S}(s)e^{-\int_s^{\ell}\beta(z)\,dz}\, ds. \tag{A.5}$$

A.2 Solution for a two dimensional cavity

In section 3.5.1, numerical results are compared to the analytical solution of a very simple case. It consists on a square enclosure containing a cold, gray medium. The radiative transfer equation is

$$\mu\frac{\partial I}{\partial x} + \nu\frac{\partial I}{\partial y} = -\kappa I, \tag{A.6}$$

where $\mu = \cos\theta$ and $\nu = \sin\theta$, being θ the angle between the direction for which equation A.6 is solved and the x axis. The following variables are defined:

$$\zeta = \frac{x}{\mu} + \frac{y}{\nu}, \tag{A.7}$$

$$\xi = \frac{x}{\mu} - \frac{y}{\nu}. \tag{A.8}$$

With these new variables, equation A.6 becomes

$$2\frac{\partial I}{\partial \zeta} = -\kappa I, \tag{A.9}$$

with an easy solution

$$I(\zeta,\xi) = C(\xi)\exp\left\{-\frac{\kappa}{2}\zeta\right\}. \tag{A.10}$$

The value of $C(\xi)$ will depend on the boundary conditions. Assuming that $0 \leq \theta \leq \pi/2$, the boundary conditons are $I(x=0,y) = I(x,y=0) = I_0$. The ξ-function C may be written as $C(\xi) = I_0 \exp\left\{-\frac{\kappa}{2} g(\xi)\right\}$, so equation A.10 will take the form

$$I(\zeta,\xi) = I_0 \exp\left\{-\frac{\kappa}{2}(\zeta + g(\xi))\right\}. \tag{A.11}$$

According the definition of ζ and ξ, $x = 0 \Rightarrow \zeta = -\xi$ and $y = 0 \Rightarrow \zeta = \xi$. So a function g such that $\zeta + g(\xi) = 0$ for $\xi = \pm\zeta$ must be choosen. This implies that $g(\zeta) = g(-\zeta) = -\zeta$. The simplest function g with this property is $g(\xi) = -|\xi|$, so the solution to equation A.6 is

$$I(\zeta,\xi) = I_0 \exp\left\{-\frac{\kappa}{2}(\zeta - |\xi|)\right\}. \tag{A.12}$$

In the original x, y coordinates, the solution can be written as

$$I(x,y) = I_0 \exp\left\{-\kappa \min\left(\frac{x}{\mu}, \frac{y}{\nu}\right)\right\}. \tag{A.13}$$

A.3 Radiative heat flux divergence

The integration of equation A.1 over the solid angle, taking into account all possible directions along which the RTE is solved, leads to the divergence of radiative heat flux,

$$\nabla \cdot \mathbf{q}_r(\mathbf{r}) = \kappa(\mathbf{r}) \left(4\pi I_b(\mathbf{r}) - \int_{4\pi} I(\mathbf{r},\hat{\mathbf{s}})\, d\Omega\right). \tag{A.14}$$

For an isothermal, purely absorbing, homogeneous, one dimensional layer of thickness L, surrounded by black, non emitting walls, it is possible to get an analytic form for the heat flux divergence. With the aid of the solutions presented before, the intensity radiation field is

$$I(x,\mu) = \left\{ \begin{array}{ll} I_b\left(1 - e^{-\kappa x/\mu}\right) & \text{for } 0 \leq \mu \leq 1 \\ I_b\left(1 - e^{\kappa(L-x)/\mu}\right) & \text{for } -1 \leq \mu \leq 0 \end{array} \right. \tag{A.15}$$

where x is the distance through the layer and $\mu = \cos\theta$, with θ being the angle between radiation propagation and the x axis. The integral over the solid angle translates into an integral over μ and a multiplication by 2π for an one dimensional problem. Hence, the divergence of heat flux is

$$\nabla \cdot \mathbf{q}_r(x) = 4\pi\kappa I_b - 2\pi\kappa \int_{-1}^{1} I(x,\mu)\, d\mu. \tag{A.16}$$

The integral can be arranged into

$$\int_{-1}^{1} I(x,\mu)\,d\mu = I_b\left(\int_0^1 (1-e^{-\kappa x/\mu})\,d\mu + \int_{-1}^{0}(1-e^{\kappa(L-x)/\mu'})\,d\mu'\right), \tag{A.17}$$

and, via the transformation $\mu = -\mu'$ on the last integral, the absorption term is calculated as

$$\int_{-1}^{1} I(x,\mu)\,d\mu = 2I_b - I_b\int_0^1 (e^{-\kappa x/\mu} + e^{-\kappa(L-x)/\mu})\,d\mu. \tag{A.18}$$

Finally, combining together the absorption and emission contributions, the divergence of radiative heat flux is obtained:

$$\boldsymbol{\nabla}\cdot\mathbf{q}_r(x) = 2\pi\kappa I_b\left\{E_2(\kappa x) + E_2(\kappa L - \kappa x)\right\}, \tag{A.19}$$

where $E_2(x)$ is the exponential integral function (see [1], p. 799).

References

[1] M.F. Modest. *Radiative heat transfer*. McGraw-Hill, 1993.

Appendix B

Basic mathematical details

B.1 Gauss-Legendre integration

This kind of numerical quadrature consists on approximate an integral using a weighted summation of the integrand evaluated at cleverly selected control points. To show that this is, in fact, possible, in this section we will find explicitly the weights and points in order to evaluate the integral of a function between -1 and 1 with such a weighted summation, where only four points are selected:

$$\int_{-1}^{1} f(x)\, dx = \omega_1 f_1 + \omega_2 f_2 + \omega_3 f_3 + \omega_4 f_4. \tag{B.1}$$

We will impose the restriction that the summation be exact for polynomials of degree less than 6. Thus a closed form for the weights will be obtained. Consider the polynomial

$$f(x) = \alpha P_0(x) + \beta P_1(x) + \gamma P_2(x) + \delta P_3(x) + \epsilon P_4(x) + \theta P_5(x) \tag{B.2}$$

where $P_i(x)$ is the Legendre polynomial of degree i. Recall that $P_0(x) = 1$, so the avobe integral equals 2α since Legendre polynomials are orthogonal in the interval $[-1, 1]$. Let's pick $\pm a_1$ and $\pm a_2$ so that $P_4(\pm a_1) = P_4(\pm a_2) = 0$. It is possible to show that

$$a_1 = \frac{1}{\sqrt{35}}\sqrt{15 + 2\sqrt{30}}; \qquad a_2 = \frac{1}{\sqrt{35}}\sqrt{15 - 2\sqrt{30}}; \tag{B.3}$$

Also, for brevity, $f_{1,2} = f(\pm a_1)$ and $f_{3,4} = f(\pm a_2)$. Now we compute

$$f_1 + f_2 + f_3 + f_4 = 4\alpha + 2\gamma \left(P_2(a_1) + P_2(a_2)\right), \tag{B.4}$$

since $P_{2n+1}(x)$ is an odd polynomial. This is the motivation to pick as evaluation points the roots of an even polynomial such as $P_4(x)$. Next, we compute

$$\omega_1 f_1 + \omega_2 f_2 + \omega_3 f_3 + \omega_4 f_4 = 2\alpha(\omega_1 + \omega_3) + 2\gamma\left(\omega_1 P_2(a_1) + \omega_3 P_2(a_2)\right). \tag{B.5}$$

Equations B.4 and B.5 can be written as

$$\begin{aligned} 2\alpha(\omega_1+\omega_3) + 4\gamma &= \omega_1(f_1+f_2) + \omega_3(f_3+f_4), & \text{(B.6)} \\ 4\alpha + 2\gamma\left(\frac{1}{\omega_1} + \frac{1}{\omega_3}\right) &= f_1 + f_2 + f_3 + f_4, & \text{(B.7)} \end{aligned}$$

provided we choose $\omega_1 = \omega_2 = 1/P_2(a_1)$ and $\omega_3 = \omega_4 = 1/P_2(a_2)$. We have now a system of equations, which has to be solved for α and γ. Defining $z_1 = \omega_1(f_1+f_2) + \omega_3(f_3+f_4)$ and $z_2 = \omega_1\omega_3(f_1+f_2+f_3+f_4)$, the system of equations takes the form

$$\begin{aligned} 2\alpha(\omega_1+\omega_3) + 4\gamma &= z_1, & \text{(B.8)} \\ 4\alpha\omega_1\omega_3 + 2\gamma(\omega_1+\omega_3) &= z_2. & \text{(B.9)} \end{aligned}$$

Solving for 2α we get

$$2\alpha = \int_{-1}^{1} f(x)\,dx = (f_1+f_2)\left\{\frac{\omega_1}{\omega_1-\omega_3}\right\} + (f_3+f_4)\left\{\frac{\omega_3}{\omega_3-\omega_1}\right\}. \tag{B.10}$$

So finally we can write

$$\int_{-1}^{1} f(x)\,dx = (f_1+f_2)\omega_1' + (f_3+f_4)\omega_2' \tag{B.11}$$

and give an explicit values of the weights:

$$\omega_1' = \frac{1}{2} - \frac{\sqrt{30}}{36} \quad \text{and} \quad \omega_2' = \frac{1}{2} + \frac{\sqrt{30}}{36}. \tag{B.12}$$

The function f is evaluated at the roots of $P_4(x)$ as stated above. The sum exactly equals the integral if the integrand is a polynomial of degree less than 6, and gives a good approximation in the other cases. For instance,

$$\int_{-1}^{1} e^x\,dx = e - \frac{1}{e} = 2.350402387\ldots \tag{B.13}$$

while

$$\omega_1'\left(e^{a_1} + e^{-a_1}\right) + \omega_2'\left(e^{a_2} + e^{-a_2}\right) = 2.350402092\ldots \tag{B.14}$$

B.2 Relation between false scattering and ray effect

It has been observed that, for a given number of discrete ordinates N, oscillations in the wall heat flux appear as the number of discretization nodes increases, as a clear manifestation of the so called ray effect. The reason of this behavior lies in the fact that the numerical (or false) scattering depends on the mesh size; the shorter the node spacing δ, the lower the false scattering effect. When the false scattering effect is lower, oscillations appear due to an insufficient number of discrete ordinates (ray effect). Thus, for any given N, an estimation of the node spacing δ is desired.

Assuming a rectangular cavity, with sides L_x and L_y, we focus our attention on the maximum distance Δ_y in the vertical wall for two consecutive ordinates θ_i and θ_{i-1}. With a little of geometry one find that

$$\Delta_y = L_x(\tan\theta_i - \tan\theta_{i-1}). \tag{B.15}$$

If the discrete ordinates are choosen as in [1], that is, $\theta_i = (2i-1)\pi/4N$, the distance in the vertical wall can be written as

$$\Delta_y = L_x \tan\frac{\pi}{2N}\left(1+\tan\frac{(2i-1)\pi}{4N}\tan\frac{(2i-3)\pi}{4N}\right). \tag{B.16}$$

Clearly Δ_y increases as the ordinate index i does, until i reaches the limiting value n such that $\theta_n < \psi$ and $\theta_{n+1} > \psi$, where $\psi = \arctan(L_y/L_x)$. After some algebra, and realizing that $(2n-1)\pi/4N = \psi - \epsilon$, with $\epsilon = \eta\pi/2N$ and $0 \leq \eta \leq 1$, the distance Δ_y is

$$\Delta_y = L_x \tan\frac{\pi}{2N}\left(1+\tan(\psi-\epsilon)\tan(\psi-\epsilon-\pi/2N)\right). \tag{B.17}$$

For small values of ϵ, the distance can be approximated by

$$\Delta_y \simeq L_x \tan\frac{\pi}{2N}\left(1+\left(\frac{L_y}{L_x}\right)^2 - \left(\frac{L_y}{L_x}\right)\left[\left(1+\left(\frac{L_y}{L_x}\right)^2\right)\left(\frac{\pi}{2N}(2\eta-1)\right)\right]\right) \tag{B.18}$$

The value of η is undetermined between 0 and 1. With the hypothesis that the mean value is $\eta = 1/2$, and considering that $N \gg 1$, finally we obtain

$$\Delta_y \simeq L_x\frac{\pi}{2N}\left(1+\left(\frac{L_y}{L_x}\right)^2\right). \tag{B.19}$$

The mean distance between nodes, δ_y, is choosen in a way that Δ_y is covered by m control volumes (with $m = 5$ for example), i.e., $\Delta_y = m\delta_y$, which implies that

$$\delta_y \simeq \frac{\pi L_x}{2Nm}\left(1+\left(\frac{L_y}{L_x}\right)^2\right) \tag{B.20}$$

It is worth noting that this δ_y is the minimum distance. For the distance between two nodes in the x axis the same analysis would yield the same results with x and y exchanged, that is,

$$\delta_x \simeq \frac{\pi L_y}{2Nm}\left(1+\left(\frac{L_x}{L_y}\right)^2\right). \tag{B.21}$$

B.3 The S_n ordinate set

The ordinate set of order n is obtained with the relation

$$\mu_i^2 = \mu_1^2 + \frac{2(i-1)}{n-2}(1-3\mu_1^2), \tag{B.22}$$

where the index i runs from 1 to $n/2$ (n is an even integer greater than 2). In the above relation μ_1 is determined, along with the weights a_i, by forcing that the approximated integral gives exact values for several moments, that is,

$$\sum_{i=1}^{n/2} a_i \mu_i^k = \frac{1}{k+1} \tag{B.23}$$

for some a priori selected values of k. Given the nature of the relations B.22 and B.23, a nonlinear system has to be solved.

B.3.1 Tables for several values of n

Here are the tabulated weights and directions for $n = \{4, 6, 8, 10, 12\}$.

i	μ_i	a_i
1	$2.9587585476808098 \times 10^{-1}$	$6.6666666666666667 \times 10^{-1}$
2	$9.0824829046386479 \times 10^{-1}$	$3.3333333333333333 \times 10^{-1}$

Table B.1: Ordinates and weights for the S_4 approximation. Equation B.23 holds for $k = \{0, 1, 2\}$.

The ordinate sets in tables B.1 to B.5 are suitable for multidimensional cases. In the three dimensional ordinate set, the directions are those that have projections μ_i on each axis and lie in the unit sphere. Thus each three-dimensional ordinate must obey the restriction $\mu_i^2 + \mu_j^2 + \mu_k^2 = 1$, with $1 \leq \{i, j, k\} \leq n/2$. Not all values of $\{i, j, k\}$ are useful. In fact, $i + j + k = n/2 + 2$ must hold for a valid direction. There are $n(n+2)/8$ such directions in each octant.

i	μ_i	a_i
1	$1.8386710903378073 \times 10^{-1}$	$4.3579844316562122 \times 10^{-1}$
2	$6.9505139601886445 \times 10^{-1}$	$4.6173644700210847 \times 10^{-1}$
3	$9.6560124918680024 \times 10^{-1}$	$1.0246510983227855 \times 10^{-1}$

Table B.2: Ordinates and weights for the S_6 approximation. Equation B.23 holds for $k = \{0, 1, 2, 3\}$.

i	μ_i	a_i
1	$1.4225553242346792 \times 10^{-1}$	$3.4436590771700393 \times 10^{-1}$
2	$5.7735026918962018 \times 10^{-1}$	$4.2028034773474127 \times 10^{-1}$
3	$8.0400872517751543 \times 10^{-1}$	$1.2634158137950924 \times 10^{-1}$
4	$9.7955435121784884 \times 10^{-1}$	$1.0901216316874843 \times 10^{-1}$

Table B.3: Ordinates and weights for the S_8 approximation. Equation B.23 holds for $k = \{0, 1, 2, 3, 4\}$.

i	μ_i	a_i
1	$1.3727193312794930 \times 10^{-1}$	$3.2024697371374683 \times 10^{-1}$
2	$5.0468891002891736 \times 10^{-1}$	$3.3536146934149275 \times 10^{-1}$
3	$7.0041288408170388 \times 10^{-1}$	$9.5325916625663462 \times 10^{-2}$
4	$8.5231773445654380 \times 10^{-1}$	$1.8894253053589230 \times 10^{-1}$
5	$9.8097544961666649 \times 10^{-1}$	$6.0123109783207715 \times 10^{-2}$

Table B.4: Ordinates and weights for the S_{10} approximation. Equation B.23 holds for $k = \{0, 1, 2, 5, 8, 10\}$.

i	μ_i	a_i
1	$1.2028966644554817 \times 10^{-1}$	$2.8269030105021986 \times 10^{-1}$
2	$4.5363844804142206 \times 10^{-1}$	$3.1219784576420512 \times 10^{-1}$
3	$6.3016353371905831 \times 10^{-1}$	$8.7042725966186285 \times 10^{-2}$
4	$7.6708820673840594 \times 10^{-1}$	$1.4291214605783314 \times 10^{-1}$
5	$8.8303032485016963 \times 10^{-1}$	$1.2413797501117962 \times 10^{-1}$
6	$9.8542416871763827 \times 10^{-1}$	$5.1019006150373108 \times 10^{-2}$

Table B.5: Ordinates and weights for the S_{12} approximation. Equation B.23 holds for $k = \{0, 1, 2, 5, 6, 8, 11\}$.

B.3.2 Three dimensional set for S_4

There are only three directions in the first octant. If we denote by $s_m = (i, j, k)$ the direction whose projections over x, y and z axis are μ_i, μ_j and μ_k then the three directions in this approximation are $s_1 = (1, 1, 2)$, $s_2 = (1, 2, 1)$ and $s_3 = (2, 1, 1)$. These directions form one group, as permutations of the projections over the axis are excluded. Therefore only one three-dimensional weight ω_m has to be found. Notice that when computing the first moment, for instance, in the x direction,

$$\sum_{i=1}^{N} \omega_m s_m^x, \tag{B.24}$$

under this approximation we get $\omega_1(2\mu_1 + \mu_2)$. Here N is the number of different groups, which is $n/2 - 1$. We want this projection to be $\pi/4$ since it will be computed over four octants (an hemisphere) when calculating the incoming or outgoing radiative heat flux. Recalling equation B.23 for $k = 1$, we can write

$$\frac{\pi}{4} = \omega_1(2\mu_1 + \mu_2) = \mu_1(2\omega_1) + \mu_2\omega_1 = \frac{\pi}{2} a_1\mu_1 + \frac{\pi}{2} a_2\mu_2, \tag{B.25}$$

so from the second term of the last two equations, $\omega_1 = (\pi/2)a_2$ and from table B.1 finally we get $\omega_1 = \pi/6$. If we had considered the first term instead, we would have get the same result. So the three dimensional set is defined by directions s_1, s_2 and s_3 with the common weight ω_1. By the symmetry of the three dimensional directions, the same results would have been obtained if the projection was over y or z axis.

B.3.3 Three dimensional set for S_6

The same technique applied on the previous section will be useful now. First, the three dimensional ordinates are $s_1 = (1, 1, 3)$, $s_2 = (1, 3, 1)$, $s_3 = (3, 1, 1)$, $s_4 = (2, 2, 1)$, $s_5 = (2, 1, 2)$ and $s_6 = (1, 2, 2)$. There are two groups in this case, s_1 to s_3, with weight ω_1, and s_4 to s_6, with weight ω_2. So calculating again the first moment projecting over x axis, and equating to $\pi/4$, we get

$$\frac{\pi}{4} = \omega_1(2\mu_1 + \mu_3) + \omega_2(2\mu_2 + \mu_1) = (2\omega_1 + \omega_2)\mu_1 + 2\omega_2\mu_2 + \omega_1\mu_3. \tag{B.26}$$

Recalling equation B.23 we can write

$$\frac{\pi}{4} = \frac{\pi}{2}a_1\mu_1 + \frac{\pi}{2}a_2\mu_2 + \frac{\pi}{2}a_3\mu_3. \tag{B.27}$$

By comparison of the two last terms of both equations, we obtain $\omega_1 = (\pi/2)a_3$ and $\omega_2 = (\pi/4)a_2$. The equality implied by the first term is verified by the values of ω_1 and ω_2. Looking at table B.2, the values are $\omega_1 = 0.1609518181$ and $\omega_2 = 0.3626469574$.

B.3.4 Three dimensional set for S_8

There will be three groups of equivalent directions, up to a permutation, and hence three weights ω_1, ω_2 and ω_3. With ω_1, the directions $s_1 = (1,1,4)$, $s_2 = (1,4,1)$ and $s_3 = (4,1,1)$. With ω_2, the direction $s_4 = (2,2,2)$, and with ω_3 the directions $s_5 = (1,2,3)$, $s_6 = (1,3,2)$, $s_7 = (2,1,3)$, $s_8 = (2,3,1)$, $s_9 = (3,1,2)$ and $s_{10} = (3,2,1)$. Considering again the first moment, we get

$$\frac{\pi}{4} = \omega_1(2\mu_1 + \mu_4) + \omega_2\mu_2 + \omega_3(2\mu_1 + 2\mu_2 + 2\mu_3). \tag{B.28}$$

Expanding the expression, reagrouping and comparing to equation B.23, we get

$$\begin{aligned}\frac{\pi}{2}a_1\mu_1 + \frac{\pi}{2}a_2\mu_2 + \frac{\pi}{2}a_3\mu_3 + \frac{\pi}{2}a_4\mu_4 &= \mu_1(2\omega_1 + 2\omega_3) + \mu_2(2\omega_3 + \omega_2)\\ &\quad + \mu_3(2\omega_3) + \mu_4\omega_1.\end{aligned} \tag{B.29}$$

Comparing again, and solving when necessary, we obtain $\omega_1 = (\pi/2)a_4$, $\omega_3 = (\pi/4)a_3$, $\omega_2 = (\pi/2)(a_2 - a_3)$, the last one arises comparing the factors multiplying μ_2. With the values taken from table B.3, $\omega_1 = 0.1712359055$, $\omega_2 = 0.4617179344$ and $\omega_3 = 0.0992284460$.

B.3.5 Three dimensional set for S_{10}

There will be four groups of directions, and hence four weights. With the weight ω_1, the directions $s_1 = (1,1,5)$, $s_2 = (1,5,1)$ and $s_3 = (5,1,1)$. With ω_2 the directions $s_4 = (2,2,3)$, $s_5 = (2,3,2)$ and $s_6 = (3,2,2)$. With ω_3 the directions $s_7 = (4,2,1)$, $s_8 = (4,1,2)$, $s_9 = (2,4,1)$, $s_{10} = (2,1,4)$, $s_{11} = (1,2,4)$ and $s_{12} = (1,4,2)$. Finally, with ω_4 the directions $s_{13} = (3,3,1)$, $s_{14} = (3,1,3)$ and $s_{15} = (1,3,3)$. Considering again the first moment, we get

$$\begin{aligned}\frac{\pi}{4} &= \omega_1(2\mu_1+\mu_5)+\omega_2(2\mu_2+\mu_3)+\omega_3(2\mu_1+2\mu_2+2\mu_4)\\ &\quad +\omega_4(2\mu_3+\mu_1) \quad \text{(B.30)}\\ &= \mu_1(2\omega_1+2\omega_3+\omega_4)+\mu_2(2\omega_2+2\omega_3)+\mu_3(\omega_2+2\omega_4)\\ &\quad +\mu_4(2\omega_3)+\mu_5\omega_1. \quad \text{(B.31)}\end{aligned}$$

Comparing to equation B.23 we find that the weights ω are $\omega_1 = (\pi/2)a_5$, $\omega_3 = (\pi/4)a_4$, $\omega_2 = (\pi/4)(a_2 - a_4)$, $\omega_4 = (\pi/8)(2a_3 + a_4 - a_2)$. According to table B.4 the numerical values for the weights are $\omega_1 = 0.0944411600$, $\omega_2 = 0.1149971656$, $\omega_3 = 0.1483951164$ and $\omega_4 = 0.0173702170$.

B.3.6 Three dimensional set for S_{12}

There will be five groups of directions, and hence five weights. With the weight ω_1, the directions $s_1 = (1,1,6)$, $s_2 = (1,6,1)$ and $s_3 = (6,1,1)$. With ω_2 the directions $s_4 = (2,2,4)$, $s_5 = (2,4,2)$ and $s_6 = (4,2,2)$. With ω_3 the directions $s_7 = (3,3,2)$, $s_8 = (3,2,3)$ and $s_9 = (2,3,3)$. With ω_4 the directions $s_{10} = (1,2,5)$, $s_{11} = (1,5,2)$, $s_{12} = (2,1,5)$, $s_{13} = (2,5,1)$, $s_{14} = (5,1,2)$ and $s_{15} = (5,2,1)$. Finally with ω_5, the directions $s_{16} = (1,3,4)$, $s_{17} = (1,4,3)$, $s_{18} = (3,1,4)$, $s_{19} = (3,4,1)$, $s_{20} = (4,1,3)$ and $s_{21} = (4,3,1)$. Considering again the first moment, we get

$$\begin{aligned}\frac{\pi}{4} &= \omega_1(2\mu_1+\mu_6)+\omega_2(2\mu_2+\mu_4)+\omega_3(2\mu_3+\mu_2)\\ &\quad +\omega_4(2\mu_1+2\mu_2+2\mu_5)+\omega_5(2\mu_1+2\mu_3+2\mu_4) \quad \text{(B.32)}\\ &= \mu_1(2\omega_1+2\omega_4+2\omega_5)+\mu_2(2\omega_2+\omega_3+2\omega_4)+\mu_3(2\omega_3+2\omega_5)\\ &\quad +\mu_4(\omega_2+2\omega_5)+\mu_5(2\omega_4)+\mu_6\omega_1. \quad \text{(B.33)}\end{aligned}$$

By comparison with equation B.23, the weights are found to be $\omega_1 = (\pi/2)a_6$, $\omega_4 = (\pi/4)a_5$, $\omega_2 = (\pi/2)(a_4 + a_5 + 2a_6 - a_1)$, $\omega_3 = (\pi/4)(a_3 + a_5 + 2a_6 - a_1)$ and $\omega_5 = (\pi/4)(a_1 - a_5 - 2a_6)$. According to table B.5 their numerical values are $\omega_1 = 0.0801404674$, $\omega_2 = 0.1357133976$, $\omega_3 = 0.0239769589$, $\omega_4 = 0.0974977375$ and $\omega_5 = 0.0443862383$.

References

[1] A. Sànchez and T.F. Smith. Surface radiation exchange for two-dimensional rectangular enclosures using the discrete ordinates method. *Journal of Heat Transfer*, 114:465–472, 1992.

Appendix C

Characterization of flows

C.1 Motivation

Solving problems such the differential heated cavity benchmark, convergence of solution problems may arise if, among other things, the discretization time step Δt is too small or too big. Even if we are only interested in the steady state, and the transient solution is used as a relaxation factor, an improper value of Δt will result on physically unrealistic solutions. According to results shown in [1], page 89, this difficulty on achieve convergence for large Δt is observed only for segregated solvers of the Navier-Stokes equations. Coupled solvers behaves better for such large values of Δt.

If Δt is choosen to be a small number, magnitudes such the temperature will slightly change from discrete time $n\Delta t$ to $(n+1)\Delta t$. The slight change is due to the fact that Δt is far less than the typical amount of time required by, say, heat diffusion. In other words, we don't let enough time for the temperature to change. On the other hand, if Δt is too big then physically unrealistic solutions are obtained because the numerical procedure can't follow the system evolution. Thus, solving the steady state by means of the transient solution as a relaxation factor will give wrong results since magnitudes at time $n\Delta t$ and $(n+1)\Delta t$ are nearly disconnected, providing useless solutions to the problem.

C.2 Time scales

The point now is to give a meaning to the words *small* and *big*. In problems such the differential heated cavity there are several simultaneous phenomena: natural buoyancy, which tends to put the hotter fluid above the cold one, heat conduction, which tends to equalize the fluid temperature over all the domain, radiation transfer, which tends to equalize the temperature over a significant part of the domain… Each phenomena occur at a different time rates, and we may think that these rates are independent one of each other. The time rates are referred as conduction time scale (τ_c), buoyancy time scale (τ_b), radiation time scale (τ_r) and viscous time scale (τ_v), as in section 6.2.4. Taking acount of the physical properties of the fluid, it is possible to combine them to form combinations with dimensions of time:

$$\begin{aligned}
\tau_c &\propto \frac{L^2 \rho c_p}{k}, && \text{(C.1)}\\
\tau_b &\propto \sqrt{\frac{L}{g\beta\Delta T}}, && \text{(C.2)}\\
\tau_r &\propto \frac{\rho c_p L \Delta T}{\sigma_B T^4}, && \text{(C.3)}\\
\tau_v &\propto \frac{\rho L^2}{\mu}. && \text{(C.4)}
\end{aligned}$$

These are merely indicative quantities, but information about what is going on can be obtained. Here L is a characteristic length of the problem, and ΔT is the maximum difference of temperatures within the fluid. When numerically solving a problem, we must choose the time step Δt of the same order of magnitude of the minimum of $\{\tau_c, \tau_b, \tau_r, \tau_v\}$ to get the results with the least number of iterations.

C.3 Dimensionless equations

Taking into account the above discussion, it is clear that at least three kinds of dimensionless variables can be chosen, one for each time scale. If we denote by τ_α any of the above mentioned time scales, the dimensionless form of Navier-Stokes equations can be written as (all variables are dimensionless)

$$\begin{aligned}
\boldsymbol{\nabla}\cdot\mathbf{u} &= 0, && \text{(C.5)}\\
(\partial_t + \mathbf{u}\cdot\boldsymbol{\nabla})\,\mathbf{u} &= -\boldsymbol{\nabla}P + \gamma_1\nabla^2\mathbf{u} + \gamma_2 T\hat{\mathbf{n}}, && \text{(C.6)}\\
(\partial_t + \mathbf{u}\cdot\boldsymbol{\nabla})\,T &= \gamma_3\nabla^2 T - \gamma_4\boldsymbol{\nabla}\cdot\mathbf{Q}^R, && \text{(C.7)}
\end{aligned}$$

where

$$\gamma_1 = \frac{\tau_\alpha\mu}{\rho L^2} = \frac{\tau_\alpha}{\tau_v}; \quad \gamma_2 = \frac{\tau_\alpha^2 g\beta\Delta T}{L} = \left(\frac{\tau_\alpha}{\tau_b}\right)^2; \quad \gamma_3 = \frac{\tau_\alpha k}{\rho c_p L^2} = \frac{\tau_\alpha}{\tau_c}, \qquad \text{(C.8)}$$

and the dimensionless pressure P is $P_d(\tau_\alpha^2/\rho L^2)$. The vector $\hat{\mathbf{n}}$ is unitaty in the direction of the gravity field, and γ_4 depends upon the factor used to define the dimen-

	γ_1	γ_2	γ_3	γ_4
$\tau_\alpha = \tau_v$	1	Ra/Pr	$1/Pr$	$\phi/Pr\,Pl$
$\tau_\alpha = \tau_b$	$\sqrt{Pr/Ra}$	1	$1/\sqrt{Ra\,Pr}$	$\phi/Pl\,\sqrt{Ra\,Pr}$
$\tau_\alpha = \tau_c$	Pr	$Ra\,Pr$	1	ϕ/Pl
$\tau_\alpha = \tau_r$	$Pr\,Pl/\phi$	$Ra\,Pr\,Pl^2/\phi$	Pl/ϕ	1

Table C.1: Values of the dimensionless parameters of NSE

sionless radiative heat transfer:

$$\mathbf{Q}^R = \mathbf{q}^R \frac{\tau_\alpha}{\rho c_p L \Delta T} \quad \Rightarrow \quad \gamma_4 = 1, \tag{C.9}$$

$$\mathbf{Q}^R = \mathbf{q}^R \frac{1}{\sigma_B T_0^4} \quad \Rightarrow \quad \gamma_4 = \frac{\tau_\alpha \sigma_B T_0^4}{\rho c_p L \Delta T} = \frac{\tau_\alpha}{\tau_r}. \tag{C.10}$$

The latter assumption is used used in this appendix. It is possible to identify $\gamma_1, \gamma_2, \gamma_3$ and γ_4 with the viscous, buoyancy, conduction and radiation time scales previously defined.

The complete description of the problem will need four values, the Rayleigh number Ra, the Prandtl number Pr, the Planck number Pl and the dimensionless reference temperature ratio ϕ. The dimensionless temperature reference ratio arises because radiation heat exchange depends not only on temperature differences but also on an absolute temperature. The values of such parameters are

$$Ra = \frac{\tau_c \tau_v}{\tau_b^2}, \qquad Pr = \frac{\tau_c}{\tau_v}, \qquad Pl = \phi \frac{\tau_r}{\tau_c}, \qquad \phi = \frac{T_0}{\Delta T}, \tag{C.11}$$

with ΔT being the maximum temperature difference in the domain. By equating τ_α to the time scales previously defined, the values for γ_i in equations C.6 and C.7 are obtained and reported on table C.1.

C.4 Illustrative results

The differential heated cavity problem is solved for the same initial and boundary conditions, for several values of Δt, with radiation not taken into account. The situation consists on a fluid contained on a square cavity of length $1m$. The east and west walls are maintained at T_e and T_w respectively, and the north and south walls are adiabatic. The direction of the gravitational field is of course perpendicular to north and south walls. The appropriate dimensionless values are $Pr = 0.71$ and the

Δt	# iter.	time(s)	# iter.	time(s)
$\frac{1}{8}\tau_b$	3579	118.6	2000	67.0
$\frac{1}{2}\tau_b$	985	32.9	547	18.4
τ_b	513	17.3	288	9.5
$2\tau_b$	265	8.6	155	5.2
$3\tau_b$	180	6.2	111	3.8
$8\tau_b$	∞	∞	53	1.8
$12\tau_b$	∞	∞	510	17.7
$16\tau_b$	∞	∞	∞	∞
	$Ra = 10^6$		$Ra = 10^5$	

Table C.2: Number of iterations and computation time. The symbol ∞ means that for the corresponding Δt no solution was obtained.

time scales are $\tau_c = 7.1s$, $\tau_v = 10s$, and $\tau_b = 0.266s$ for $Ra = 10^5$ and $\tau_b = 0.084s$ for $Ra = 10^6$.

The number of iterations and computation times are presented in table C.2. In both cases, choosing the time step Δt as $\frac{1}{2}\tau_b$ roughly doubles the number iterations and the computation time. The best choice isn't τ_b, but a few times its value (depending on the value of Ra).

One may safely choose $\Delta t = 2\tau_b$ (assuming that $\tau_b < \tau_c$) as the first approach, and then increase slightly the time step. In this particular case, a relation between τ_b and n_{iter} (the number of iterations) can be found:

$$\begin{aligned} n_{\text{iter}} &\propto \tau_b^{-0.94} \qquad (Ra = 10^6), \\ n_{\text{iter}} &\propto \tau_b^{-0.87} \qquad (Ra = 10^5). \end{aligned}$$

For some values of Ra (for example $Ra \leq 10^4$), the time step parameter may be increased without limit, obtaining always convergence and the same result in the same time independant of Δt.

C.5 Physical meaning of time scales

C.5.1 Conduction time scale

The definition of τ_c may seem arbitrary. In this section a very simple analytical case is studied in order to see the time evolution of one magnitude. Consider an one-dimensional medium of length L, and a constant thermal conductivity k, a specific heat c_P and density ρ. At time $t = 0$ the medium has uniform temperature T_0.

Assuming that the medium is bounded by another media which is at $T = 0$, the energy conservation equation reads

$$\rho c_P \frac{\partial T}{\partial t} = k \frac{\partial^2 T}{\partial x^2}. \tag{C.12}$$

Since at $x = 0$ and $x = L$ the temperature must be 0, a Fourier decomposition of the temperature $T(x,t)$ is attempted:

$$T(x,t) = \sum_{n=1}^{\infty} a_n(t) \sin\left(\frac{\pi n x}{L}\right), \tag{C.13}$$

with $a_{2n}(0) = 0$ and $\pi a_{2n+1}(0) = 4T_0/(2n+1)$. Also the diffusion coefficient D is defined as $D = k/(\rho c_P)$. Thus equation C.12 can be written as

$$\sum_{n=1}^{\infty} \dot{a}_n(t) \sin\left(\frac{\pi n x}{L}\right) = -D \sum_{n=1}^{\infty} \lambda_n a_n(t) \sin\left(\frac{\pi n x}{L}\right), \tag{C.14}$$

where

$$\lambda_n = \frac{n^2 \pi^2}{L^2}. \tag{C.15}$$

Since the sine functions forms a basis of functions, we must have $\dot{a}_n(t) = -D\lambda_n a_n(t)$ and, therefore, $a_n(t) = a_n(0)e^{-t/\tau}$, with $\tau = 1/(D\lambda_n)$. The last term to vanish is of course a_1, and it takes approximately 5τ units of time (since $e^{-5} < 10^{-2}$):

$$5\tau = \frac{5}{D\lambda_1} = \frac{5}{\pi^2}\frac{L^2 \rho c_P}{k} \simeq \frac{\tau_c}{2}, \tag{C.16}$$

so the system needs about $\tau_c/2$ units of time to reach the steady state. Hence the conduction time scale may be regarded as the amount of time that needs a system to reach the steady state when only conduction heat transfer is considered.

C.5.2 Buoyancy time scale

The buoyancy scale is related to the time it takes an isothermal bubble, hotter than the surrounding fluid in an ammount ΔT, to travel a distance L. The bubble will be lighter than the surrounding fluid, for positive thermal coefficient β, and therefore will move upwards (oposed to graviational field). Under the Boussinesq approximation, commonly employed in natural convection, we have

$$\rho_{\text{fluid}} \simeq \rho_{\text{bub}} + \left.\frac{\partial \rho}{\partial T}\right|_{\text{bub}} \delta T = \rho_{\text{bub}}(1 - \beta \delta T), \tag{C.17}$$

with $\delta T = T_{\text{fluid}} - T_{\text{bub}}$.

The buoyant force over the bubble is, recalling the Archimedes principle, $\rho_{\text{fluid}} V g$, while its weight is $\rho_{\text{bub}} V g$, where V is the volume of the bubble. The resulting acceleration is the difference of the two opposite forces divided by the mass:

$$a_{\text{bub}} = -g\beta\delta T. \tag{C.18}$$

The simplest possible situation is an isothermal bubble moving within an isothermal fluid. If we consider $T_{\text{bub}} = T_{\text{fluid}} + \Delta T$, we get $\delta T = -\Delta T$, and a resulting upward acceleration $a_{\text{bub}} = g\beta\Delta T$. The acceleration is constant, and therefore the time it takes a bubble to travel a distance L is simply

$$t = \sqrt{\frac{2L}{a_{\text{bub}}}} = \sqrt{2}\sqrt{\frac{L}{g\beta\Delta T}} \equiv \sqrt{2}\tau_b. \tag{C.19}$$

If a linear temperature profile of the fluid is assumed, the factor $\sqrt{2}$ becomes $\pi/2$. As in the previous time scale, we neglect all numerical factors, obtaining equation C.2.

C.5.3 Radiation time scale

Considering that radiation is the only mode of energy transfer, it can be readily estimated the time it takes for a hot gas layer to reach the temperature of its surroundings, by radiating its excess energy. The ammount of energy that has to be released is roughly $\rho c_p V \Delta T$, and it is emitted at a rate $\sigma_B T^4 S$, being T a mean temperature of the gas layer. Therefore, we have

$$\tau_r = \frac{\rho c_p V \Delta T}{\sigma_B T^4 S} \equiv \frac{\rho c_p L \Delta T}{\sigma_B T^4}, \tag{C.20}$$

where L is the volume/surface ratio V/S.

C.5.4 Viscous time scale

The viscous time scale can be considered analogous to conduction time scale, since for very viscous fluids, equation C.6 becomes a diffusion equation on the velocity, similar to equation C.12, with a diffusion coefficient of μ/ρ, resulting in equation C.4. This time can be understood as the time it takes for a velocity gradient to be established at a distance L of the boundaries, due to non-slip boundary condition.

References

[1] M. Soria. *Parallel multigrid algorithms for computational fluid dynamics and heat transfer*. PhD thesis, Universitat Politècnica de Catalunya, 2000.

Nomenclature

Latin symbols

$A_{i,j}$	area of surfaces i, j
a_k	non gray model weighting coefficient
B^i	attenuation term of the RTE
E_b	angular integrated blackbody intensity
$F_{i\rightarrow j}$	view factor from surface i to surface j
$F(T, \bar{\xi}, k)$	black body distribution function
f	interpolation factor
$f(\eta, \eta_i)$	absorption line profile
G	incident energy, $\int_{4\pi} I \, d\Omega$
g_k	irradiosity of surface k
I	intensity radiation field
I_b	directional blackbody intensity
j_k	radiosity of surface k
k^*	mean absorption coefficient
ℓ	parametric length along direction $\hat{\mathbf{s}}$
N	number of ordinates per quadrant or octant, number of absorption coefficient intervals in non gray methods
$\hat{\mathbf{n}}$	vector perpendicular to a given area
Q_k	total radiative heat flux trough area k
Q^*	dimensionless total heat flux
Q^*_c	dimensionless covection heat flux
Q^*_r	dimensionless radiative heat flux
$q(\hat{\mathbf{n}})$	radiative heat flux through a surface whose normal is $\hat{\mathbf{n}}$
$\hat{\mathbf{q}}_r$	radiative heat flux vector
$\mathcal{S}$	heat source
S^i	source term of the RTE
S_n	ordinate set used to integrate the RTE
$\hat{\mathbf{s}}$	direction vector
$\hat{\mathbf{s}}^*$	direction vector $\hat{\mathbf{s}}$ reflected with respect to a given plane
T_n	alternative ordinate set to integrate the RTE

Greek symbols

α	absorptivity of a surface
$\alpha(T, 0 \rightarrow \ell)$	total absorptivity of a gas layer
β	extinction coefficient, thermal expansion coefficient

γ	anisotropic phase function coefficient
ϵ	emissivity of a surface
ε	emissivity of a gas layer
η	wavenumber, $1/\lambda$
θ	polar angle of $\hat{\mathbf{s}}$
κ	absorption coefficient
κ_P	Planck mean absorption coefficient
λ	wavelength of a photon
μ	cosine of the polar angle, $\cos\theta$
μ^*	sine of the polar angle, $\sin\theta$
ν	cosine of the azimuthal angle, $\cos\varphi$
ν^*	sine of the azimuthal angle, $\sin\varphi$
$\bar{\xi}$	set of variables on which the absorption coefficient may depend on
ρ	total reflectivity of a surface, $\rho_s + \rho_d$
ρ_d	diffuse reflectivity of a surface
ρ_s	specular reflectivity of a surface
σ_B	Stefan-Boltzmann constant, $5.6697 \times 10^{-8} W/m^2 K^4$
σ_s	scattering coefficient
τ	optical depth, transmissivity of a surface
Ω	solid angle
ω	albedo, $\sigma_s/(\sigma_s + \kappa)$

Concept index